Title
Osteocyte regulation of bone quality in homeostasis and in skeletal disease

Author
Mazur, Courtney

Publication Date
2019

Osteocyte regulation of bone quality in homeostasis and in skeletal disease

by
Courtney Mazur

DISSERTATION
Submitted in partial satisfaction of the requirements for degree of
DOCTOR OF PHILOSOPHY

in

Bioengineering

in the

GRADUATE DIVISION

of the

UNIVERSITY OF CALIFORNIA, SAN FRANCISCO
AND
UNIVERSITY OF CALIFORNIA, BERKELEY

Approved:

DocuSigned by:
Tamara Alliston — Tamara Alliston
E233CABEF261499...
Chair

DocuSigned by:
EC Hsiao — Edward Hsiao
[illegible]D4BA...
DocuSigned by:
Grace O'Connell — Grace O'Connell
[illegible]4FF...
DocuSigned by:
Jeffrey Lotz — Jeffrey Lotz
3D96864A89B54C2...

Committee Members

Acknowledgements

Thank you to my amazing support network of mentors, coworkers, friends and family. Progress in research is rarely made in isolation, and your intellectual and personal guidance truly made this work possible.

Thank you to my family for cheering me on from afar. My parents have always supported my scientific aspirations and all that I want to accomplish in life. Kirsten even manages to rally random strangers she meets to wish me luck in my research. Your unwavering support has bolstered me through life and especially through graduate school.

Thank you to James for always giving me the encouragement, advice, or chocolately dessert that I need to get things done. While you still may not understand exactly what I do in lab, your support has been instrumental to my happiness and success.

I'm so thankful for the community that I've found in California. Friends from my Bioengineering cohort, PPSG, and outside of UCSF have helped me grow in science and as a person over this time. I've enjoyed hiking, biking, skiing, exploring the Bay Area, eating, problem solving, and learning with you. Karen, Jon, Dave, Allison, Roberto, Nick, Rami, Dan, Mary, Maddie, Alex, Tina, Dinara, and Rachel, you've taught me so much. Dave, it has been a pleasure to have you as a friend in and out of lab. Our scientific discussions, commiseration, and exchanging of corny jokes were central to my grad school experience and are completely irreplaceable.

Thank you to my mentor, Tamara Alliston, who has been an amazing role model in science and in life. You have taught me so much about planning, conducting, and communicating science and about the type of scientist and mentor that I want to be. I am so

grateful for the opportunities you pushed me towards and for all the constructive feedback along the way. Without you I may never have known about osteocytes at all, and together we have learned so much. Thank you also to my thesis committee, Ed Hsiao, Grace O'Connell, and Jeff Lotz, and to the Ortho Lab PIs Rich Schneider, Aaron Fields and Andrew Brack, for thoughtful discussions about my work and career.

I am indebted to Ortho Lab members past and present who established a welcoming, helpful, and fun work culture. Throwing trivia nights and solving crossword puzzles together made the lab experience even better. Thank you to Neha, Tristan, Gaby, Serra, Cristal, Claire, Joanna and Spenser who went before me in this PhD process and were generous mentors, collaborators and friends. Dave, Karsyn, Charlie, Jihee, Luke, Stephanie, Minali, JJ, Jenny, Justin, Sean, Carter, and Thao, you all made this a great place to come to work each day. The quality of my fellow Alliston Lab members over the years has been truly excellent. I am so looking forward to seeing what you do next.

Abstract

Osteocyte regulation of bone quality in homeostasis and in skeletal disease

by

Courtney Mazur

Osteocytes are the most numerous cells in bone, working from within the mineralized matrix to exert control over their local environment and cells on the bone surface. Healthy osteocytes are key to bone homeostasis, but the full functional importance of their local remodeling activity, called perilacunar/canalicular remodeling (PLR), is only recently being discovered. This work uses multiple mouse models to investigate the molecular mechanisms controlling osteocyte PLR and demonstrates that repression of PLR causes severe loss of bone material quality. Additionally, osteocyte dysfunction is shown to disrupt bone homeostasis during skeletal disease and to promote degradation of overlying cartilage in the joint. Finally, we begin to determine the extent to which PLR is mechanosensitive, revealing distinct site- and magnitude-specific modulation of osteocyte behavior with applied load. Together these findings reveal new essential roles for osteocytes and PLR within bone and joints during homeostasis and disease.

Table of Contents

List of Figures

List of Tables

Chapter 1

Introduction

To provide its critical functions supporting locomotion and protecting internal organs, bone must be strong enough to resist fractures during normal activity. Bone mass, typically measured with 2D areal projections in the clinic, has largely been the focus of fracture prevention treatment. To this end, anti-resorptive drugs like bisphosphonates and anabolic therapies like intermittent PTH injections are used by several million Americans per year (1). While these therapies are successful at increasing bone mass, having higher bone mass does not necessarily reduce fractures, with one 8000-person study finding that half of its patients with fractures were not clinically osteoporotic (2). Therefore there is a critical need to understand and target other contributions to bone strength.

Bone quality encompasses characteristics of bone that contribute to its strength independent of quantity. Metrics of bone quality include bone geometry, the organization and composition of the extracellular matrix, flexural properties before and after deformation, and material properties like elastic modulus and toughness (3–8). In materials science and engineering, a long history of research connects metallurgic and manufacturing techniques to the quality and subsequent fracture resistance of metals and ceramics. In biology, however, the molecular and cellular control of bone quality is not well understood, a situation exacerbated by the lack of non-invasive clinical bone quality diagnostics (9).

Much of what is known about bone quality stems from analyses of animal bones performed ex vivo. In particular, the foundational work of John Currey has described the uniquely adapted material properties that accompany mineralized tissues with different functions. Adult polar bear bones, for example, have a higher elastic modulus than juvenile bones, which helps the longer adult bones to withstand deformation under much higher body weight (10). Deer antlers have relatively low mineralization but high toughness, decreasing the likelihood of fracture in an impact with an opponent (11). Even within a single animal, tissue-specific calibration of material properties correlates with specialized functions like weight-bearing and hearing (4). Given the remarkable specificity of material properties achieved in nature, cellular mechanisms to maintain them must exist.

In bone, there are three main types of cells. Bone-forming osteoblasts and bone-resorbing osteoclasts reside on bone surfaces, and osteocytes are located within the mineralized matrix in cavities called lacunae. Osteocytes derive from the osteoblast lineage, undergoing a series of transcriptional and morphological changes as they become surrounded by bone matrix (12). Mature osteocytes are characterized by expression of E11, Dmp1, and sclerostin, and have an extensive network of dendrites which connect to other osteocytes, vasculature, and surface cells through channels in bone called canaliculi. Originally thought to be quiescent cells, a rapidly-growing body of research over the past century has revealed osteocytes as active, essential participants in bone homeostasis.

Despite differentiating from the osteoblast lineage, osteocytes have the ability to resorb surrounding bone and enlarge their lacunae, a process initially called osteocytic osteolysis (13). In humans with rickets and osteomalacia (14), and in hibernating squirrels and bats (15, 16), enlarged osteocyte lacunae were associated with metabolic stress or pathological conditions. It was later studies in rats, egg-laying hens, and lactating mice that demonstrated that osteocytes could also deposit bone, making the maintenance of the matrix surrounding their lacunae a reversible process (17–19). Improvements in techniques and technologies available for studying these bone-embedded cells has shown that the canaliculi are also subject to remodeling (20, 21), giving rise to the current term for osteocytic maintenance of their surroundings: perilacunar/canalicular remodeling, or PLR.

Increases or decreases in perilacunar/canalicular remodeling (PLR) activity can be characterized by analyzing molecular, cellular, and tissue-level hallmarks (22). Genes involved in matrix degradation and acidification, such as matrix metalloproteinase 13 (Mmp13), Cathepsin K (Ctsk), carbonic anhydrase 1 and 2, tartrate resistant acid phosphatase 5 (Acp5), and ATPase subunits, are strongly induced with the increase in lacunar size that occurs during lactation, and they return to baseline expression levels as lacunar size returns to normal (19, 23). The involvement of these molecules in PLR is supported by studies showing that their systemic ablation causes abnormal organization of bone extracellular matrix, another hallmark of PLR. Specifically, changes to the size and organization of the lacunocanalicular network and disruption of normal collagen linearity are associated with systemic repression of PLR genes (24–28). At the tissue level, systemic repression of PLR genes can both increase and decrease bone mineralization (24, 27). Therefore, osteocytes use protease secretion and acidification to maintain the collagen and mineral in the bone extracellular matrix.

As of 2014, osteocytes were recognized as important participants in bone's response to metabolic stress and in bone homeostasis, but many important gaps in knowledge remained. First, since previous studies investigating PLR had used systemic stimuli or gene ablation, the extent to which PLR is regulated specifically by osteocytes was unknown. Similarly, factors that act in an osteocyte-intrinsic manner to control PLR in vivo had not yet been identified. Second, while repression of PLR hallmarks was often accompanied by bone fragility, the ability of osteocytes and PLR to causally control bone quality had not been determined. Third, effects on or by osteocytes and PLR during musculoskeletal disease were largely unexplored, as were the interactions of osteocytes with nearby tissues like muscle, articular cartilage, nerves, and vasculature. And fourth, while osteocytes are mechanosensitive and able to coordinate the response of osteoblasts and osteoclasts to load, it was not known whether PLR itself is regulated by load. Answers to these questions would provide critical advances towards the identification of cellular and molecular targets for the treatment of bone quality as a contributor to bone strength.

This work used novel mouse models and rigorous material testing techniques to identify osteocyte PLR as a novel mechanism regulating bone material quality under control of cell-intrinsic TGFβ signaling and MMP13. With human surgical and cadaveric tissues and mouse models of joint injury, we showed that osteocyte PLR is repressed in multiple musculoskeletal diseases and that repression of PLR through MMP13 can promote osteoarthritis. Finally, I addressed the hypothesis that osteocyte PLR is mechanosensitive and identified a possible role for the sympathetic nervous system in osteocyte TGFβ signaling. Together this work highlights osteocytes as critical regulators of bone and joint health in homeostasis and disease.

References

1. Jha S, Wang Z, Laucis N, Bhattacharyya T (2015) Trends in Media Reports, Oral Bisphosphonate Prescriptions, and Hip Fractures 1996-2012: An Ecological Analysis. *J Bone Miner Res* 30(12):2179–2187.
2. Wainwright SA, et al. (2005) Hip fracture in women without osteoporosis. *J Clin Endocrinol Metab* 90(5):2787–2793.
3. Acevedo C, et al. (2018) Contributions of Material Properties and Structure to Increased Bone Fragility for a Given Bone Mass in the UCD-T2DM Rat Model of Type 2 Diabetes. *J Bone Miner Res* 33(6):1066–1075.
4. Chang JL, et al. (2010) Tissue-specific calibration of extracellular matrix material properties by transforming growth factor-beta and Runx2 in bone is required for hearing. *EMBO Rep* 11(10):765–771.
5. Zioupos P, Currey J. (1998) Changes in the Stiffness, Strength, and Toughness of Human Cortical Bone With Age. *Bone* 22(1):57–66.
6. Boskey AL, et al. (2016) Examining the Relationships Between Bone Tissue Composition, Compositional Heterogeneity, and Fragility Fracture: A Matched Case-Controlled FTIRI Study. *J Bone Miner Res* 31(5):1070–1081.
7. Heveran CM, et al. (2019) Chronic kidney disease and aging differentially diminish bone material and microarchitecture in C57Bl/6 mice. *Bone* 127:91–103.
8. Lane NE, et al. (2006) Glucocorticoid-treated mice have localized changes in trabecular bone material properties and osteocyte lacunar size that are not observed in placebo-treated or estrogen-deficient mice. *J Bone Miner Res* 21(3):466–476.
9. Hunt HB, Donnelly E (2018) Bone Quality Assessment Techniques: Geometric,

Compositional, and Mechanical Characterization from Macroscale to Nanoscale. *Clin Rev Bone Miner Metab* 14. doi:10.1007/s12018-016-9222-4.

10. Currey JD (1999) *The design of mineralised hard tissues*.
11. Currey JD (1979) Mechanical properties of bone tissues with greatly differing functions. *J Biomech* 12(4):313–319.
12. Bonewald LF (2011) The amazing osteocyte. *J Bone Miner Res* 26(2):229–38.
13. Bélanger LF (1969) Osteocytic osteolysis. *Calcif Tissue Res* 4(1):1–12.
14. von Recklinghausen F (1910) Untersuchungen uber Rachitis und Osteomalacia. *Jena Gustav Fischer*.
15. Haller AC, Zimny ML (1977) Effects of Hibernation on Interradicular Alveolar Bone. *J Dent Res* 56(12):1552–1557.
16. Kwiecinski GG, Krook L, Wimsatt WA (1987) Annual skeletal changes in the little brown bat, Myotis lucifugus lucifugus, with particular reference to pregnancy and lactation. *Am J Anat* 178(4):410–420.
17. Baylink DJ, Wergedal JE (1971) Bone formation by osteocytes. *Am J Physiol* 221(3):669–678.
18. Zambonin Zallone A, Teti A, Primavera M V, Pace G (1983) Mature osteocytes behaviour in a repletion period: the occurrence of osteoplastic activity. *Basic Appl Histochem* 27(3):191–204.
19. Qing H, et al. (2012) Demonstration of osteocytic perilacunar/canalicular remodeling in mice during lactation. *J Bone Miner Res* 27(5):1018–1029.
20. Dole NS, et al. (2017) Osteocyte intrinsic TGFβ signaling regulates bone quality through perilacunar/canalicular remodeling. *Cell Rep* 21(9):2585–2596.

21. Tiede-Lewis LAM, et al. (2017) Degeneration of the osteocyte network in the C57BL/6 mouse model of aging. *Aging (Albany NY)* 9(10):2187–2205.
22. Yee CS, Schurman CA, White CR, Alliston T (2019) Investigating Osteocytic Perilacunar/Canalicular Remodeling. *Curr Osteoporos Rep* 17(4):157–168.
23. Jähn K, et al. (2017) Osteocytes Acidify Their Microenvironment in Response to PTHrP In Vitro and in Lactating Mice In Vivo. *J Bone Miner Res* 32(8):1761–1772.
24. Tang SY, Herber R-P, Ho SP, Alliston T (2012) Matrix Metalloproteinase-13 is Required for Osteocytic Perilacunar Remodeling and Maintains Bone Fracture Resistance. *J Bone Miner Res* 27(9):1936–1950.
25. Holmbeck K, et al. (2005) The metalloproteinase MT1-MMP is required for normal development and maintenance of osteocyte processes in bone. *J Cell Sci* 118(Pt 1):147–156.
26. Nyman JS, et al. (2011) Differential effects between the loss of MMP-2 and MMP-9 on structural and tissue-level properties of bone. *J Bone Miner Res* 26(6):1252–1260.
27. Inoue K, et al. (2006) A crucial role for matrix metalloproteinase 2 in osteocytic canalicular formation and bone metabolism. *J Biol Chem* 281(44):33814–33824.
28. Li CY, et al. (2006) Mice Lacking Cathepsin K Maintain Bone Remodeling but Develop Bone Fragility Despite High Bone Mass. *J Bone Miner Res* 21(6):865–875.

Chapter 2

Methods

Many methods were in development over the course of my dissertation work, so protocols for similar experiments sometimes vary across chapters. Common methods are detailed here, with further details provided within each chapter as applicable.

Mice

Mice were bred and housed in a specific pathogen-free environment at UCSF. Animals were housed in groups with temperature maintained between 68-74 °F, humidity maintained between 30-70%, 12-hour light/dark cycles, and access to water and rodent chow *ad libitum*. To control for the sexually dimorphic effects of bone material properties (1), osteoarthritis (2), and PLR itself (3), only male mice were used for these studies. The procedures for animal experiments were approved by the Institutional Animal Care and Use Committee at the University of California, San Francisco.

Mouse lines bred for these studies are described in Table 2.1. Homozygous MMP13$^{fl/fl}$ mice and homozygous TβRII$^{fl/fl}$ mice were bred with hemizygous DMP1-Cre$^{+\backslash-}$ mice to generate litters with wildtype (Cre$^{-/-}$) and knockout (Cre$^{+/-}$) mice compared in Chapters 3 and 5. All experiments were initiated when mice reached 8 weeks of age.

At the end of experiments, mice were euthanized by CO_2 inhalation followed by cervical dislocation. Tissues designated for RNA or protein analysis were collected first and quickly processed through to liquid nitrogen. Tissues designated for histology, microCT, and mechanical testing were then collected as needed.

Animals were monitored during multi-day experiments and humanely euthanized before the experimental endpoint as needed to relieve distress, for example, due to weight loss, severe fight wounds, or other morbidity.

Table 2.1: Mouse lines bred at UCSF

Name	Background	Jackson Labs #	Chapters	Reference
DMP1-Cre$^{+\backslash-}$	C57BL/6	023047	3, 5	(4)
TβRII$^{fl/fl}$	C57BL/6J	012603	3	(5)
MMP13$^{fl/fl}$	FVB	005710	5	(6)
SBE	C57BL/6 x SJL	005999	6, 8	(7)

Tissue processing for histology

Mouse tibias, femurs, mandibles, or intact knee joints were fixed in 10% neutral buffered formalin for 48 hours and decalcified for two weeks in 0.5 M di- and tetra-sodium EDTA, changed three times per week. Tissues were dehydrated in graded ethanol and infiltrated with paraffin. Knees were embedded in paraffin blocks at 90 degrees of flexion and sectioned in the frontal plane. Hemimandibles were embedded and sectioned sagittally. Femurs and tibias were embedded and sectioned axially to generate 6-7 μm sections. All brightfield imaging was conducted on a Nikon Eclipse E800 microscope, and all fluorescence imaging was conducted on a Leica DMi8 confocal microscope.

Analysis of collagen fiber orientation by picrosirius red stain

Polarized light microscopy was performed on deparaffinized sections stained in a saturated aqueous solution of picric acid with 0.1% Direct Red-80 for one hour, as described (8, 9) to visualize collagen fiber orientation. During microscopy, polarized filters were rotated to achieve the maximum birefringence before capturing each image. Red channel images were processed using the OrientationJ plugin for ImageJ to generate histograms of collagen fiber orientation for comparison (10).

Analysis of the lacunocanalicular network by Ploton silver stain

To visualize the osteocyte lacunocanalicular network, sections were deparaffinized and incubated in two-parts 50% silver nitrate and one-part 1% formic acid in 2% gelatin solution for 55 minutes, as described (8, 11). Stained slides were then washed in 5% sodium thiosulfate for 10 minutes and subsequently dehydrated, cleared, and mounted. Brightfield images were acquired at 100x for analysis, and comparable regions of interest were compared (i.e. medial, lateral, anterior or posterior for axial sections, and medial or lateral for frontal sections). Analysis methods are detailed within each chapter.

Immunohistochemistry (IHC)

IHC was used to examine protein localization qualitatively and semi-quantitatively (i.e. % positively stained cells). For IHC, slides were deparaffinized and hydrated prior to incubation in Innovex Uni-Trieve low temperature retrieval solution (NB325) in a 65 °C water bath for 30 minutes. Endogenous peroxidase activity was quenched using 3% H_2O_2 for 10 minutes at room temperature. For the subsequent steps, Innovex Universal Animal

Immunohistochemistry Kit (329ANK) was utilized. Samples were blocked with Fc-Block and Background Buster for 45 minutes each at room temperature. Primary antibodies were diluted in PBS (Table 2.2) and incubated in a humid chamber at 4°C overnight. Secondary linking antibody and HRP-enzyme were both used at room temperature for 10 minutes each. Fresh DAB solution was applied and incubated at room temperature for 5 minutes prior to washing with tap water and mounting with Innovex Advantage aqueous mounting medium. Negative controls were performed by substituting rabbit IgG at the same concentration as primary antibody.

Immunofluorescence (IF)

IF was used to examine protein localization qualitatively and semi-quantitatively (i.e. % positively stained cells). Sections were deparaffinized and antigens were retrieved with 0.25% trypsin-EDTA at 37 °C for 25 minutes, or with Uni-Trieve solution as above. Sections were blocked with Background Buster (Innovex) for 10 minutes or 10% normal goat serum for one hour, incubated with PBS/0.1% Tween for 5 minutes, and then incubated overnight with primary antibodies diluted in PBS with 0.1% Tween and 5% BSA (Table 2.2). After washes in PBS, secondary antibody conjugated to Alexa Fluor 594 (Table 2.2) was applied for 60 minutes. Background was reduced with copper sulfate for 10 minutes, and slides were mounted with Prolong Gold antifade reagent with DAPI.

Table 2.2: Antibodies used for immunostaining and Western blotting

Target	**Product number**	**Concentration**	**Chapter**
MMP13	Abcam 39012	1:50 – 1:100	4, 5, 8
Cathepsin K	Abcam 19027	1:50	5
Aggrecan	Abcam 216965	1:200	5
Collagen II	Abcam 34712	1:200	5
CGGFVDIPEN	Gift from Dr. John Mort	1:200	5
CGGNITEGE	Gift from Dr. John Mort	1:200	5
Goat anti-rabbit	Invitrogen A-11012	1:1000	5
Sclerostin	R&D AF1589	1:100 – 1:200	8
Donkey anti-goat	Invitrogen A-11058	1:1000	8
Beta-actin	Abcam 8226	1:2000	6, 7, 8
pSmad3	Gift from Dr. Ed Leof	1:1000	6
pSmad3	Abcam 52903	1:2000	7
pCreb	Cell signaling #9198	1:1000	7
pAkt	Cell signaling #4060	1:1000	7, 8
p-p38	Cell signaling #9211	1:1000	7

Micro-computed tomography (μCT)

For skeletal phenotyping, tibias, femurs, or intact knee joints were dissected and stored in 70% ethanol. Cortical analysis was conducted in a 1-mm region equidistant from the proximal and distal ends of the bone. Femoral trabecular analysis was conducted in a 2-mm region immediately proximal to the distal growth plate. Samples were scanned using a Scanco μCT50 specimen scanner with an X-ray potential of 55 kVp, current of 109 μA, and voxel size of 10 μm. Thresholding and quantification was performed as previously described (12, 13).

Cells

Osteocyte cell lines were cultured on plates coated with rat tail collagen type I in 20% O_2 and 5% CO_2. MLO-Y4 osteocyte-like cells were cultured in α-MEM with nucleosides with 2.5% FBS, 2.5% FCS and 1% P/S at 37 °C (14). OCY454 cells were cultured in α-MEM with nucleosides with 10% FBS and 1% antibiotic/antimycotic at 34 °C until confluent (Day 0), then differentiated at 37 °C for 14 days before use (15).

Quantitative RT-PCR analysis

Humeri or tibias designated for mRNA analysis were quickly cleaned of muscle and periosteum, epiphyses were trimmed, and marrow was removed by centrifugation (16). If applicable, tibias were then cut into proximal and distal portions. All bones were snap-frozen in liquid nitrogen. Two humeri per animal were combined into one tube with 1.5 mL TRIzol, and tibia portions were each placed into a tube with 1 mL QIAzol. Tubes were stored on ice and each bone sample homogenized with a rotor-stator homogenizer (GLH, Omni). Lysate was then stored at -80 °C until RNA extraction.

For RNA extraction, QIAzol or TRIzol lysate was thawed, and 200 μL chloroform per mL of lysate was added and mixed well. The mixture was centrifuged for 15 minutes at 12,000 g at 4 °C, and the aqueous supernatant was carefully transferred to a clean tube. mRNA collected in TRIzol was purified using the RNeasy Mini Kit, and mRNA and miRNA collected in QIAzol was purified using the miRNeasy Mini Kit (Qiagen), following manufacturer's instructions for each kit. On-column DNase (Qiagen) was applied for 15 minutes, and the RNA was eluted in 35 μL RNase-free water. RNA concentration was quantified with a NanoDrop spectrophotometer and the product stored at -80 °C until use.

To make cDNA, 1 μg or 15 μL RNA per sample was reverse-transcribed using the iScript cDNA synthesis kit, and the concentration was brought to 10 ng/μL with clean water. cDNA was stored at -20 °C until use.

qPCR was performed with both Taqman and SYBR-based technologies. Primer product numbers and sequences are given in Table 2.3. 10-80 ng equivalent of cDNA was used per reaction, with input quantity chosen for each gene in order to achieve threshold values of amplification between 20 and 30 cycles. All reactions were performed in technical duplicates. Expression was then quantified by the ΔΔCt method (17).

Table 2.3: SYBR primer sequences and TaqMan Assay IDs used for gene expression analysis of murine cDNA

Target	**Sequence**	**ng input**	**Chapter**
L19 (sense)	5'-ACGGCTTGCTGCCTTCGCAT -3'	20	4, 6
L19 (antisense)	5'-AGGAACCTTCTCTCGTCTTCCGGG-3'		
β-actin (sense)	5'-CTCTGGCTCCTAGCACCATGAAGA-3'	10-20	5, 6, 7
β-actin (antisense)	5'-GTAAAACGCAGCTCAGTAACAGTCCG-3'		
β-actin	Mm02619580_g1	10-20	5, 8
18s (sense)	5'-CGAACGTCTGCCCTATCAAC-3'	1-10	6, 7
18s (antisense)	5'-GGCCTCGAAAGAGTCCTGTA-3'		
18s	Mm03928990_g1	1-10	7
Gilz (sense)	5'-TGACTGCAACGCCAAAGC-3'	20-50	4
Gilz (antisense)	5'-CTGATACATTTCGGTGTTCATGGTT-3'		
Mmp13 (sense)	5'-CGGGAATCCTGAAGAAGTCTACA-3'	20-50	4, 5, 6
Mmp13 (antisense)	5'-CTAAGCCAAAGAAAGATTGCATTTC-3'		
Mmp14 (sense)	5'-AGGAGACGGAGGTGATCATCATTG-3'	20-50	4, 5
Mmp14 (antisense)	5'-GTCCCATGGCGTCTGAAGA-3'		
Mmp2 (sense)	5'-AACGGTCGGGAATACAGCAG-3'	20-50	4, 5
Mmp2 (antisense)	5'-GTAAACAAGGCTTCATGGGG-3'		
Ctsk (sense)	5'- GAGGGCCAACTCAAGAAGAA-3'	20-50	4, 5
Ctsk (antisense)	5'- GCCGTGGCGTTATACATACA-3'		
Acp5 (sense)	5'-CGTCTCTGCACAGATTGCAT-3'	20-50	4, 5
Acp5 (antisense)	5'-AAGCGCAAACGGTAGTAAGG-3'		
Car2 (sense)	5'-GAGCTTCACTTGGTTCACTGG-3'	20-50	4, 5
Car2 (antisense)	5'-TGTGAGGCAGGTCCAATCTTC-3'		
Mmp13	Mm00439491_m1	20-50	5
Rankl (sense)	5'-CCAAGATCTCTAACATGACG-3'	20-50	5
Rankl (antisense)	5'-CACCATCAGCTGAAGATAGT-3'		
Opg (sense)	5'-AGAGCAAACCTTCCAGCTGC-3'	20-50	5
Opg (antisense)	5'-CTGCTCTGTGGTGAGGTTCG-3'		
Timp1 (sense)	5'-CTCAAGACCTATAGTGCTGGC-3'	20-50	5, 6
Timp1 (antisense)	5'-CAAAGTGACGGCTCTGGTAG-3'		
Timp2 (sense)	5'-AGTGCAAGATCACTCGCTGT-3'	20-50	5
Timp2 (antisense)	5'-CGCGCAAGAACCATCACTTC-3'		
Atp6v0d2 (sense)	5'-TCTTGAGTTTGAGGCCGACAG-3'	20-50	5
Atp6v0d2 (antisense)	5'-GCAACCCCTCTGGATAGAGC-3'		
Atp6v1g1 (sense)	5'-TGAGCAGTTGACTTAGGCCG-3'	20-50	5
Atp6v1g1 (antisense)	5'-CCTCCGGTTCTTTCGCTTGC-3'		

Target	Sequence	ng input	Chapter
Sost (sense)	5’-TCCTCCTGAGAACAACCAGAC-3’	40-80	6, 7
Sost (antisense)	5’-TGTCAGGAAGCGGGTGTAGTG-3’		
AP (sense)	5’-TAGTACTGGCCATCGGCACC-3’	20-50	6
AP (antisense)	5’-AGGTCTCTTGGGCTTGCTGT-3’		
OC (sense)	5’-GCTGCGCTCTGTCTCTCTGA-3’	20-50	6
OC (antisense)	5’-GCCCTCCTGCTTGGACATGA-3’		
OP (sense)	5’-TCTGGCAGCTCAGAGGAGAA-3’	20-50	6
OP (antisense)	5’-CTGAGATGGGTCAGGCACCA-3’		
Col1a1 (sense)	5’-GACGCATGGCCAAGAAGACA-3’	20-50	6
Col1a1 (antisense)	5’-ACCTCGGGTTTCCACGTCTC-3’		
Ptgs2 (sense)	5’-CTCACGAAGGAACTCAGCAC-3’	>75	6, 7
Ptgs2 (antisense)	5’-GGATTGGAACAGCAAGGATTTG-3’		
Serpine1 (sense)	5’-CAGATGACCACAGCGGGGAA-3’	20-50	6, 7
Serpine1 (antisense)	5’-GGCATGAGCTGTGCCCTTCT-3’		
Sost	Mm00470479_m1	40-80	7
Phex	Mm00448119_m1	50	7
Dmp1	Mm01208363_m1	50	7
Adra2a (sense)	5’-CGCAGGCCATCGAGTACAA-3’	20-50	7
Adra2a (antisense)	5’-GATGACCCACACGGTGACAA-3’		
Adra2b (sense)	5’-TCCCTCTGGGAGGCAAGTG-3’	20-50	7
Adra2b (antisense)	5’-GGCCAGGATTCCAGACCATT-3’		
Adra2c (sense)	5’-CATGGGCGTGTTCGTACTGT-3’	20-50	7
Adra2c (antisense)	5’-CAGGCCTCACGGCAGATG-3’		
Adrb2 (sense)	5’-GCCACGACATCACTCAGGAAC-3’	20-50	7
Adrb2 (antisense)	5’-CGATAACCGCACTGAGGATGG-3’		
c-fos (sense)	5’-AAGGGGCAAAGTAGAGCAGC-3’	50	7
c-fos (antisense)	5’-TTGATCTGTCTCCGCTTGGA-3’		
Serpine1	Mm00435858_m1	20-50	8
Ptgs2	Mm00478374_m1	>75	8
Gja1	Mm01179639_s1	40	8

Flexural strength tests

Bones designated for mechanical testing were gently cleaned of muscle to avoid scratching the bone surface, then stored in HBSS at 4 °C for up to two weeks, or wrapped in HBSS-soaked gauze and stored at -20 °C. All bones were brought to room temperature before testing. Whole hydrated femurs were loaded to failure in 3-point bending using a Bose Electroforce 3200 test frame. Tests were performed in air at a fixed displacement rate of 10 μm/s, and load-displacement data was recorded. Data processing is described within each Chapter.

In vivo axial tibial loading

After troubleshooting and optimization (Chapter 6), the final murine in vivo axial tibial loading protocol applies 5-7 N compressive load to the right leg, or approximately 800-1200 microstrain. Before loading, mice are anesthetized with injectable ketamine/xylazine anesthesia (100 mg/kg ketamine and 10 mg/kg xylazine) and lack of response to a toe pinch is confirmed before the right leg is placed into the load frame. A BOSE Electroforce ELF3200 desktop load frame is fitted with custom fixtures to cup the mouse heel and knee and provide axial compressive load to the tibia (Figure 6.1). The actuator is manually displaced until the load feedback reads the desired maximum load and then a preload of -0.5 N. The actuator is then set to cycle between these two positions for 600 cycles at 1 Hz in displacement control mode, with load data recorded on a 50 lb load cell. One 10-minunte loading session was performed per day for up to five consecutive days. After each loading session, mice are returned to a warm cage to recover and then ambulate normally until the next loading session or predetermined harvest time. After harvest, the non-loaded left tibia serves as an internal control for each animal.

Protein extraction from bone

Tibias designated for protein analysis were quickly cleaned of muscle and periosteum, epiphyses were trimmed, and marrow was removed by centrifugation. If applicable, tibias were then cut into proximal and distal portions. Foil-wrapped bones were stored in liquid nitrogen until protein extraction. RIPA buffer (10 mM Tris pH 8, 1 mM EDTA, 1 mM EGTA, 140 mM NaCl, 1% Triton X, 0.1 % sodium deoxycholate, 0.1% SDS) supplemented with protease and phosphatase inhibitors (5 mM sodium orthovanadate, 10 mM sodium pyrophosphate, 100 mM NaF, 500 μM PMSF, 1x cOmplete Mini tablet) was prepared fresh on the day of protein harvest (18, 19).

In the final, optimized protocol, 2-mL tubes containing 2.8-mm ceramic beads are pre-chilled at -20 °C. Whole tibias or proximal and distal portions are placed in individual tubes with 90 μL ice cold RIPA. Without allowing bones to thaw, tubes are then placed in a Bead Mill 24 Homogenizer (Omni) and shaken at 5 m/s for four bouts of 10 seconds with rest on ice half-way through. After bone lysate is in RIPA, samples are incubated on ice for 30 minutes, sonicated 8x15 seconds with a cup-horn sonicator in a circulating ice water bath, and centrifuged for 6 minutes at 12,000 g at 4 °C. Liquid protein lysate is then transferred to a clean tube for storage at -20 °C for one week or -80 °C.

Protein quantification

To normalize protein loading into Western blots, protein lysate from loaded and non-loaded tibias was quantified using the Bradford assay. Technical duplicates of 1 μL of each protein sample are loaded into UV-transparent 96-well plates (Corning #3635). A standard curve of BSA from 1.26 μg/μL to 10.08 μg/μL plus 1 μL RIPA per well is also plated in technical duplicates. Protein assay dye concentrate (BioRad #500-0006) is diluted in water, and 200 μL are mixed into each well. A single read at 595 nm is then performed on a spectrophotometer and sample protein concentrations interpolated from the standard curve.

Western blotting

8.5% or 10% polyacrylamide gels with 5% stacking gels were prepared in the lab and stored at 4 °C for up to one week. Protein lysate was thawed on ice and preparations of equal protein content with Laemmli buffer were made for each sample. Protein preparations were heated in a 95 °C bath for 10 minutes, then cooled on ice and briefly spun to collect condensation. Equal volumes of prepared protein were loaded in each lane along with ladder and TGFβ-treated cell lysate as a positive control. 60-70 V was applied until the protein passed through the stacking gel, then 100-150 V was applied until the 37 kDa band of the ladder was near the bottom of the gel. The protein was transferred to a nitrocellulose membrane at 100 V for 50-70 minutes, blocked with 5% milk in TBS for 50-90 minutes, and washed in TBST before application of primary antibodies (Table 2.2). Primary antibodies were applied for 1 hour at room temperature or overnight at 4 °C with gentle shaking. Secondary antibodies with IR tags were applied for 1 hour at room temperature. β-actin antibody was prepared in 1% milk, and phospho-protein antibodies were prepared in 5% BSA. Protein was detected on an Odyssey Infrared Imager (Licor) and images quantified in ImageStudio Lite software. Signal from test protein bands was normalized to signal from corresponding β-actin control bands for each sample and then compared across conditions.

References

1. Somerville JM, Aspden RM, Armour KE, Armour KJ, Reid DM (2004) Growth of C57BL/6 mice and the material and mechanical properties of cortical bone from the tibia. *Calcif Tissue Int* 74(5):469–475.
2. Ma H-L, et al. (2007) Osteoarthritis severity is sex dependent in a surgical mouse model. *Osteoarthr Cartil* 15(6):695–700.
3. Dole N, Yee C, Mazur C, Acevedo C, T A TGF-beta regulation of perilacunar/canalicular remodeling is sexually dimorphic. *BioRxiv* 737395.
4. Lu Y, et al. (2007) DMP1-targeted Cre expression in odontoblasts and osteocytes. *J Dent Res* 86(4):320–325.
5. Leveen P, et al. (2002) Induced disruption of the transforming growth factor beta type II receptor gene in mice causes a lethal inflammatory disorder that is transplantable. *Blood* 100(2):560–568.
6. Stickens D, et al. (2004) Altered endochondral bone development in matrix metalloproteinase 13-deficient mice. *Development* 131(23):5883–95.
7. Lin AH, et al. (2005) Global analysis of Smad2/3-dependent TGF-beta signaling in living mice reveals prominent tissue-specific responses to injury. *J Immunol* 175(1):547–554.
8. Jauregui EJ, et al. (2016) Parallel mechanisms suppress cochlear bone remodeling to protect hearing. *Bone* 89:7–15.
9. Montes GS, Junqueira LC (1991) The use of the Picrosirius-polarization method for the study of the biopathology of collagen. *Mem Inst Oswaldo Cruz* 86(3):1–11.
10. Rezakhaniha R, et al. (2012) Experimental investigation of collagen waviness and

orientation in the arterial adventitia using confocal laser scanning microscopy. *Biomech Model Mechanobiol* 11(3–4):461–73.

11. Ploton D, et al. (1986) Improvement in the staining and in the visualization of the argyrophilic proteins of the nucleolar organizer region at the optical level. *Histochem J* 18(1):5–14.
12. Dole NS, et al. (2017) Osteocyte intrinsic TGFβ signaling regulates bone quality through perilacunar/canalicular remodeling. *Cell Rep* 21(9):2585–2596.
13. Fowler TW, et al. (2017) Glucocorticoid suppression of osteocyte perilacunar remodeling is associated with subchondral bone degeneration in osteonecrosis. *Sci Rep* 7:44618.
14. Kato Y, Windle JJ, Koop BA, Mundy GR, Bonewald LF (1997) Establishment of an osteocyte-like cell line, MLO-Y4. *J Bone Miner Res* 12(12):2014–2023.
15. Spatz JM, et al. (2015) The Wnt Inhibitor Sclerostin Is Up-regulated by Mechanical Unloading in Osteocytes in Vitro. *J Biol Chem* 290(27):16744–16758.
16. Kelly NH, Schimenti JC, Patrick Ross F, van der Meulen MCH (2014) A method for isolating high quality RNA from mouse cortical and cancellous bone. *Bone* 68:1–5.
17. Livak KJ, Schmittgen TD (2001) Analysis of Relative Gene Expression Data Using Real-Time Quantitative PCR and the 2−ΔΔCT Method. *Methods* 25(4):402–408.
18. Alford AI, et al. (2012) Two molecular weight species of thrombospondin-2 are present in bone and differentially modulated in fractured and nonfractured tibiae in a murine model of bone healing. *Calcif Tissue Int* 90(5):420–428.
19. Nguyen J, et al. (2013) Load Regulates Bone Formation and Sclerostin Expression through a TGF b -Dependent Mechanism. *PLoS One* 8(1):e53813.

Chapter 3

TGFβ regulates fracture toughness via osteocytes

This chapter is based on work published in the peer-reviewed article titled “Osteocyte intrinsic TGFβ signaling regulates bone quality through perilacunar/canalicular remodeling“ by Neha S. Dole, Courtney M. Mazur, Claire Acevedo, Justin P. Lopez, David A. Monteiro, Tristan W. Fowler, Bernd Gludovatz, Flynn Walsh, Jenna N. Regan, Sara Messina, Daniel S. Evans, Thomas F. Lang, Bin Zhang, Robert O. Ritchie, Khalid S. Mohammad, and Tamara Alliston in *Cell Reports*.

Introduction

Differences in bone mass do not fully explain bone fragility, leaving bone quality as an important and underutilized therapeutic target for reducing fracture. Bone quality includes mass-independent properties across multiple length scales, such as bone geometry, organization and composition of the extracellular matrix, flexural properties before and after deformation, and material properties like elastic modulus and toughness (1–4). The properties of mineralized tissues vary widely in nature, allowing for function-driven adaptations like the stiff whale bulla and flexible, tough antlers (5). Despite the remarkable specialization of bone quality parameters, the biological mechanisms controlling them are incompletely understood.

Transforming growth factor beta (TGFβ) is an essential regulator of both bone mass and bone quality. Previous work from the Alliston Lab and others has implicated osteoblasts and osteoclasts as TGFβ-responsive regulators of bone mass and density (4, 6–8). These systemic or osteoblast-targeted interventions for TGFβ signaling have also caused differences in bone flexural strength, mineralization, and toughness (6, 7, 9, 10). However, the cellular mechanisms by which TGFβ regulates bone quality remain unknown.

Osteocytes are a prime candidate to be the cellular target of TGFβ in its control of bone quality. In addition to their coordination of osteoblast and osteoclast function, osteocytes play a direct role in the maintenance of the surrounding ECM through perilacunar-canalicular remodeling (PLR) (11). While PLR has previously been described primarily as a stress-response mechanism for liberating minerals in times of high metabolic demand (12), recent work has highlighted this process as essential for homeostatic bone ECM organization and material properties (11). Further, systemic ablation of proteases that act downstream of TGFβ, including MMP2, MMP13, MMP14, and Cathepsin K, has caused suppression of PLR hallmarks (11, 13–16). It was not yet known whether this process was regulated in an osteocyte-intrinsic manner.

Using mice with a DMP1-Cre-mediated ablation of the TGFβ receptor type II (TβRII), Dole et al. tested the hypothesis that TGFβ controls PLR in an osteocyte-intrinsic manner (17). Male mice with an osteocyte-specific loss of function in TGFβ signaling had lower expression of key PLR genes Mmp2, Mmp13, Mmp14, Cathepsin K and Acp5. While collagen linearity was not affected, the ability of osteocytes to maintain their lacunocanalicular network was visibly reduced, with disorganized canaliculi that were 50% shorter than in WT bones. These findings are consistent with osteocyte-intrinsic control of PLR and now allow for testing of the hypothesis that osteocyte PLR is the cellular mechanism by which TGFβ regulates bone quality.

Methods

Mice

DMP1-Cre (9.6-kb promoter) and TβRII$^{fl/fl}$ mice were bred at UCSF to generate wildtype (DMP1-Cre^{-}; TβRII$^{fl/fl}$) and TβRII$^{ocy-/-}$ (DMP1-Cre^{+}; TβRII$^{fl/fl}$) mice with osteocyte-targeted inhibition of TGFβ signaling (Table 2.1). At two months old, femurs were dissected from male mice of each genotype and gently cleaned of soft tissue before storage in Hank's Balanced Salt Solution (HBSS) at 4 °C. Tests were conducted within one month of bone harvest.

Flexural testing

HBSS-soaked femurs were brought to room temperature and positioned on a 6 mm span with the central loading point at the mid-diaphysis. Tests were conducted with the anterior side in compression, and load-displacement data was recorded. After fracture, bone cross-sections were imaged in a variable pressure scanning electron microscope (VP-SEM, Hitachi S-4300SE/N) for measurement of diameter and cortical thickness, and moment of inertia was calculated modeled as an elliptical cross-section (18). Load-displacement measurements were converted to stress-strain using standard beam theory equations. Bending modulus was calculated from the linear portion of the stress-strain curve and yield stress was calculated using the 0.2% offset method (19) with custom Python scripts for n=5 per group.

In situ fracture toughness testing

One femur per animal was notched at the mid-diaphysis on the posterior side to a depth of approximately one third the anterior-posterior diameter using an oscillating razor blade irrigated with 0.05 μm diamond suspension. Bones were briefly sonicated to remove diamond residue, then returned to storage in HBSS at 4 °C. Three-point bending was performed with the notched posterior side in tension on a 6mm span with a Gatan Microtest 2-kN stage (Gatan, Abingdon, UK) mounted in the VP-SEM at 35 Pa. Loading was performed at a displacement rate of 50 μm/min while samples were observed in real time in the SEM in back-scattered electron mode at an excitation voltage of 20 kV. Images were captured and peak load recorded each time a crack advanced. This protocol was performed on n≥6 femurs from individual animals, but bones were excluded from analysis if scratches from dissection were apparent in SEM images or if the notch was found to be too shallow or deep. Work of fracture was calculated for n=5 bones per group, and crack resistance curves (R-curves) were generated for n=3 bones per group.

Nanoindentation

Femurs from WT and TβRII$^{ocy-/-}$ mice were embedded in EpoxiCure 2 resin. Sections were generated at the mid-diaphysis using a low-speed circular saw, polished with increasing grits of sandpaper, and finished with 1 μm diamond polish, then stored in HBSS at 4 °C. Samples were blotted dry immediately before mounting in a nanoindenter with a Berkovitch tip. Indents were made every 5 μm between the endosteal and periosteal surface using a trapezoidal loading profile with 1000 μN peak load and a 10-second hold. The load-displacement curves were used to calculate local elastic modulus by the Olivier-Pharr method for n=3 per group (6, 20).

Results

DMP1-Cre^{+};TβRII$^{fl/fl}$ mice (TβRII$^{ocy-/-}$) have an osteocyte-specific loss of function in TGFβ signaling, which was validated using immunohistochemistry. Additionally, changes in gene expression and lacunocanalicular network organization are consistent with repression of PLR (17). While trabecular bone mass is elevated in TβRII$^{ocy-/-}$ femurs, cortical thickness was unchanged. Therefore, any evidence of cortical bone fragility would be attributable to defects in bone quality.

Flexural testing was initially performed on three genotypes: wild-type mice (WT), mice expressing DMP1-Cre with one floxed TβRII allele (TβRII$^{ocy +/-}$), and mice expressing DMP1-Cre with two floxed TβRII alleles (TβRII$^{ocy-/-}$). Average stress-strain curves from flexural tests for n=5 bones per group demonstrate an allelic dosage effect of TβRII deletion (Figure 3.1 A), but only WT and TβRII$^{ocy-/-}$ specimens were analyzed further. TβRII$^{ocy-/-}$ bone showed a 26% reduction in bending modulus and 27% reduction in yield stress compared to WT bone, indicating reduced resistance to elastic deformation (Figure 3.1 B-C). The Young's modulus of cortical bone tissue as measured by nanoindentation was also significantly lower in TβRII$^{ocy-/-}$ bone (Figure 3.1 D).

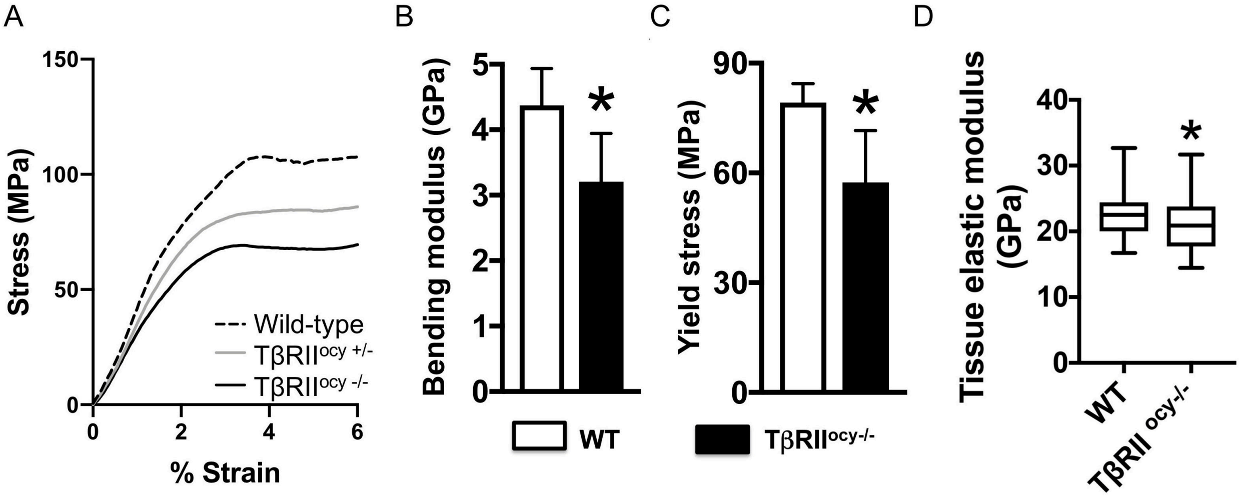

Figure 3.1: Flexural properties of TβRII$^{ocy-/-}$ bone. (A) Stress-strain curves from femurs tested in 3-point bending, where lines represent the average of five bones. (B) Bending modulus and (C) yield stress parameters were calculated from the same five animals. (D) Tissue elastic modulus was measured by nanoindentation for n=3 bones. Graphs show mean +/- SD. *$p<0.05$.

In addition to flexural properties, the ability of bones to resist fracture depends on their ability to absorb energy as they deform, called toughness. To evaluate the role of osteocyte-intrinsic TGFβ signaling in fracture toughness, we used *in situ* fracture toughness tests, which allow simultaneous observation of the crack growth from a predefined notch and quantitative measurement of force required to propagate the crack. Overall, these tests demonstrated that TβRII$^{ocy-/-}$ cortical bone has a significant 65% reduction in work of fracture compared with WT bone (Figure 3.2 A).

Calculation of the crack-resistance curve (R-curve) allows for comparison of the crack initiation toughness and crack growth toughness between genotypes (Figure 3.2 B). While R-curves are often shown in terms of the stress intensity factor K, the small geometry of mouse bones used here makes measurement of K strictly invalid. Therefore, R-curves were calculated in terms of work of fracture.

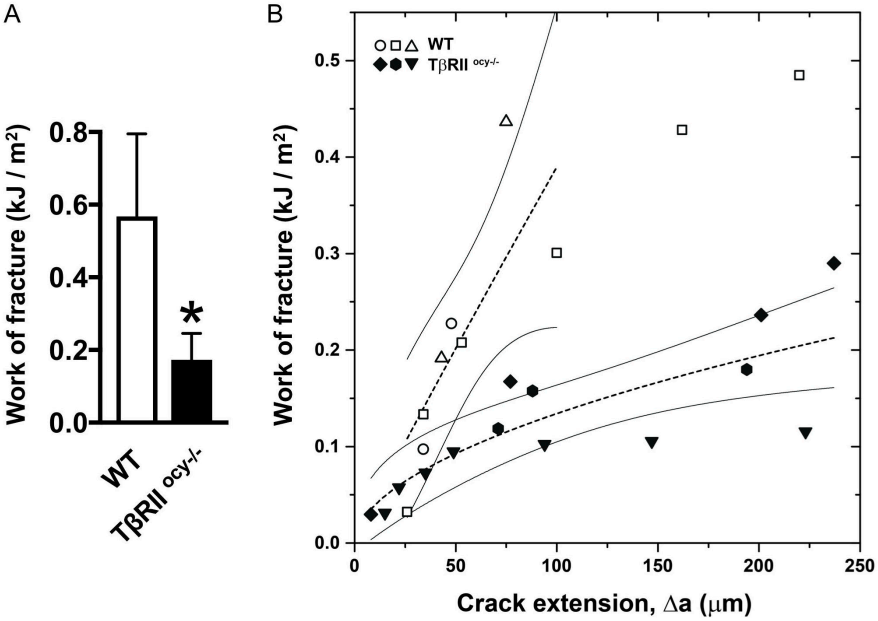

Figure 3.2: Fracture toughness of TβRII$^{ocy-/-}$ bone. (A) Work of fracture calculated from notched 3-point bending tests. Graph shows mean +/- SD, n=5, *p<0.05. (B) R-curves from in situ fracture toughness testing. Graph shows 95% confidence intervals calculated based on a power fit, n=3.

Crack initiation toughness is primarily determined by a material's intrinsic toughening mechanisms, such as small-scale plastic deformation, which act ahead of the crack tip to increase resistance to microstructural damage. The crack initiation toughness can be determined from the R-curve as the crack extension approaches 0 but could not be conclusively differentiated between WT and TβRII$^{ocy-/-}$ bone in this study. Crack growth toughness is largely determined by extrinsic toughening mechanisms, such as crack bridging, which act behind the crack tip in order to shield the crack from the applied force. Crack growth toughness manifests in the slope of the R-curve, which was significantly lower for TβRII$^{ocy-/-}$ bone than wildtype (Figure 3.2 B).

Differences in extrinsic toughening were also apparent from qualitative changes in crack growth. Specifically, in 100% of WT bones, crack extension was accompanied by crack deflection and uncracked ligament bridging. In TβRII$^{ocy-/-}$ bone, uncracked ligament bridging occurred less often and in some mice was entirely absent. Both genotypes displayed a similar number of crack deflections during extension, but the crack angle tended to be smaller and deflections more parallel to the crack extension in TβRII$^{ocy-/-}$ bone. We quantified this effect with the ratio of the crack path length relative to maximum crack extension, which was 35% lower in TβRII$^{ocy-/-}$ bone than in wildtype bone (Figure 3.3). Collectively these analyses show defects in multiple aspects of bone quality in mice with an osteocyte-intrinsic defect in TGFβ signaling.

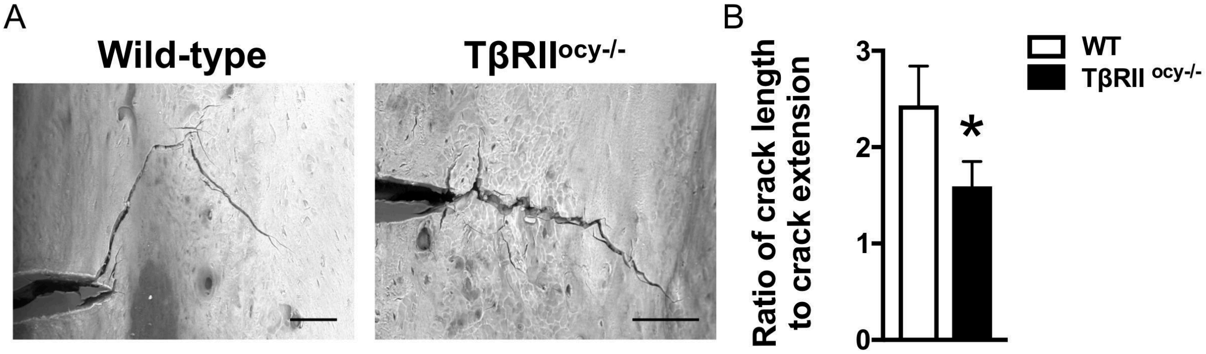

Figure 3.3: Loss of crack deflection in TβRII$^{ocy-/-}$ bone. (A) Representative SEM images of crack paths extending from preformed notches in mouse femurs during in situ fracture toughness testing. Scale bar = 100 μm. (B) Quantification of crack path length relative to extension. Graph shows mean +/- SD, n=5, *p<0.01.

Discussion

This study advances our understanding of bone fragility by identifying osteocytes as major cellular mediators of bone quality. In mice with an osteocyte-specific ablation of TβRII, the bone quality contributors flexural strength, elastic modulus, and fracture toughness were reduced. These results confirm the importance of homeostatic TGFβ signaling and the role of osteocytes in maintaining bone quality. Therefore targeting osteocytes with future therapeutics may improve bone resistance to fracture in cases where fragility accompanies normal bone mass.

These results using an osteocyte-specific defect in TGFβ signaling complement prior studies that demonstrate the importance of homeostatic TGFβ for maintenance of bone quality. Together these studies show dose-dependent and cell type-specific responses to changes in TGFβ signaling (6, 7, 9). While these prior studies suggested that systemic suppression of TGFβ signaling increases tissue elastic modulus and toughness, this work was the first to isolate the role of osteocytes. Therefore, this approach may have disrupted intricate TGFβ -mediated cellular coordination that was maintained during systemic interventions.

In addition to material bone quality defects, TβRII$^{ocy-/-}$ bone demonstrated reductions in hallmarks of PLR including organization of the lacunocanalicular network and expression of PLR genes such as Mmp13 (17). These results were similar to bones from mice with systemic ablation of Mmp13, which have disorganized collagen and canaliculi and reduced fracture toughness (11). Therefore, TGFβ likely regulates bone quality through its control of osteocyte PLR. The mechanisms by which PLR contributes to extrinsic toughening, as well as the specific contributions of each protease downstream of TGFβ, remain to be determined.

References

1. Zimmermann EA, Busse B, Ritchie RO (2015) The fracture mechanics of human bone: influence of disease and treatment. *Bonekey Rep* 4. doi:10.1038/bonekey.2015.112.
2. Hernandez CJ, Keaveny TM (2006) A biomechanical perspective on bone quality. *Bone* 39(6):1173–1181.
3. Fonseca H, Moreira-Gonçalves D, Coriolano HJA, Duarte JA (2014) Bone quality: The determinants of bone strength and fragility. *Sport Med* 44(1):37–53.
4. Alliston T (2014) Biological regulation of bone quality. *Curr Osteoporos Rep*. doi:10.1007/s11914-014-0213-4.
5. Currey JD (1979) Mechanical properties of bone tissues with greatly differing functions. *J Biomech* 12(4):313–319.
6. Mohammad KS, et al. (2009) Pharmacologic inhibition of the TGF-beta type I receptor kinase has anabolic and anti-catabolic effects on bone. *PLoS One* 4(4):e5275.
7. Edwards JR, et al. (2010) Inhibition of TGF-b signaling by 1D11 antibody treatment increases bone mass and quality in vivo. *J Bone Miner Res* 25(11):2419–2426.
8. Tang SY, Alliston T (2013) Regulation of postnatal bone homeostasis by TGFβ. *Bonekey Rep* 2. doi:10.1038/bonekey.2012.255.
9. Balooch G, et al. (2005) TGF-beta regulates the mechanical properties and composition of bone matrix. *Proc Natl Acad Sci U S A* 102(52):18813–18818.
10. Chang JL, et al. (2010) Tissue-specific calibration of extracellular matrix material properties by transforming growth factor-beta and Runx2 in bone is required for hearing. *EMBO Rep* 11(10):765–771.

11. Tang SY, Herber R-P, Ho SP, Alliston T (2012) Matrix Metalloproteinase-13 is Required for Osteocytic Perilacunar Remodeling and Maintains Bone Fracture Resistance. *J Bone Miner Res* 27(9):1936–1950.

12. Qing H, et al. (2012) Demonstration of osteocytic perilacunar/canalicular remodeling in mice during lactation. *J Bone Miner Res* 27(5):1018–1029.

13. Inoue K, et al. (2006) A crucial role for matrix metalloproteinase 2 in osteocytic canalicular formation and bone metabolism. *J Biol Chem* 281(44):33814–33824.

14. Holmbeck K, et al. (2005) The metalloproteinase MT1-MMP is required for normal development and maintenance of osteocyte processes in bone. *J Cell Sci* 118(Pt 1):147–156.

15. Nyman JS, et al. (2011) Differential effects between the loss of MMP-2 and MMP-9 on structural and tissue-level properties of bone. *J Bone Miner Res* 26(6):1252–1260.

16. Li CY, et al. (2006) Mice Lacking Cathepsin K Maintain Bone Remodeling but Develop Bone Fragility Despite High Bone Mass. *J Bone Miner Res* 21(6):865–875.

17. Dole NS, et al. (2017) Osteocyte intrinsic TGFβ signaling regulates bone quality through perilacunar/canalicular remodeling. *Cell Rep* 21(9):2585–2596.

18. Ritchie RO, et al. (2008) Measurement of the toughness of bone: a tutorial with special reference to small animal studies. *Bone* 43(5):798–812.

19. Turner CH, Burr DB, Turner CH (1993) Basic Biomechanical Measurements of Bone: A Tutorial. *Bone* 14:595–608.

20. Oliver WC, Pharr GM (1992) An improved technique for determining hardness and elastic modulus using load and displacement sensing indentation experiments. *J Mater Res* 7(6):1564–1583.

Chapter 4

Osteocytes in skeletal disease

This chapter is based on work in two peer-reviewed publications:

Fowler et al. Glucocorticoid suppression of osteocyte perilacunar remodeling is associated with subchondral bone degeneration in osteonecrosis. *Sci Rep*. 7, 44618 (2017).

Alemi et al. Glucocorticoids cause mandibular bone fragility and suppress osteocyte perilacunar-canalicular remodeling. *Bone Rep*. 9: 145–153 (2018).

Introduction

A growing body of evidence establishes that functional osteocytes are essential for skeletal homeostasis. As discussed in Chapter 3, suppression of TGFβ signaling severely impairs osteocyte perilacunar/canalicular remodeling (PLR) and bone material properties (1). Systemic ablation of just one PLR enzyme, Mmp13, reduces organization of the lacunocanalicular network and collagen in the bone extracellular matrix and causes fragility (2). Expression of MMP13 by osteocytes in at least some bones is necessary for resorption of the lacunar walls to meet the high metabolic demand of lactation (2). In skeletal diseases, however, effects on or by osteocytes are largely unknown. Since osteocytes are such important regulators of bone, we hypothesized that they could also play a causal role in disease. We set out to address this gap in understanding by examining the role of PLR in glucocorticoid-induced skeletal disease.

Glucocorticoid (GC) treatment is a major risk factor for osteonecrosis (ON), in which bone tissue dies, mechanically fails, and eventually causes painful collapse of overlying articular cartilage. Degeneration of osteonecrotic bone is not currently reversible, and it often necessitates joint replacement surgery or other reconstruction for relatively young patients. Also called avascular necrosis, the traditional understanding of ON is that interrupted bloodflow in the bone begins a cascade of cell death (3). In end-stage disease, apoptosis of osteoblasts and osteocytes has been observed adjacent to the collapsed bone (4), leading to the hypothesis that osteocyte death is one of the main mechanisms driving GC-induced ON. However, osteocyte death and other observed changes to osteoblasts, osteoclasts, and vasculature do not fully explain the intricacies of the ON phenotype, which includes sclerotic zones and reduction in tissue elastic modulus. Since mice with ablation of Mmp13 and with osteocyte-specific inhibition of TGFβ signaling also show changes to bone mineralization and material properties, our group hypothesized that GCs affect osteocyte PLR before the appearance of other ON symptoms.

One of the major sites of GC-induced ON is the hip, but ON can also occur in the mandible as a severe complication of radiation therapy. The mesodermally-derived femur and the neural crest-derived mandible are specialized for very different functions, and previous work demonstrated that PLR can be regulated in a site-specific manner (5). Therefore, we examined both femoral and mandibular bone to learn about the role of PLR in skeletal disease.

Methods

Mice

Male FVB mice were purchased from Jackson labs and acclimatized in the UCSF LARC for at least one week. At 8 weeks old, mice were anesthetized with inhaled isofluorane, and slow-release pellets of placebo or the gluococorticoid prednisolone (Innovative Research of America, 2.8 mg/kg/day) were subcutaneously implanted. After 7, 21, 35 or 55 days of treatment, mice were euthanized and humeri, femurs, and mandibles were collected.

Flexural testing

For mechanical testing, bones were collected from mice treated with placebo or prednisolone for 35 days. Femurs were gently dissected and muscle carefully removed to avoid scratching the bone surface, then stored in HBSS at 4 °C for up to one month. The temporomandibular joints were gently dislocated and the hemimandibles separated between the incisors. Muscle was carefully removed to avoid scratching the bone surface. Hemimandibles were stored in HBSS at 4 °C for up to one month.

All bones were brought to room temperature prior to testing. Femurs were positioned on a 6-mm span with the central loading point at the mid-diaphysis and the posterior side in tension. Hemimandibles were positioned on a 4-mm span with the buccal side facing up (buccal compression) and the central loading point at the midpoint of the molars. Stiffness was calculated from the slope of the load-displacement curve using a custom Python script, and ultimate load was defined as the maximum bending load sustained.

I conducted extensive protocol development and optimization for mandible mechanical testing prior to testing of experimental samples. Based on this, I chose a 4-mm span and buccal compression for both physiological relevance and to minimize technical variability. However, I still observed technical variation in mandible failure that was unrelated to bone material or mechanical behavior. To control for this, experimental samples were included for analysis if the fracture occurred immediately posterior to the molars without preceding fracture of the condylar process or angular process (Figure 4.1 A). Hemi-mandibles from the same animal were treated as technical replicates and averaged together for final comparisons.

Quantitative RT-PCR analysis

Humeri from mice treated with placebo and prednisolone for 7 days were quickly cleaned of muscle, periosteum, and marrow and stored in liquid nitrogen. Bones were homogenized in TRIzol, and purified as described in Chapter 2. qPCR was performed with SYBR primers (Table 2.3). Expression was quantified by the ΔΔCt method with L19 as the housekeeping gene.

Cells

MLO-Y4 osteocytic cells were cultured as described in Chapter 2. To set up each experiment, cells were trypsinized, counted, and replated into collagen type I-coated 6-well plates at 50,000 cells/well. The next day, media was replaced and cells were pre-treated with 1 μM of the caspase-3 inhibitor DEVD or vehicle (PBS) for 30 minutes. The glucocorticoid dexamethasone (Dex) was dissolved in sterile water and applied to wells at a final concentration of 0.1 μM or 1 μM. An equal volume of vehicle (water) was used in control wells. All wells were harvested after 24 hours of Dex treatment for mRNA analysis or measurement of cell death.

To quantify cell death, nonadherent cells were collected from each well prior to trypsinization of cells adhered to the culture dish. The trypsinized cells were collected with media containing serum and combined with the nonadherent cells before centrifugation. Each cell pellet was resuspended in an equal volume of media and diluted in 0.4% trypan blue stain. Cells containing and excluding trypan blue stain were counted using a hemacytometer, with eight measurements made for each replicate of each condition.

Histological analyses

For histology, femurs and hemimandibles from mice treated with placebo or prednisolone for 21 or 55 days were fixed in 10% neutral buffered formalin, decalcified, paraffin-embedded, and sectioned, as described in Chapter 2. Cortical bone analysis was performed on axial femoral sections at the mid-diaphysis and on sagittal sections on the inferior border of the mandible. Immunohistochemistry was performed with antibodies for MMP13 and Cathepsin K (Table 2.2). Ploton silver stain and picrosirius red stain were performed as described in Chapter 2.

To quantify changes in the lacunocanalicular network, greyscale images of silver-stained sections were thresholded in ImageJ. In femurs, the orientation of dark silver-stained canaliculi was compared and their area relative to total bone area per image was compared. In mandibles, the area of stained lacunae and canaliculi was normalized to total bone area for each image.

Results

In the sclerotic bone of human femoral heads with stage IV osteonecrosis, histologic hallmarks of PLR were severely repressed compared to regions of healthy bone. Osteocyte expression of MMP13 was reduced, collagen organization was disrupted, lacunar volume was smaller, and canaliculi were shorter and less numerous than in adjacent normal bone. However, contrary to prior reports, osteocytes appeared viable (6). The disruption of PLR hallmarks in end-stage human disease establishes that osteocytes are affected by glucocorticoid treatment, possibly independent of apoptosis.

To learn whether osteocytes and PLR play a causal role in GC-induced skeletal disease, we treated mice with the glucocorticoid prednisolone or with placebo pellets implanted subcutaneously for 7-55 days. At 35 days of treatment, we found that mandibles and femurs from prednisolone-treated mice were significantly more fragile than those from placebo-treated mice (Figure 4.1), suggesting efficacy of our osteonecrosis model. For unknown reasons, neither ultimate load of mandibles (p=0.23) nor stiffness of femurs (p=0.18) different significantly between treatments.

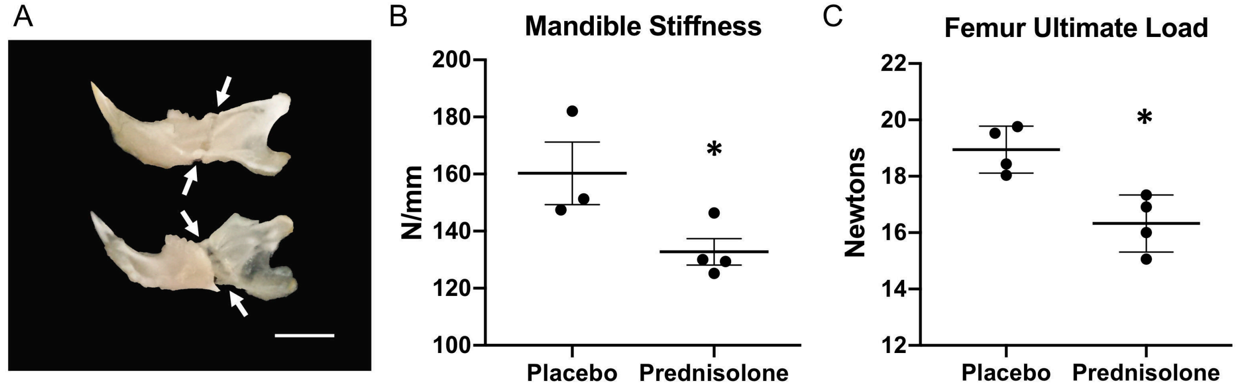

Figure 4.1: Flexural properties of placebo and prednisolone-treated bones. (A) Examples of mandible fracture locations included for analysis. Scale bar = 4 mm. (B) Stiffness of mouse mandibles after 35 days of glucocorticoid treatment. Points represent the average of two hemimandibles from one animal. n=3 animals for placebo, n=4 animals for prednisolone. Graph shows mean +/- SEM. (C) Ultimate load of mouse femurs after 35 days of glucocorticoid treatment. Points each represent one femur. n=4. Graph shows mean +/- SD. $^*p<0.05$.

Since prior animal studies often focused on osteocyte apoptosis in response to GCs (7, 8), we used TUNEL staining to measure cell death. We found a significant increase in the percentage of TUNEL-positive osteocytes in trabecular bone, which agrees with prior studies. However in femoral cortical bone, no increase in osteocyte death was observed with 7 or 21 days of treatment (6). This suggests that any early effects of glucocorticoid treatment in cortical bone occur independent of apoptosis.

After just 7 days of treatment, we observed severe changes in osteocyte behavior. As expected, the GC-induced gene Gilz was significantly upregulated. Expression of matrix metalloproteinases (Mmp)-2, -13 and -14, Cathepsin K (Ctsk), and tartrate-resistant acid phosphatase (Acp5) mRNA was repressed 25-80% in bone from GC-treated mice compared to placebo-treated mice, consistent with repression of PLR (Figure 4.2 A). Interestingly, carbonic anhydrase II (Car2), which was co-regulated with these other genes in a lactation model of PLR induction (9), was upregulated in the GC-treated bone, perhaps as a compensatory mechanism. These changes in transcriptional activity preceded detectable loss of bone mass in the femur and mandible with microCT (6, 10).

To further determine whether the observed changes in gene expression after GC treatment were osteocyte-intrinsic and independent of apoptosis, we cultured MLO-Y4 osteocytes with the GC dexamethasone with or without the caspase-3 inhibitor DEVD. 24 hours of dexamethasone treatment repressed Mmp13 expression in MLO-Y4 cells in a dose-dependent manner (Figure 4.2 B). Pre-treatment with DEVD effectively blocked apoptosis of MLO-Y4 cells (Figure 4.2 C) without affecting the repression of Mmp13. These *in vitro* results further support that GC-induced changes in osteocyte activity can occur independently of apoptosis.

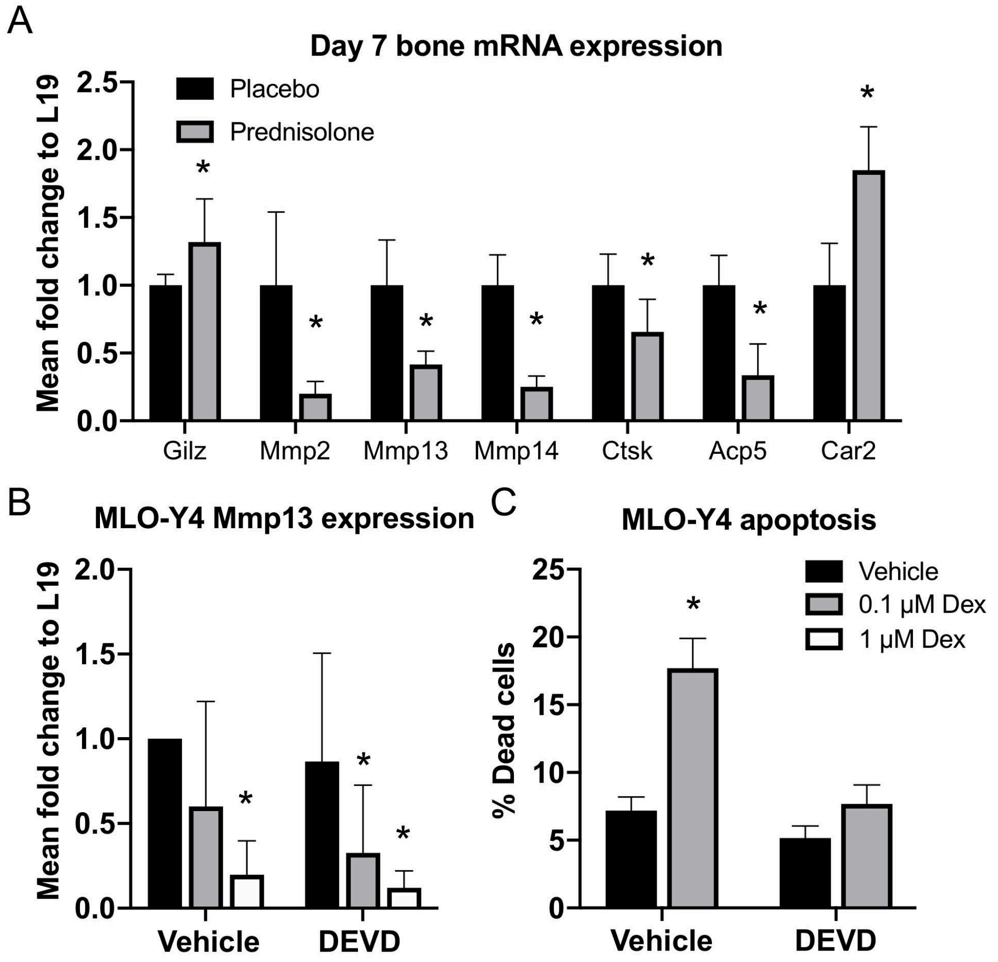

Figure 4.2: Gene expression in bones and MLO-Y4 osteocytes treated with glucocorticoids. (A) Mean fold change gene expression in bone from prednisolone and placebo-treated mice. n=6. (B) Mean fold change Mmp13 expression in MLO-Y4 cells treated with dexamethasone +/- DEVD for 24 hours. n=3 experiments. (C) Apoptosis in MLO-Y4 cells after 24 hours of Dex treatment was blocked by DEVD. n=3 experiments. Graphs show mean +/- SD. *p<0.05.

Hypermineralization of glucocorticoid-treated bone also develops rapidly. After 7 days of treatment in trabecular bone, and after 21 days of treatment in cortical bone, peak mineral density is increased in mice administered prednisolone (6). This finding is particularly significant because sclerosis is detectable in end-stage human disease, and it may persist from shortly after initiation of treatment.

Beginning at 21 days of treatment, we began to observe histological changes consistent with repressed PLR. Expression of MMP13 protein in osteocytes was reduced by 30-60% in the cortical bone of femurs and mandibles and remained repressed in mandibular bone after 55 days of prednisolone treatment (Figure 4.3). Cathepsin K protein expression was also lower in the mandibles of GC-treated mice at 55 days (10). The organization of the extracellular matrix was also severely altered. Collagen fibers, which are aligned with axial cross-sections of the femur in control mice, were broken and disorganized in femoral cortical and trabecular bone from GC-treated mice (6). The lacunocanalicular network in trabecular and cortical bone of femurs and mandibles was visibly degenerated, with significantly reduced area and canalicular alignment (Figure 4.4)(6). The disruption of osteocyte behavior and maintenance of the extracellular matrix induced by GCs is consistent with repression of PLR seen in MMP13-deficient mice and may eventually contribute to collapse of the tissue.

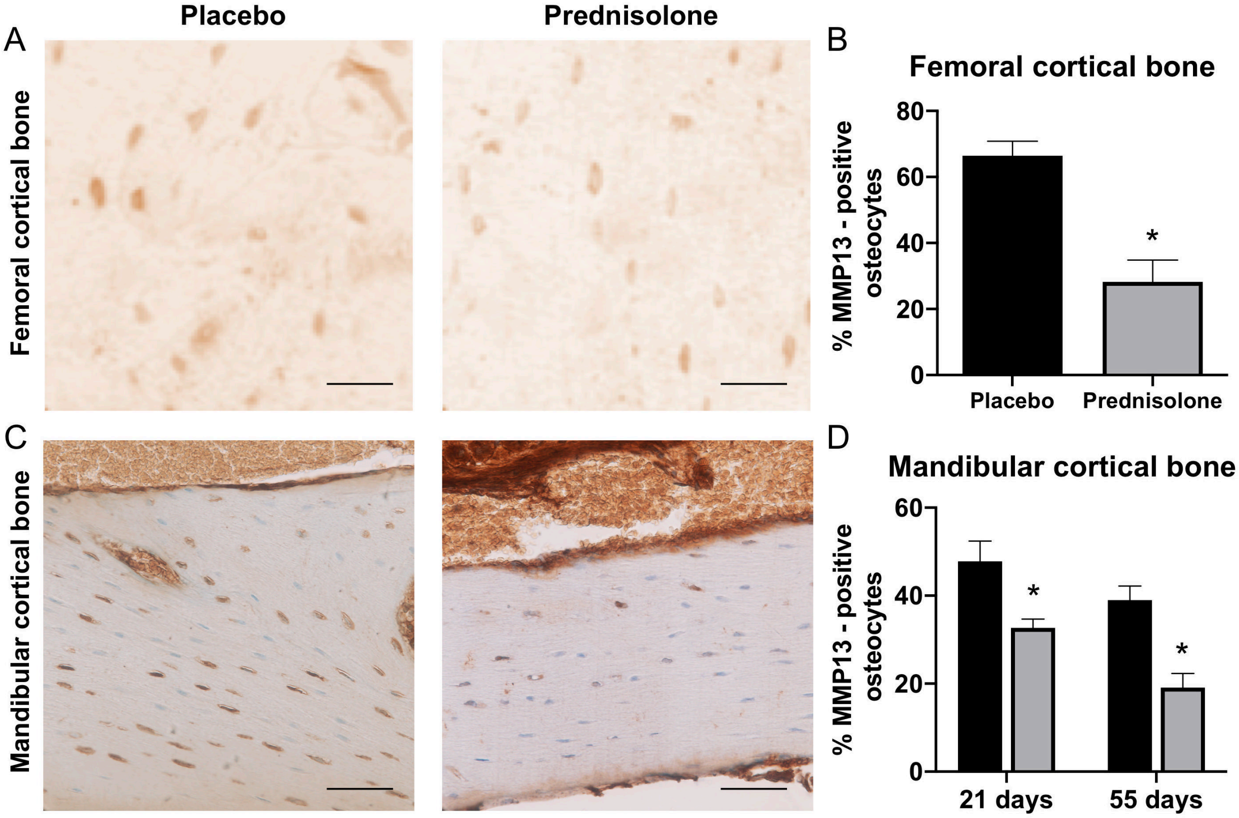

Figure 4.3: MMP13 expression in murine femoral and mandibular cortical bone treated with placebo or prednisolone. (A, C) Representative images of immunohistochemistry for MMP13 in bones from mice treated for 21 days. Scale bars = 20 µm. (B) Quantification of MMP13-expressing osteocytes in femoral cortical bone, n=4. (D) Quantification of MMP13-expressing osteocytes in mandibular cortical bone after 21 and 55 days of treatment, n ≥ 5. Graphs show mean +/- SEM. *p<0.05.

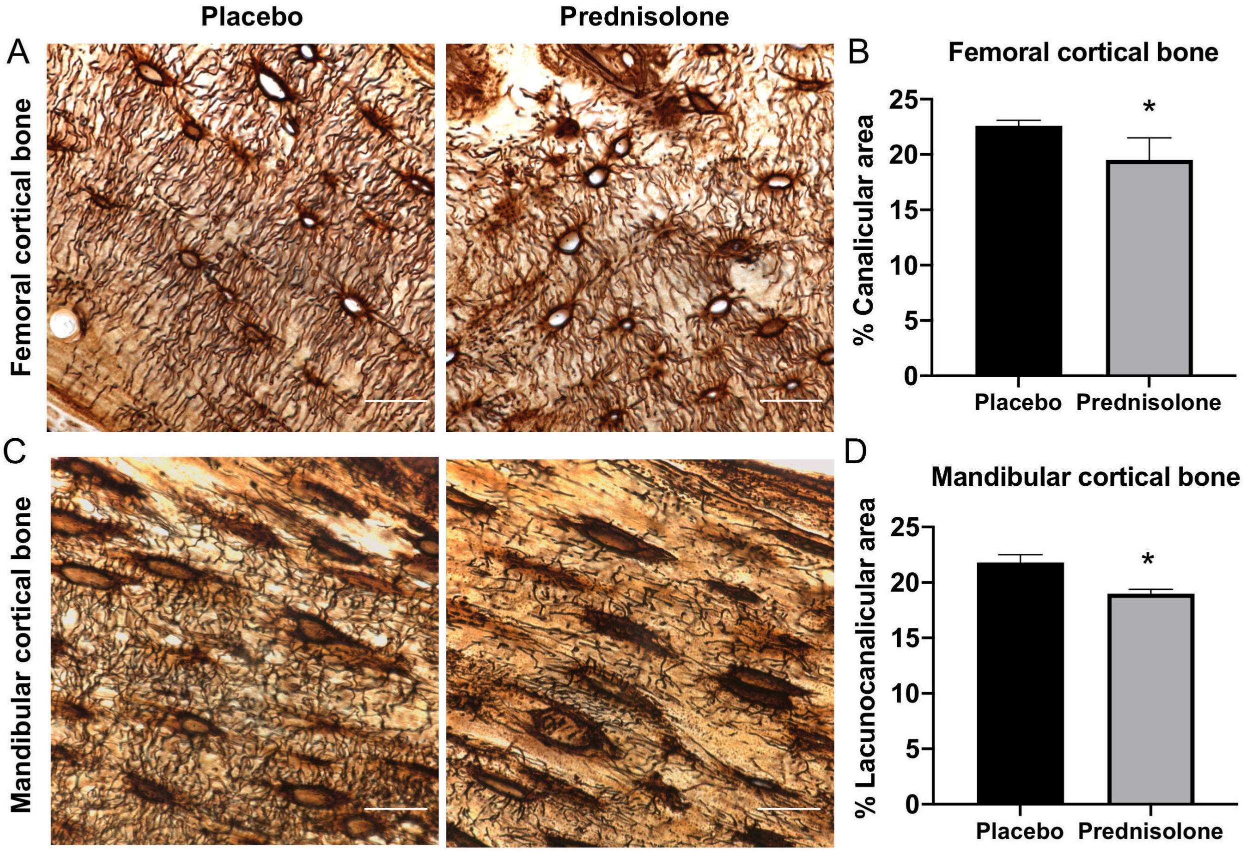

Figure 4.4: Lacunocanalicular network morphology in murine femoral and mandibular cortical bone treated with placebo or prednisolone. (A, B) Representative images and quantification of canalicular area in femoral cortical bone from mice treated with prednisolone or placebo for 21 days, n≥3. (C, D) Representative images and quantification of lacunocanalicular area in mandibular cortical bone from mice treated with prednisolone or placebo for 55 days, n≥5. Scale bars = 20 μm. Graphs show mean +/- SEM. $^*p<0.05$.

Therefore, glucocorticoid treatment affects hallmarks of PLR including gene expression, protein expression, mineralization, and tissue organization in both the mesodermally-derived femur and neural crest-derived craniofacial bone. Reduction of flexural strength of mandibles and femurs occurred after repression of genes and proteins associated with PLR, and so GC-related fragility may also derive from defects in PLR. Particularly in cortical bone, where increases in osteocyte apoptosis were not observed over the same timeline, these results suggest that osteocytes are active participants in the progression of disease and bone fragility, rather than victims of glucocorticoid-induced osteonecrosis.

Discussion

The existing paradigm for glucocorticoid-induced osteonecrosis argues that high-dose GC treatment causes vascular defects and osteocyte apoptosis, which subsequently lead to bone degeneration and joint collapse. Here we showed that even before bone fragility and before significant osteocyte apoptosis, glucocorticoids affect osteocyte PLR, suggesting a causal role for suppression of PLR in the development of skeletal diseases like ON. While PLR is in some cases regulated in a site-specific manner (5), we showed that osteocytes in tissues with different mechanical demands and derived from different germ layers are both susceptible to GCs. GC-induced ON may eventually be understood as a disease in which osteocytes fail to maintain their extracellular matrix, resulting in mechanical failure of the tissue. With osteocyte dysfunction identified as a possible causal driver of osteonecrosis, this suggests that multiple skeletal diseases may be impacted by osteocyte PLR. However, the systemic nature of GC treatment prevents definitive attribution of these bone defects to osteocytes alone, so future studies of osteocytes in disease will need to utilize cell-targeted approaches.

References

1. Dole NS, et al. (2017) Osteocyte intrinsic TGFβ signaling regulates bone quality through perilacunar/canalicular remodeling. *Cell Rep* 21(9):2585–2596.
2. Tang SY, Herber R-P, Ho SP, Alliston T (2012) Matrix Metalloproteinase-13 is Required for Osteocytic Perilacunar Remodeling and Maintains Bone Fracture Resistance. *J Bone Miner Res* 27(9):1936–1950.
3. Mankin HJ (1992) Nontraumatic Necrosis of Bone (Osteonecrosis). *N Engl J Med* 326(22):1473–1479.
4. Weinstein RS, Nicholas RW, Manolagas SC (2000) Apoptosis of Osteocytes in Glucocorticoid-Induced Osteonecrosis of the Hip. *J Clin Endocrinol Metab* 85(8):2907–2912.
5. Jauregui EJ, et al. (2016) Parallel mechanisms suppress cochlear bone remodeling to protect hearing. *Bone* 89:7–15.
6. Fowler TW, et al. (2017) Glucocorticoid suppression of osteocyte perilacunar remodeling is associated with subchondral bone degeneration in osteonecrosis. *Sci Rep* 7:44618.
7. Plotkin LI, Manolagas SC, Bellido T (2007) Glucocorticoids induce osteocyte apoptosis by blocking focal adhesion kinase-mediated survival. Evidence for inside-out signaling leading to anoikis. *J Biol Chem* 282(33):24120–24130.
8. O’Brien CA, et al. (2004) Glucocorticoids act directly on osteoblasts and osteocytes to induce their apoptosis and reduce bone formation and strength. *Endocrinology* 145(4):1835–1841.
9. Qing H, et al. (2012) Demonstration of osteocytic perilacunar/canalicular remodeling

in mice during lactation. *J Bone Miner Res* 27(5):1018–1029.

10. Alemi AS, et al. (2018) Glucocorticoids cause mandibular bone fragility and suppress osteocyte perilacunar-canalicular remodeling. *Bone Reports* 9:145–153.

Chapter 5

Osteocyte dysfunction promotes osteoarthritis through MMP13-dependent suppression of subchondral bone homeostasis

This chapter is taken from the peer-reviewed article of the same name, by Courtney M. Mazur, Jonathon J. Woo, Cristal S. Yee, Aaron J. Fields, Claire Acevedo, Karsyn N. Bailey, Serra Kaya, Tristan W. Fowler, Jeffrey C. Lotz, Alexis Dang, Alfred C. Kuo, Thomas P. Vail, and Tamara Alliston, published in *Bone Research*.

Introduction

Osteoarthritis (OA), the most common chronic joint disease, is a leading cause of pain and disability worldwide (1). OA irreversibly damages articular cartilage and the surrounding tissues, compromising joint function and mobility of over 30 million Americans (2). Abundant research efforts have investigated cartilage and its interactions with other joint tissues in order to understand the underlying mechanisms of OA initiation and progression (3–5). Still, no permanent disease-modifying therapies exist short of joint replacement.

A major question in the field is the extent to which subchondral bone plays a causal role in the pathogenesis of OA. Though much correlative evidence indicates the coordinated degradation of subchondral bone and cartilage (3, 6), causality is difficult to ascertain because analyses are often conducted on tissues with end-stage disease or in models in which both the bone and cartilage are affected. Recent studies have illuminated that biological (7) and mechanical (8) changes to the subchondral bone can precede degradative changes to overlying cartilage. However, the cellular mechanisms responsible for OA-related changes in subchondral bone, and particularly the role of osteocytes, remain unclear.

Recent reports have reinvigorated interest in the active role of osteocytes in remodeling their surrounding bone matrix – a process called perilacunar/canalicular remodeling (PLR) (9–12). PLR is a dynamic process by which osteocytes secrete matrix metalloproteinases (MMPs) (13–15), cathepsin K (CatK) (10), and other enzymes (16, 17) to dynamically resorb and then replace the local bone matrix. PLR maintains bone material properties (13, 18, 19), systemic mineral homeostasis (10, 12), and the canalicular channels that facilitate osteocyte communication, mechanosensation, and nourishment (9, 20, 21). Several known regulators of bone homeostasis, including TGF-β (19), SOST (17), parathyroid hormone (10, 22), and Vitamin D (23, 24), regulate PLR to support the metabolic and mechanical function of the skeleton. Although PLR is a fundamental mechanism by which osteocytes maintain bone homeostasis, its role in the maintenance of subchondral bone and the progression of joint disease remain unclear.

To elucidate the role of PLR in disease, we previously investigated osteonecrosis, a progressive and severe joint disease in which subchondral bone mechanically fails with painful collapse of the articular surface (25, 26). We found that glucocorticoids, a major risk factor associated with osteonecrosis (25), suppress PLR and cause the same changes in subchondral bone of mice as seen in glucocorticoid-induced human osteonecrosis (27). Although suppression of PLR is clearly associated with the degradation of subchondral bone in osteonecrosis, it was not possible to isolate the effects of osteocytes from the systemic influence of glucocorticoids. Given that the health of articular cartilage depends upon subchondral bone for mechanical and vascular support (28, 29), we hypothesized that signs of PLR dysregulation may also accompany the much more common joint disease, osteoarthritis. We tested this hypothesis by examining specific hallmarks of PLR suppression and their relationship to cartilage degeneration in OA of the human knee. As a step towards evaluating the causality of PLR suppression in joint disease, we evaluated the bone and joint phenotypes of a novel mouse model with ablation of the critical PLR enzyme MMP13 from osteocytes but not chondrocytes. Together, our results demonstrate the causal role of osteocyte-derived MMP13 in the pathogenesis of OA, suggesting the importance of osteocyte perilacunar/canalicular remodeling for joint homeostasis.

Results

Degeneration of the osteocyte lacunocanalicular network in human osteoarthritis

To determine if osteocytic PLR is affected by osteoarthritis (OA) in humans, we compared subchondral bone in tibial plateaus from patients with end-stage OA to that of cadaveric donors with no clinical evidence of joint disease. As expected, tibial plateaus from patients with OA had gross degeneration of the articular cartilage (Supp. Figure 5.1a-f) and radiographic evidence of subchondral bone sclerosis, particularly on the medial side of the joint (Supp. Figure 5.1g-i). Histological analysis confirmed the cartilage degeneration and subchondral bone sclerosis in OA specimens (Figure 5.1a). Consistent with prior reports (6), both the subchondral bone plate and trabeculae were thicker in OA than in controls (Figure 5.1a). Relative to the cadaveric controls, OA tibial plateaus showed decreased cartilage thickness, reduced Safranin-O positive proteoglycan staining in the superficial zone, and cartilage fibrillation (Figure 5.1a), resulting in significantly higher OARSI scores (Supp. Figure 5.1b). Although the control cartilage was more intact than the OA cartilage overall, the medial compartment showed more evidence of degeneration in both OA and control specimens. Therefore, the subsequent analyses of subchondral bone compared defined regions of interest between the control and OA specimens, as well as between the medial and lateral side of the same specimen.

While OA-dependent differences in osteoblast and osteoclast function have been described (3, 6), the effect of OA on osteocytes is not well-defined. Therefore, we evaluated osteocyte PLR in subchondral bone by studying one of its key hallmarks, the lacunocanalicular network (LCN). Silver staining revealed that cadaveric control subchondral bone had both more abundant and apparently longer canalicular projections than the subchondral bone from OA patients (Figure 5.1b). The dramatic degeneration of the canalicular network in OA bone was particularly evident in the medial side of the tibial plateau, where cartilage degeneration was most severe. Quantitative analysis revealed significant OA-dependent reductions in the total osteocyte lacunocanalicular area (38-46%) (Figure 5.1c) and canalicular length (51-54%) (Figure 5.1d) relative to cadaveric controls, consistent with this hallmark feature of PLR suppression (10, 13–15, 19, 27, 30). Therefore, the reduced canalicular length and lacunocanalicular area in OA subchondral bone strongly suggests that PLR is suppressed in OA.

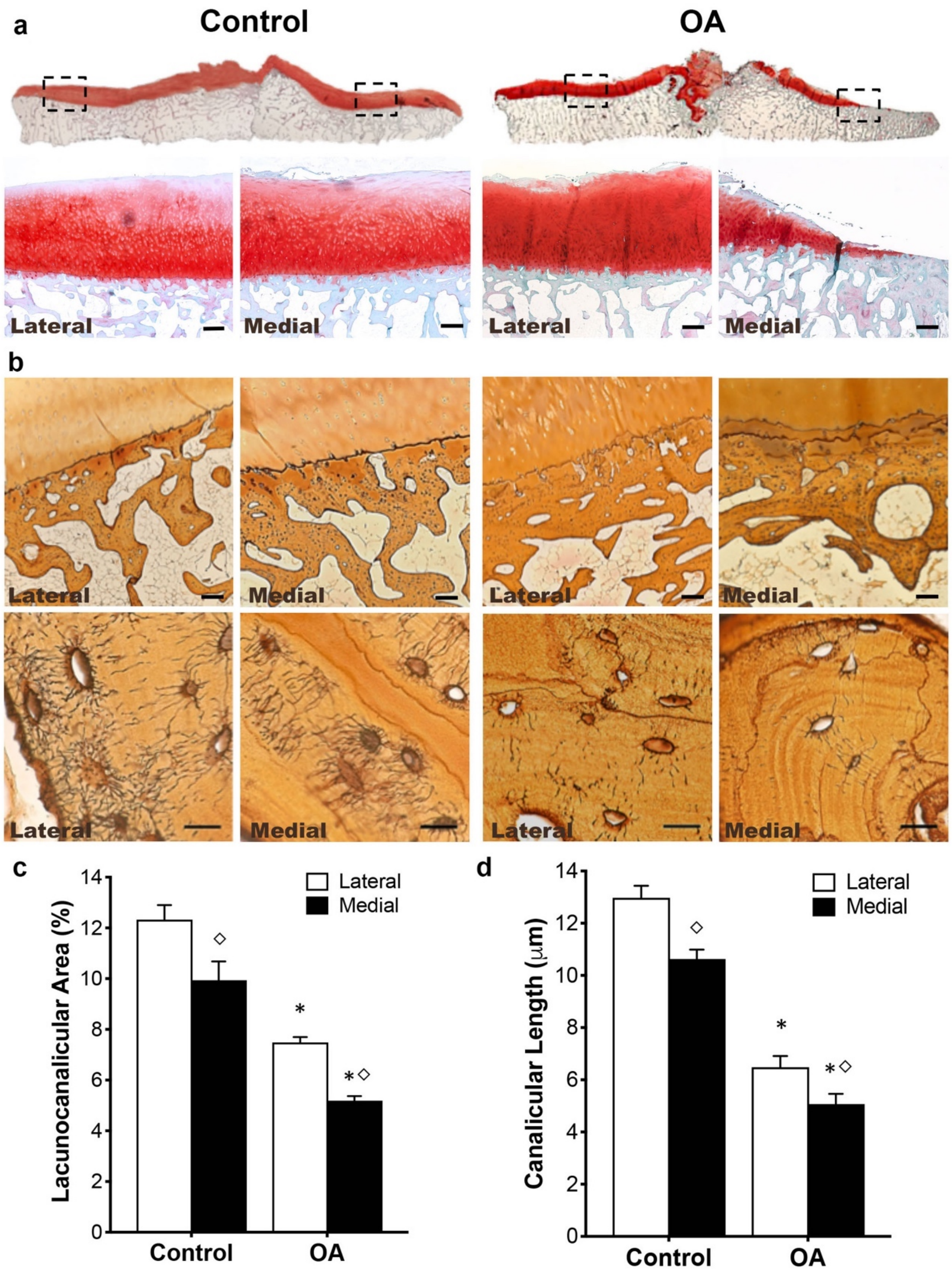

Figure 5.1: Lacunocanalicular networks are disrupted in human OA subchondral bone. (a) Control cadaveric and OA specimens stained with Safranin-O/Fast Green and imaged at 0.5x (top) or 2x (bottom, scale bars: 400 μm) magnification displayed differences in articular cartilage and subchondral bone morphology on the lateral and medial sides of the tibial plateau. Subsequent analyses compared the indicated regions of interest (black boxes on top row) between control and OA specimens, and between the less affected lateral side with the

more severely degraded medial side. (b) These identified regions of interest in Ploton silver-stained sections were evaluated at low (4x, top, scale bars: 200 μm) and high (100x, bottom, scale bars: 20 μm) magnification to visualize the lacunocanalicular network of subchondral bone. (c, d) Quantification of the lacunocanalicular area normalized to the bone area (c) and canalicular length (d) revealed significant OA-dependent reductions in both parameters (n = 5). Graphs show mean ± SEM. $^*P < 0.05$ compared with respective regions of control specimens, ⋄$P < 0.05$ between regions by Holm–Sidak post hoc tests.

Collagen disorganization and hypermineralization in human OA subchondral bone

In mouse models of PLR suppression and in human osteonecrotic subchondral bone, loss of lacunocanalicular area is often accompanied by collagen disorganization and hypermineralization of the bone extracellular matrix (ECM) (13, 27, 30). Therefore, we evaluated the organic and mineral constituents of OA subchondral bone. Birefringent collagen fibers in OA subchondral bone showed qualitatively less alignment relative to the control tissue (Figure 5.2a). Upon quantification, collagen linearity was significantly lower in OA specimens compared to control specimens on both the lateral and medial sides. Furthermore, collagen fibers were significantly less aligned on the medial side of the joint than on the lateral side in both groups (Figure 5.2b).

Consistent with these site- and disease-dependent patterns, hypermineralization of subchondral bone was most pronounced in specimens from the medial side of the OA tibial plateau (Figure 5.2d). Medial OA specimens also portrayed a rougher subchondral surface than control specimens. Statistical analysis confirms that the distribution of mineral density is significantly shifted in medial OA samples relative to lateral OA samples, but low sample size precludes quantitative comparison to control groups (Figure 5.2c). Therefore, OA is accompanied by subchondral bone collagen disorganization and is regionally associated with bone matrix hypermineralization within samples, concordant with suppressed PLR (13, 27, 30).

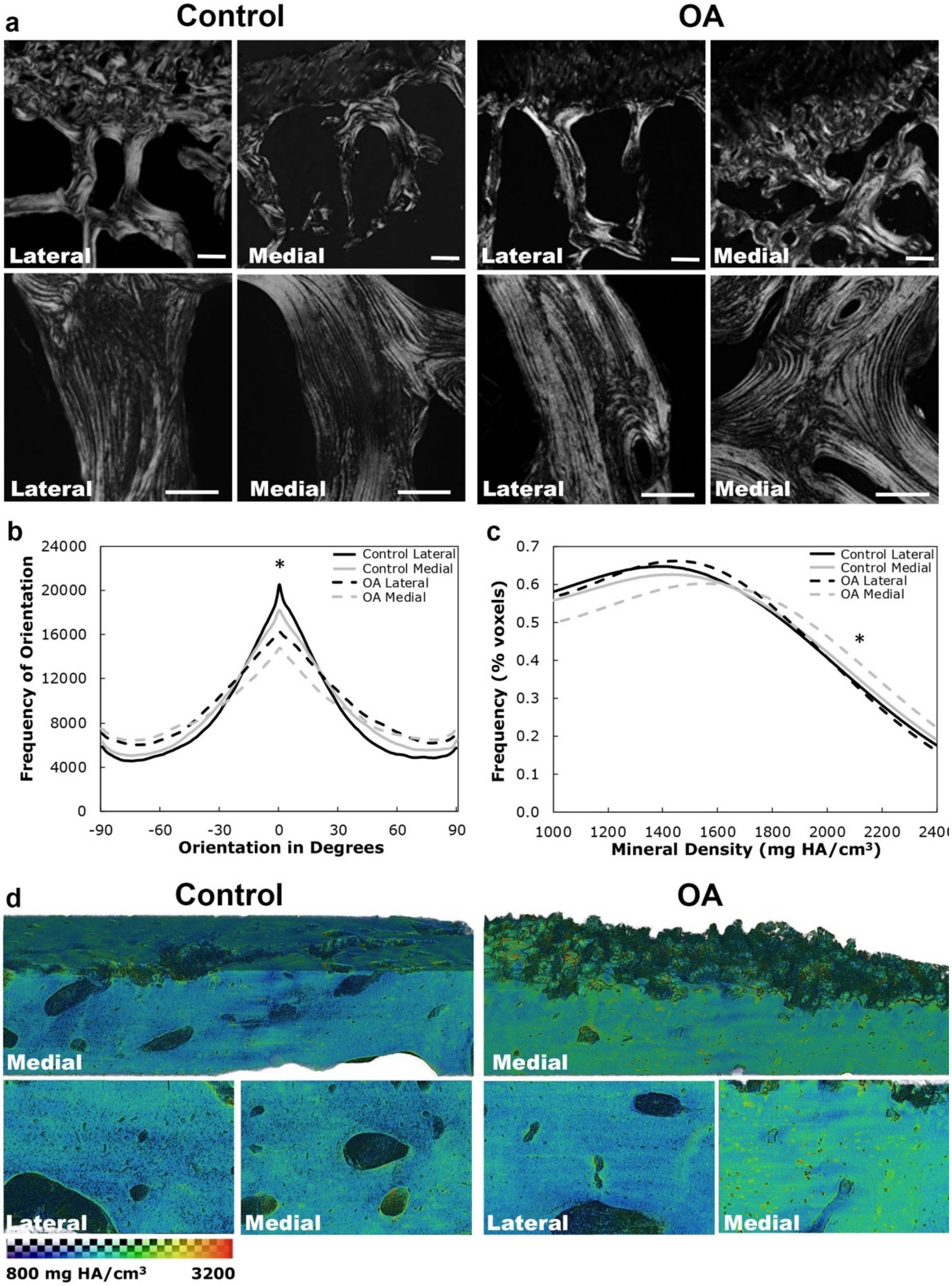

Figure 5.2: Human OA subchondral bone shows collagen disorganization and hypermineralization. (a) Control cadaveric ($n = 5$) and OA (lateral $n = 5$, medial $n = 4$) specimens stained with Picrosirius Red and imaged at low (4x, top, scale bars: 200 µm) or high (40x, bottom, scale bars: 100 µm) magnification using polarized light microscopy revealed differences in subchondral bone collagen organization. Collagen fibers are less

organized in OA samples than control samples and in medial regions than lateral regions. (b) The distribution of collagen fiber orientation shows significant differences between all four groups. (c, d) Synchrotron Radiation X-ray micro-computed tomography (SRμT) of subchondral bone from the lateral and medial sides of cadaveric control and OA tibial plateaus showed a qualitative increase in mineralization, according to the colorimetric scale (800–3 200 mg HA · cm^{-3}), in 3D-reconstructed (d, top) and 2D high-magnification (d, bottom) images. The distribution of mineralization through the subchondral bone from each region (c) confirms the shift in the peak mineralization level in OA medial specimens ($n = 5$) compared with OA lateral ($n = 4$) specimens. OA curves were not statistically compared with medial or lateral control samples due to low sample size ($n = 2$). Lines represent the mean of all specimens in the group. *$P < 0.05$ by mixed model with random intercepts.

Reduced osteocyte expression of PLR enzymes in human OA subchondral bone

Given that OA subchondral bone shows multiple signs of suppressed PLR, we sought to evaluate the expression of key enzymes implicated in PLR by osteocytes. Immunohistochemistry (IHC) revealed qualitatively lower levels of MMP13 (Figure 5.3a) and Cathepsin K (CatK, Figure 5.3c) protein expression in subchondral bone of the medial OA tibial plateau relative to healthy controls and relative to the less severely affected lateral OA tibial plateau. Accordingly, the percentage of MMP13-positive osteocytes was lower in OA subchondral bone by 20% on the medial side and 10% on the lateral side relative to their respective control sites (Figure 5.3b). The percentage of CatK-positive osteocytes was 24% lower on the medial side and 13% lower on the lateral side in OA subchondral bone compared to respective cadaveric controls (Figure 5.3d). No differences in negative control immunostaining were observed between cadaveric and OA samples (Figure 5.3e). Interestingly, the percentage of MMP13-positive osteocytes is strongly correlated with lacunocanalicular area and with canalicular length for each sample and region (Figure 5.3f-g).

Together these results suggest that human OA is correlated with PLR suppression in subchondral bone, as demonstrated by repression of key PLR enzymes in subchondral bone, loss of lacunocanalicular area, collagen disorganization, and hypermineralization. As a next step in evaluating the causality of PLR suppression in joint disease, we generated mice with a targeted deletion of MMP13 from osteocytes. We previously reported that systemic ablation of MMP13 suppresses PLR (13), however, chondrocyte expression of MMP13 contributes to cartilage degradation (31), and ablation of MMP13 in chondrocytes is chondroprotective (32, 33). Therefore, we characterized the bone and joint phenotypes of mice with a novel, osteocyte-intrinsic ablation of MMP13.

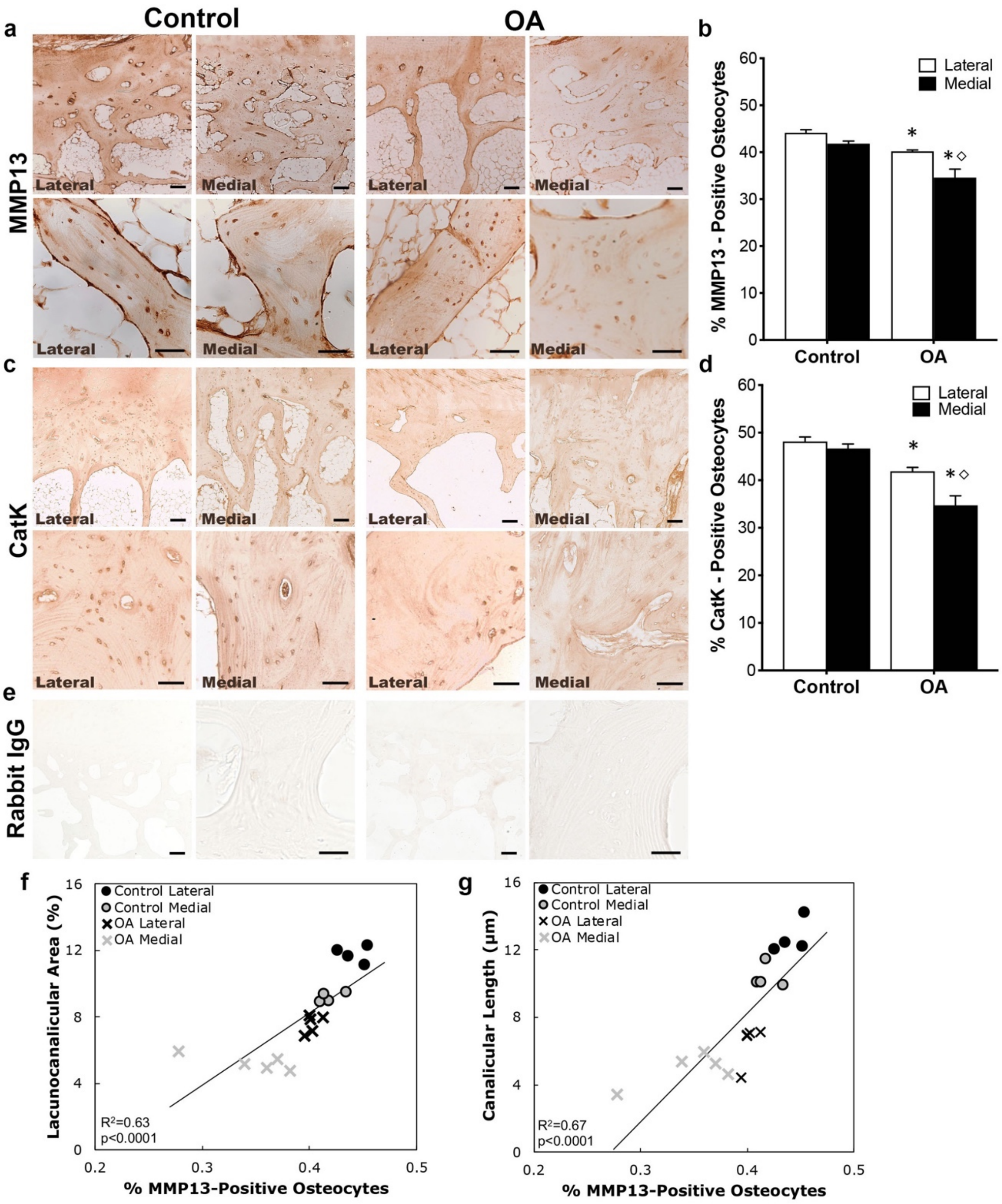

Figure 5.3: PLR enzyme expression is suppressed in human OA subchondral bone. (a–d) Immunohistochemical analysis of MMP13 (a) and Cathepsin K (CatK, c) levels and localization in subchondral bone from control and OA tibial plateau specimens was performed at low (4x, top, scale bars: 200 µm) and high (40x, bottom, scale bars: 100 µm) magnification. Qualitative and quantitative analyses show diminished MMP13 and CatK expression in the OA tibial plateau, with a significant reduction in the percentage of osteocytes stained positively for MMP13 (b, control n = 4, OA n = 5) and CatK (d, control n = 4, OA n = 5) in both regions. (e) No differences in negative control staining were observed. (f–

g) Furthermore, Pearson's product–moment correlation indicates that percent of MMP13-positive osteocytes is strongly correlated with lacunocanalicular area (f, $r = 0.79$, $P < 0.0001$) and canalicular length (g, $r = 0.82$, $P < 0.0001$). Graphs show mean ± SEM. *$P < 0.05$ compared with respective regions of control specimens, ⋄$P < 0.05$ between regions by Holm–Sidak post hoc tests.

Targeted ablation of MMP13 expression in osteocytes

An established floxed MMP13 allele (34) was deleted under control of DMP1-Cre (9.6-kb promoter) (35), resulting in mice with a targeted deletion of MMP13 in osteocytes. DMP1-Cre$^{+/-}$;MMP13$^{fl/fl}$ (MMP13$^{ocy-/-}$) animals are born at the same rate and are grossly similar to their DMP1-Cre$^{-/-}$;MMP13$^{fl/fl}$ (wildtype) littermates, with no significant differences in weight or lifespan.

We validated the tissue-specific reduction in MMP13 expression at the transcriptional and translational level. In femoral cortical bone of MMP13$^{ocy-/-}$ animals, immunofluorescence revealed 37% fewer MMP13-positive osteocytes (Figure 5.4a, c), and in subchondral trabecular bone, the number of MMP13-positive osteocytes was reduced by 63% (Figure 5.4b, c, regions of interest shown in Supp. Figure 5.2a, b, channels shown separately in Supp. Figure 5.2c). This result was consistent with the 63% reduction in MMP13 mRNA expression in humeri cleaned of marrow and periosteum (Figure 5.4e).

Given the goal of identifying the role of osteocyte-derived MMP13, and since the 9.6-kb DMP1-Cre promoter can induce off-target recombination in late osteoblasts and some soft tissues (36), we also evaluated possible changes in MMP13 expression in other cell types in the MMP13$^{ocy-/-}$ mouse model. Immunofluorescence revealed neither significant changes in the number of MMP13-positive chondrocytes in articular cartilage (Figure 5.4g) nor qualitative differences in MMP13 expression in growth plate chondrocytes in MMP13$^{ocy-/-}$

mice (Supp. Figure 5.2d). MMP13 expression in periosteal cells (Figure 5.4a), bone marrow (Figure 5.4b, Supp. Figure 5.2c), and skeletal muscle (not shown) was also unchanged between genotypes. Further, the number of DAPI-stained osteocytes in cortical bone is not affected by MMP13 ablation (Figure 5.4f), suggesting that recombination in this model is not affecting the differentiation and embedding of osteocytes. Therefore, the MMP13$^{ocy-/-}$ mouse model is appropriate to observe differences in bone and joint phenotypes arising primarily from changes in osteocyte-derived MMP13.

Trabecular bone volume is increased in mice with systemic ablation of MMP13 and in other models of PLR suppression (13, 19, 34). To determine if deletion of osteocyte-intrinsic MMP13 is sufficient to alter bone mass, we used μCT to analyze trabecular and cortical bone mass and microarchitecture. Relative to wildtype mice, MMP13$^{ocy-/-}$ femurs had a 25% increase in trabecular bone volume fraction due to a 16% increase in trabecular number and a corresponding decrease in trabecular spacing with no change in trabecular thickness (Figure 5.4h). MMP13$^{ocy-/-}$ femurs also show an increase in volumetric bone mineral density and a decrease in SMI reflecting a shift to more plate-like microarchitecture. The mRNA levels or ratio of RANKL and OPG mRNA expression do not account for these differences (data not shown). Cortical bone thickness and total mineral density were normal in MMP13$^{ocy-/-}$ femurs (Figure 5.4i). Therefore osteocyte-intrinsic MMP13 is sufficient to alter trabecular bone volume and mineralization.

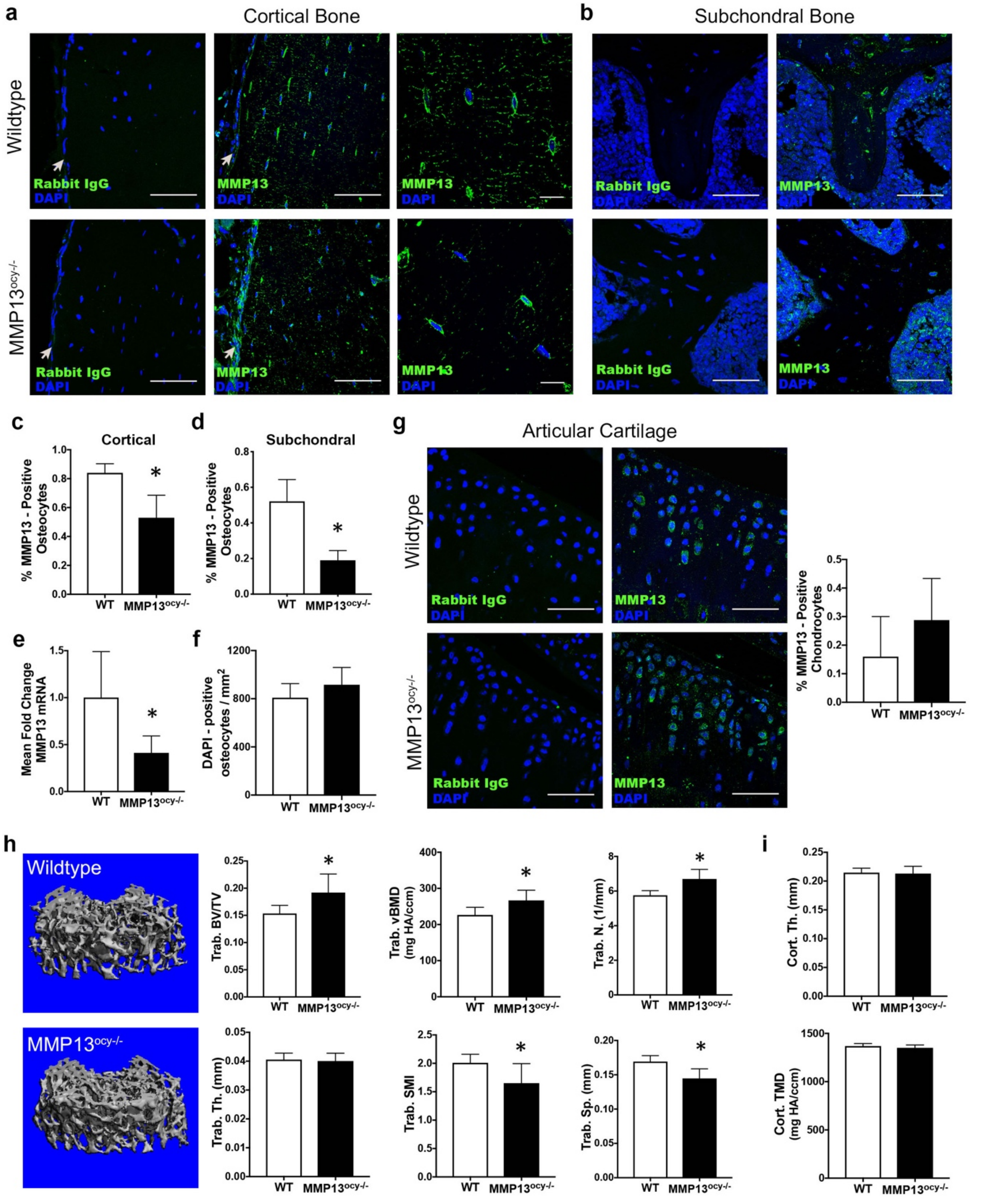

Figure 5.4: Osteocyte-specific reduction in MMP13 expression in the cortical and subchondral bone causes increased trabecular bone mass. (a–d) In cortical bone (a) imaged at low (left and center, arrows indicate periosteal surface, scale bars: 50 μm) and high (right, scale bars: 10 μm) magnification and in subchondral trabecular bone (b, scale bars: 50 μm),

the number of osteocytes stained positive for MMP13 is reduced in MMP13$^{ocy-/-}$ bone compared with wild-type (c, d, n = 6-9). No differences were observed in osteoblasts in the periosteum, in bone marrow, or in negative control images. (e) MMP13 mRNA was also significantly reduced in MMP13$^{ocy-/-}$ bone compared with wild-type (n = 7–9). (f) Osteocyte number was not changed between groups. (g) MMP13 expression in chondrocytes was not significantly different between groups (scale bars: 50 µm, n = 6–8). (h) µCT of distal femoral trabecular bone (n = 11) shows that bone volume fraction and volumetric bone mineral density are increased in MMP13$^{ocy-/-}$ bone due to an increase in the trabecular number and corresponding decrease in trabecular spacing rather than a change in trabecular thickness. Decreased SMI indicates a shift to more plate-like trabecular structures. (i) Cortical bone, however, did not present differences in thickness or mineral density. Graphs show mean ± SD. *$P < 0.05$ between genotypes by unpaired t test.

Suppressed PLR in MMP13$^{ocy-/-}$ bone

To determine the role of osteocyte-intrinsic MMP13 in PLR, we evaluated the osteocyte LCN and collagen alignment, both of which are sensitive to PLR suppression, including in mice with systemic ablation of MMP13 (13). The LCN of femoral cortical bone is visibly disrupted by osteocyte-intrinsic MMP13 deficiency (Figure 5.5a). Canalicular length in MMP13$^{ocy-/-}$ mice is reduced by 20% (Figure 5.5b) with no significant change in lacunar area (Figure 5.5c) or lacunar density (data not shown). This decrease in canalicular length occurs in a coordinated manner across the medial, lateral, anterior and posterior regions of MMP13$^{ocy-/-}$ cortical bone (Figure 5.5b). We consistently observed a small but significant decrease in peak alignment of collagen fibers in MMP13$^{ocy-/-}$ bones compared to wildtype bone in the anterior region (Figure 5.5d, e). In the other regions studied, no differences in collagen linearity were detected despite the change in PLR activity suggested by LCN analysis.

Since changes to collagen, mineral, or LCN organization can affect bone biomechanical behavior (13, 19, 37), we tested mechanical properties of femurs from 2- and 4-month-old wildtype and MMP13$^{ocy-/-}$ mice using 3-point bending. Small but significant decreases in whole-bone structural stiffness and ultimate load were detected in 4-month-old MMP13$^{ocy-/-}$ bones (Table 5.1), consistent with minor deficiencies in both collagen and mineral (38, 39). However, no significant changes were detected in yield properties, postyield displacement, or work-to-fracture, so cortical bone biomechanical outcomes were relatively insensitive to osteocyte-intrinsic MMP13 deficiency in this model. Overall, osteocyte-intrinsic MMP13 is required for PLR since its ablation disrupts the maintenance of canalicular networks and collagen organization and reduces bone mechanical properties.

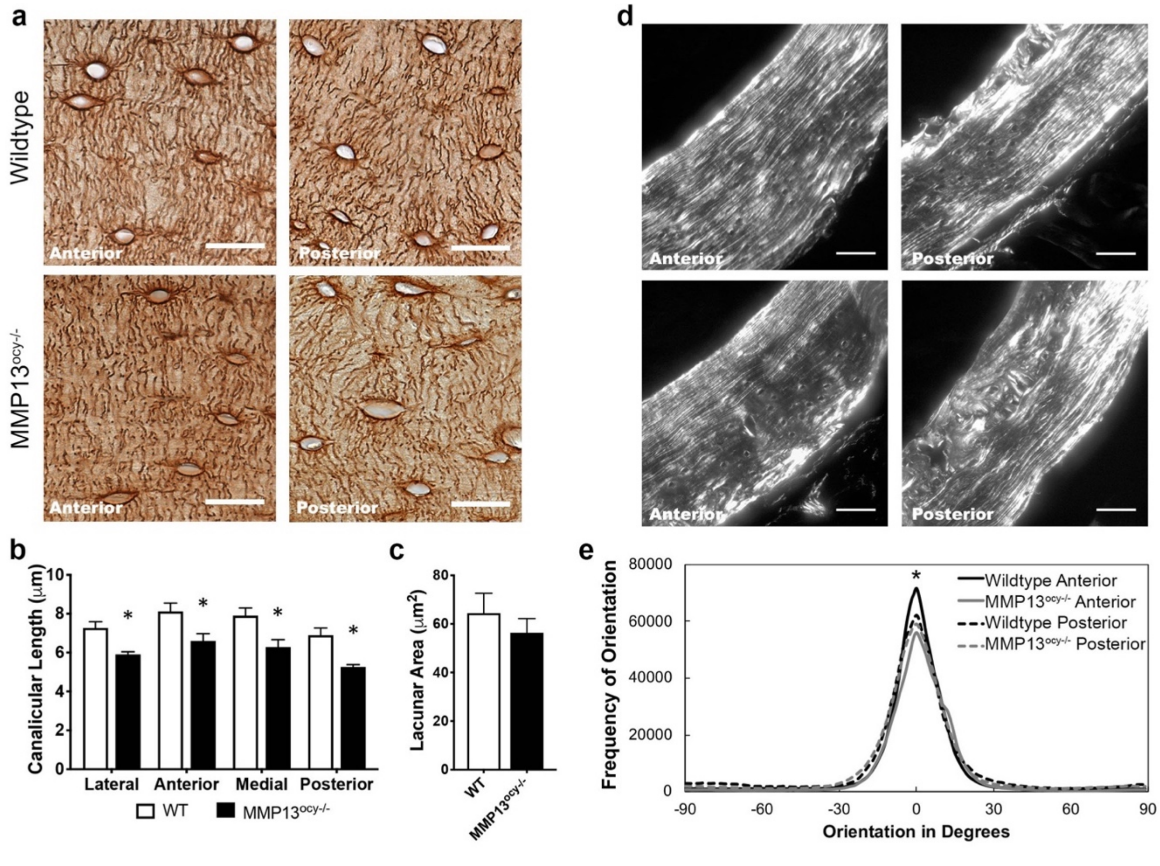

Figure 5.5: MMP13$^{ocy-/-}$ cortical bone displays hallmarks of suppressed perilacunar/canalicular remodeling. (a–c)Canalicular length in wild-type bone is longer than that in MMP13$^{ocy-/-}$ bone in all regions sampled (b, n = 7), while lacunar area is not statistically different (c, n = 7). Graphs show mean ± SEM. (d, e) Collagen fiber organization is reduced in MMP13$^{ocy-/-}$ bone (n = 9) compared with wild-type bone (n = 8) in the anterior quadrant but not in other regions. Lines represent the mean of all specimens in the group. Scale bars are 20 μm in (a) and 50 μm in (d). *$P < 0.05$ between genotypes by unpaired t test.

Table 5.1: Flexural properties of wild-type and MMP13$^{\text{ocy}-/-}$ femurs. Femurs from wild-type and MMP13$^{\text{ocy}-/-}$ mice were broken with either anterior or posterior side in compression. In general, structural and tissue material properties were stronger in posterior (physiological) compression than anterior compression and get stronger with age. Ultimate load tended to be lower in MMP13$^{\text{ocy}-/-}$ bones than wild-type bones, particularly in 4-month-old samples broken in anterior compression. MMP13$^{\text{ocy}-/-}$ bones also had lower stiffness in this test configuration. Values are presented as mean ± SD. $^{*}P < 0.05$ between genotypes, $^{\#}P < 0.065$ between genotypes by unpaired t test.

	Posterior compression, 2 months (n=9)		Posterior compression, 4 months (n=8-9)	
	WT	MMP13$^{\text{ocy-/-}}$	WT	MMP13$^{\text{ocy-/-}}$
Bending Stiffness (N/mm)	79.06 +/- 8.65	77.37 +/- 5.03	105.22 +/- 13.22	104.83 +/- 9.33
Yield Load (N)	11.57 +/- 1.55	10.94 +/- 1.63	13.05 +/- 2.43	13.86 +/- 1.55
Ultimate Load (N)	16.79 +/- 2.21	15.11 +/- 1.24 #	19.02 +/- 2.08	18.24 +/- 1.63
Postyield Displacement (mm)	0.50 +/- 0.22	0.55 +/- 0.26	0.50 +/- 0.37	0.34 +/- 0.14
Work to Fracture (N-mm)	7.98 +/- 1.87	7.86 +/- 3.09	8.24 +/- 3.30	6.55 +/- 1.85
Bending Modulus (GPa)	10.37 +/- 1.52	11.75 +/- 2.70	14.35 +/- 1.08	14.72 +/- 3.07
Yield Stress (MPa)	158.04 +/- 11.51	167.55 +/- 37.78	186.41 +/- 35.28	200.00 +/- 38.15

	Anterior compression, 2 months (n=3-9)		Anterior compression, 4 months (n=8-9)	
	WT	MMP13$^{\text{ocy-/-}}$	WT	MMP13$^{\text{ocy-/-}}$
Bending Stiffness (N/mm)	70.24 +/- 11.08	58.11 +/- 1.55	92.66 +/- 6.90	83.03 +/- 9.27 *
Yield Load (N)	10.18 +/- 1.94	11.11 +/- 3.61	12.28 +/- 0.91	11.76 +/- 1.31
Ultimate Load (N)	13.25 +/- 1.65	13.61 +/- 1.67	17.12 +/- 1.34	15.64 +/- 1.35 *
Postyield Displacement (mm)	0.91 +/- 0.53	0.95 +/- 0.40	0.28 +/- 0.10	0.34 +/- 0.19
Work to Fracture (N-mm)	8.91 +/- 2.32	9.16 +/- 2.40	5.09 +/- 1.50	5.27 +/- 2.01

Increased cartilage degradation in MMP13$^{ocy-/-}$ mice

Though subchondral bone clearly contributes to osteoarthritis, the role of osteocytes in joint disease remains unclear (3, 5–8). Given the strong association of PLR suppression with cartilage degeneration in human OA (Figure 5.1-5.3), we tested the hypothesis that PLR suppression via ablation of osteocyte MMP13 is sufficient to cause cartilage degeneration. Articular cartilage of 4-month-old wildtype and MMP13$^{ocy-/-}$ mouse knees demonstrated clear histopathological differences (Figure 5.6a). Relative to the smooth, proteoglycan-rich articular cartilage in wildtype knees, MMP13$^{ocy-/-}$ cartilage had surface irregularities and depletion of proteoglycans. These characteristic features of degenerating articular cartilage were apparent in basal conditions on the medial and lateral tibial and femoral surfaces. Accordingly, using two established OA grading scales (40, 41), MMP13$^{ocy-/-}$ knees had statistically more cartilage degeneration than wildtype knees (Figure 5.6b, c). Therefore, loss of MMP13 function in the subchondral bone osteocytes is sufficient to disrupt cartilage homeostasis, causing the appearance of osteoarthritic features in otherwise healthy cartilage. This result further suggests that the severe PLR suppression observed in OA human subchondral bone plays a causal role in the progression of joint disease.

To assess the role of PLR suppression in post-traumatic cartilage degeneration, we used an established medial ligamentous injury (MLI) model to induce OA in wildtype and MMP13$^{ocy-/-}$ knees (42). As in non-injured controls, sham-injured MMP13$^{ocy-/-}$ joints showed more cartilage degeneration than their wildtype counterparts (Figure 5.6d). Increases in chondrocyte hypertrophy and articular cartilage lesions, as well as proteoglycan loss, contributed to the more severe OA grade in sham-injured MMP13$^{ocy-/-}$ knees (Figure 5.6e, f). After injury, both genotypes experienced severe loss of articular cartilage and osteophyte formation, but no differences were found between genotypes (Figure 5.6d-f). These data suggest that although MMP13 expression by osteocytes is important for cartilage homeostasis, the severity of joint injury overshadows the osteocytic contribution to healthy joint crosstalk in this model.

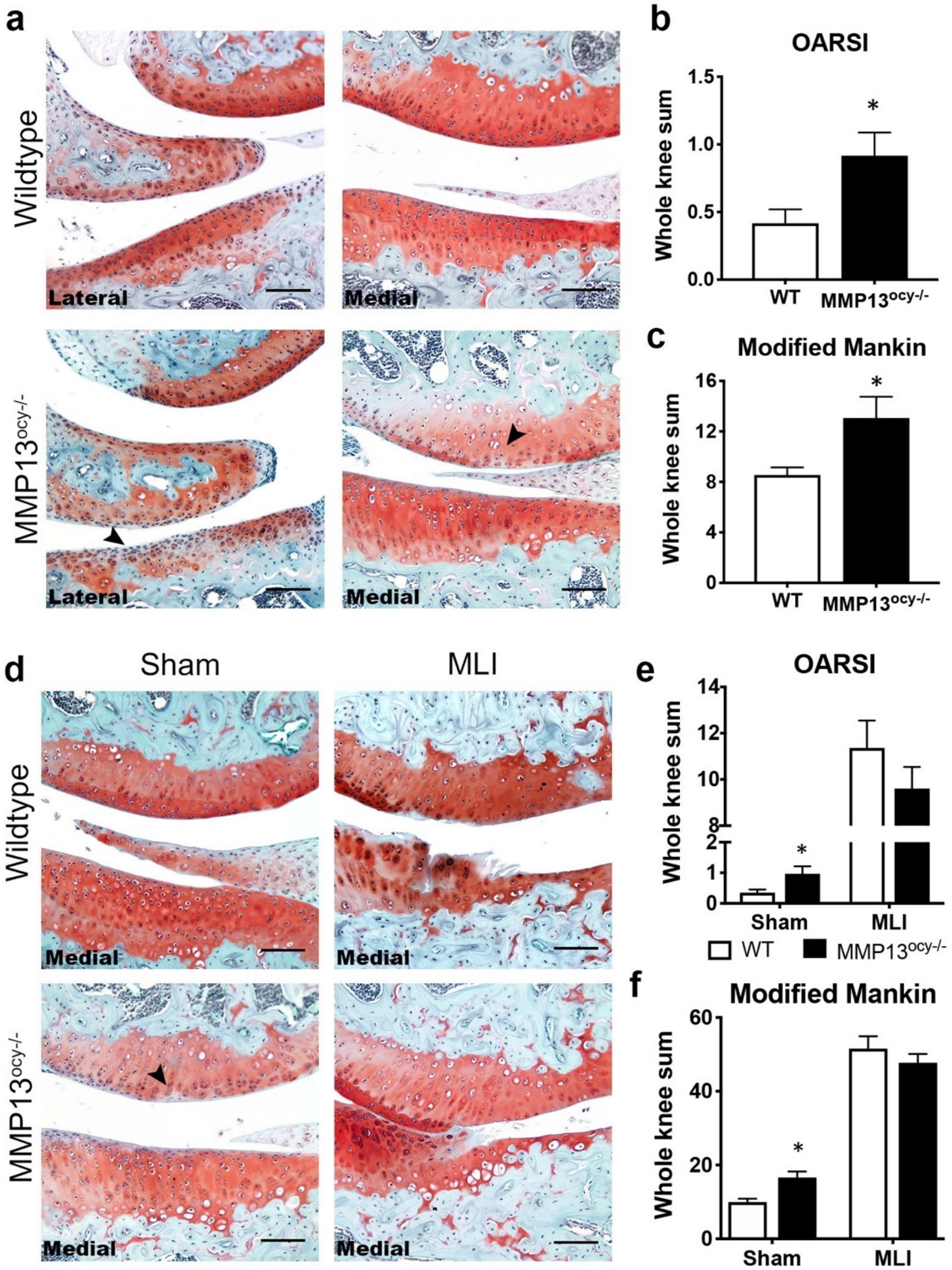

Figure 5.6: Knees of non-injured MMP13$^{ocy-/-}$ mice show more cartilage damage than wild-type mice. (a–c) Safranin-O stained joints of 16-week-old wild-type mice show intact

cartilage, while MMP13$^{ocy-/-}$ mice have areas of cartilage surface irregularity and proteoglycan depletion (a), leading to significantly higher OARSI (b) and modified Mankin (c) scores (n = 6). (d–f) In sham-injured joints, MMP13-dependent proteoglycan loss is still apparent, and meniscal-ligamentous injury (MLI) induces severe cartilage damage in both groups (d). On OARSI (e) and modified Mankin (f) grading scales, sham-injured MMP13$^{ocy-/-}$ mice score significantly higher than wild-type mice (n = 10), but scores are equivalent after MLI (n = 10 for wild-type, n = 11 for MMP13$^{ocy-/-}$). Arrows denote cartilage damage in non-injured joints. Scale bars are 100 μm. Graphs show mean ± SEM. *$P < 0.05$ between genotypes by unpaired t test.

Mechanisms of subchondral osteocyte influence on cartilage

Although a causal role for osteocytes in cartilage degeneration, to our knowledge, has not previously been demonstrated, there are multiple hypothetical mechanisms by which subchondral bone deterioration could exacerbate cartilage degeneration and drive OA (3, 5, 6). These include biological hypotheses such as cell death or vascular changes and mechanical hypotheses such as rod and plate distribution in subchondral bone (8, 43–45). To further understand why MMP13$^{ocy-/-}$ mice are predisposed to cartilage degeneration, we evaluated biological and structural features of tibial cartilage and subchondral bone in healthy and injured joints.

First, we tested the hypothesis that MMP13$^{ocy-/-}$ bone causes increased chondrocyte catabolism and apoptosis by evaluating the expression of cartilage matrix constituents collagen II and aggrecan, of degeneration markers collagen X and MMP13, and of the products of cartilage matrix degradation, the neoepitopes VDIPEN and NITEGE. Relative to the wildtype, MMP13$^{ocy-/-}$ chondrocytes had increased levels of collagen II and a slight decrease in aggrecan (Figure 5.7a). The resulting increase in the collagen II to aggrecan ratio in MMP13$^{ocy-/-}$ cartilage (Figure 5.7b) is a hallmark of early OA (46). MMP13 expression by MMP13$^{ocy-/-}$ chondrocytes was also significantly elevated (Figure 5.7a, c), consistent with the observed cartilage degeneration (Figure 5.6). Significant differences were not observed in collagen X, VDIPEN, or NITEGE expression (not shown), nor were osteocyte or chondrocyte viability altered by osteocyte MMP13 deficiency or injury (Supp. Figure 5.3), though additional timepoints may be required to observe these cellular responses (47, 48).

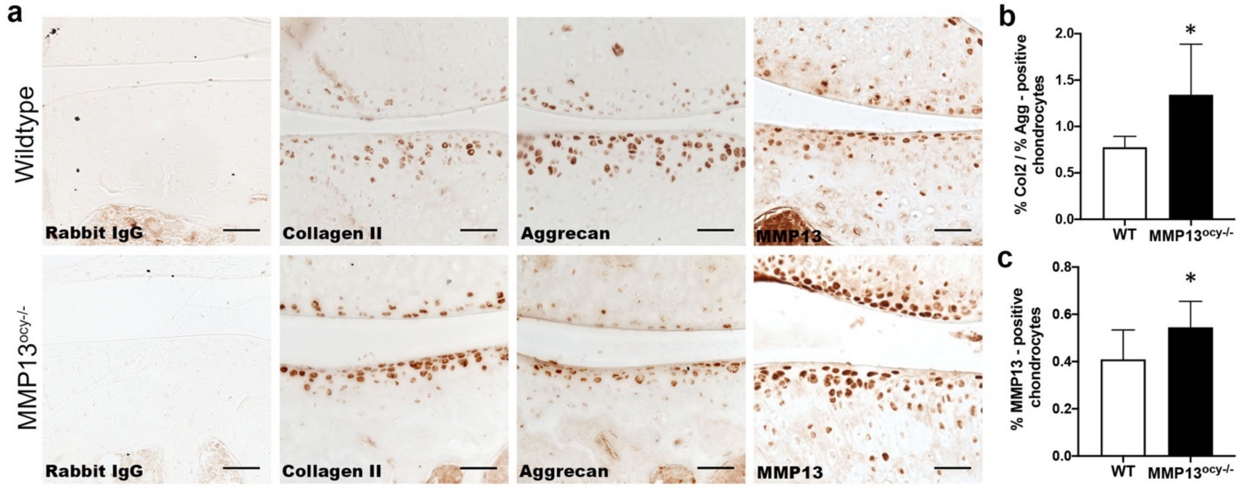

Figure 5.7: Chondrocytes in MMP13$^{ocy-/-}$ mice have altered cartilage matrix synthesis and MMP13 expression. (a) IHC of collagen II, aggrecan, and MMP13 in wild-type and MMP13$^{ocy-/-}$ mice (sham group) show qualitative genotype-dependent changes in cartilage matrix synthesis and degradation, with apparent increases in collagen II and MMP13 and a decrease in aggrecan. (b) The collagen II to aggrecan ratio in MMP13$^{ocy-/-}$ chondrocytes is significantly increased (n = 6). (c) The percentage of MMP13-positive chondrocytes in MMP13$^{ocy-/-}$ knees is significantly increased (n = 10). Scale bars are 50 µm. Graphs show mean ± SD. *$P < 0.05$ between genotypes by unpaired t test.

Second, since human osteoarthritic subchondral bone is characterized by sclerosis, collagen disorganization, and disrupted LCN (Figure 5.1-5.3), we hypothesized that these structural features would be observed in MMP13$^{ocy-/-}$ subchondral bone. As in cortical bone (Figure 5.5a), the canalicular length of osteocytes in MMP13$^{ocy-/-}$ subchondral bone was visibly shorter than in wildtype bone (Figure 5.8a). Canaliculi were 17-20% shorter in MMP13$^{ocy-/-}$ subchondral bone compared to wildtype bone, and injured samples had 17-20% shorter canaliculi than in the corresponding sham-injured groups for each genotype (Figure

5.8b). These findings suggest that the cartilage degradation in mice lacking osteocyte MMP13 could be due to reduced PLR and highlight the sensitivity of the LCN to joint injury. Collagen fiber organization in sham-injured tibial subchondral bone was also disrupted by osteocytic MMP13 deficiency (Figure 5.8c). Joint injury caused a loss of collagen fiber organization compared to wildtype shams (Figure 5.8d), but no differences between genotypes were detected after injury. Similarly, μCT of tibial subchondral bone revealed a MMP13-dependent difference in bone volume fraction between the sham groups, but not between the injured groups (Figure 5.8e, f). Thus, loss of osteocyte MMP13 causes structural changes to subchondral bone that mimic joint injury, possibly via its effects on PLR.

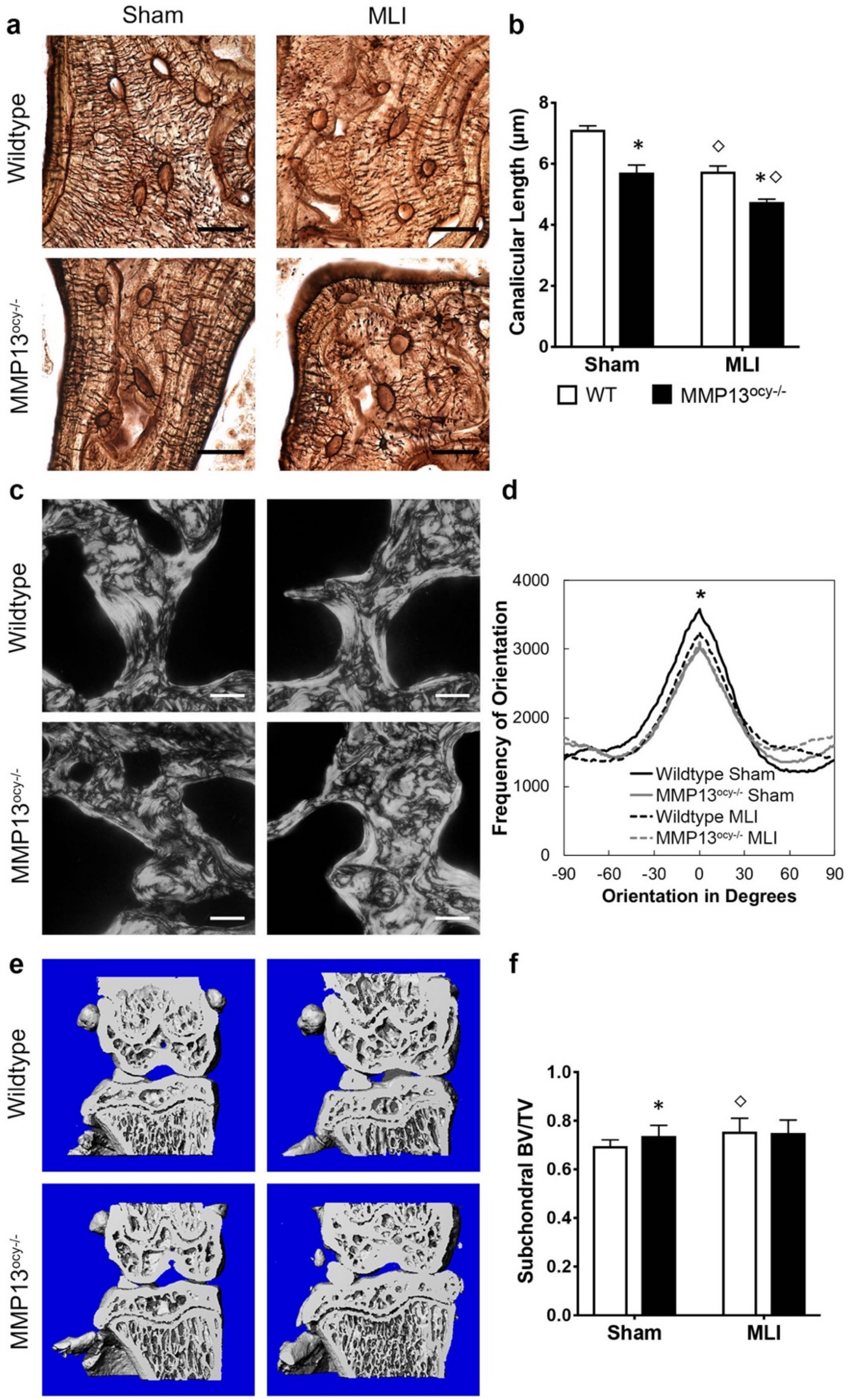

Figure 5.8: Subchondral bone shows MMP13-dependent changes before injury. (a–b) Like in cortical bone, canalicular length in MMP13$^{ocy-/-}$ subchondral tibias is shorter than in wild-type subchondral tibias (a). The difference is statistically significant in injured and non-injured joints (b, n = 6, mean ± SEM). (c, d) Collagen fiber organization is significantly affected

by MMP13 in sham-injured subchondral tibias, but no difference is apparent after injury (n = 6, lines represent the mean of all specimens in the group). (e, f) Similarly, subchondral bone volume fraction is increased in sham-injured MMP13$^{ocy−/−}$ tibias (n = 10) compared with sham-injured wild-type tibias (n = 10), but after injury wild-type (n = 10) and MMP13$^{ocy−/−}$ (n = 11) joints are indistinguishable. Graph shows mean ± SD. Scale bars are 20 μm in (a) and 50 μm in (c). *P < 0.05 between genotypes, ⋄P < 0.05 between treatments by Holm–Sidak post hoc tests.

Finally, we performed RNA-seq on wildtype and MMP13$^{ocy-/-}$ bones to determine which biological pathways in osteocytes were disrupted by MMP13 ablation. We detected 90 upregulated and 454 downregulated differentially expressed genes in MMP13$^{ocy-/-}$ bone, of which MMP13 was one of the most significantly downregulated (Figure 5.9a). With induction or suppression of PLR, we and others have previously observed coordinated and compensatory changes in expression of genes required for matrix resorption, including proteases and genes involved in acid secretion (19, 27). Thus, it was striking to find that the most differentially induced genes in MMP13$^{ocy-/-}$ bone included Ctsk and Acp5, as well as many subunits of vacuolar type ATPases associated with intracellular and extracellular acidification (Figure 5.9a, b). A gene signature score of acidification-related genes showed that they are significantly upregulated in MMP13$^{ocy-/-}$ bone ($p<0.05$). On the other hand, a gene signature score of transcription factors and markers of osteoblast differentiation showed no significant change in MMP13$^{ocy-/-}$ compared to wildtype bone ($p=0.19$), further indicating that the phenotype of the MMP13$^{ocy-/-}$ joint is a result of defective osteocyte function rather than of osteogenic differentiation. Using qPCR we validated that MMP13$^{ocy-/-}$ bone has reduced expression of Mmp2 and increased expression of Ctsk, Atp6v0d2, and Acp5 (Figure 5.9c). No changes were observed in Timp1, Timp2, or Mmp14. The increase in Cathepsin K is due to a change in osteocyte expression rather than osteoclast expression, which was verified by immunohistochemistry (Figure 5.9d). Thus, MMP13 ablation in osteocytes not only disrupts PLR, but also disrupts structural and biological homeostasis of the joint.

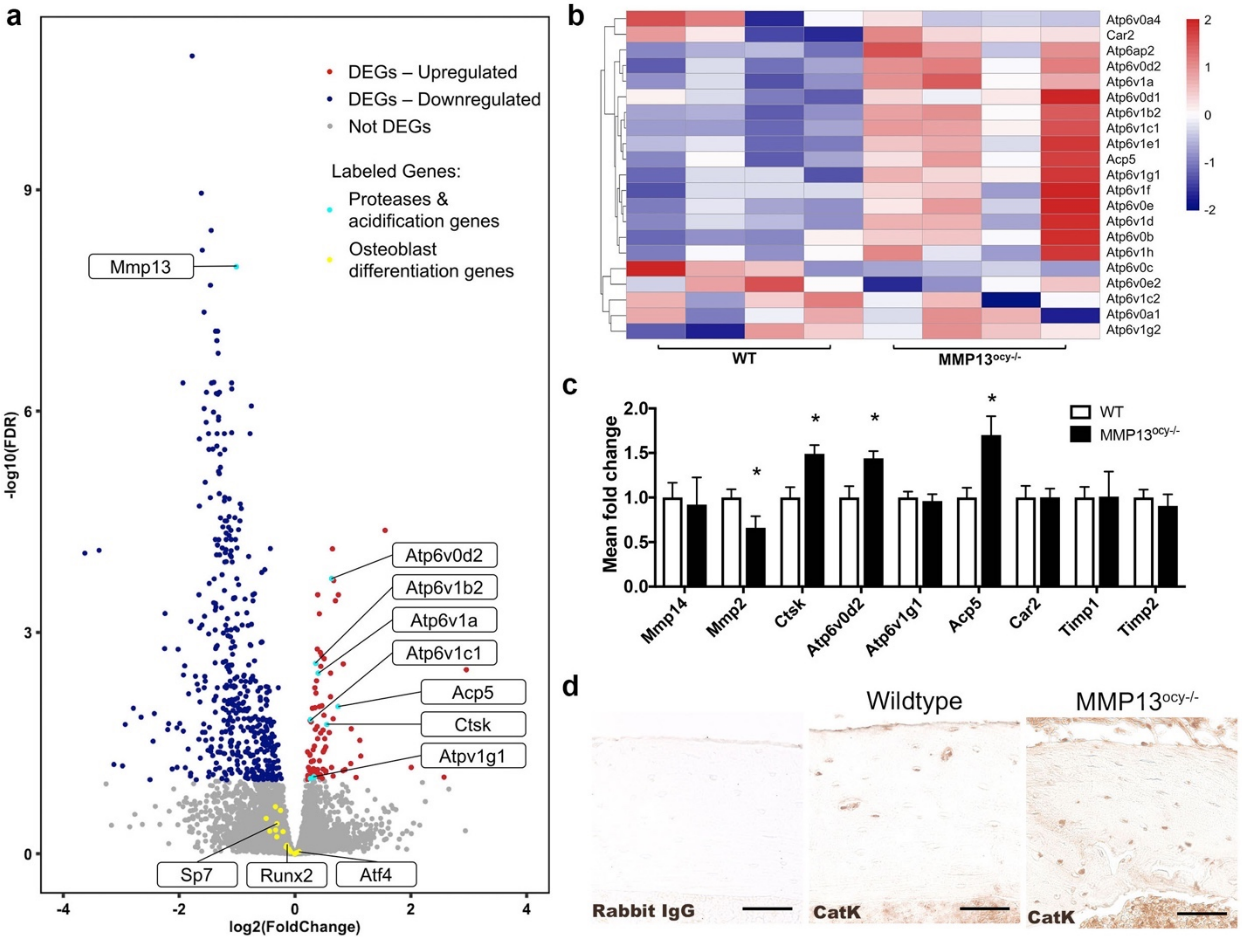

Figure 5.9: Osteocyte deficiency of MMP13 causes dysregulation of genes related to matrix degradation and acidification. (a) RNA-seq of wild-type and MMP13$^{ocy-/-}$ mice (n = 4) identified differentially expressed genes (DEGs) that are significantly repressed (blue) or induced (red) in MMP13$^{ocy-/-}$ bone, with downregulation of MMP13 and upregulation of several proteases and acidification-related genes (highlighted in turquoise). Transcription factors and other genes implicated in osteoblast differentiation (yellow) are among the genes that did not show significant expression differences in MMP13$^{ocy-/-}$ bone (gray). (b) Genes related to acidification were hierarchically clustered in a heatmap by z-score. (c) qPCR of wild-type (n = 8) and MMP13ocy−/− (n = 6) bone validates both co-regulated and compensatory expression of PLR genes (mean ± SD). (d) Immunohistochemistry reveals increased levels of Cathepsin K in osteocytes in MMP13ocy−/− cortical bone (scale bars 50 μm). *P < 0.05 between genotypes by unpaired t test.

Discussion

This study advances our understanding of crosstalk between cartilage and subchondral bone by implicating osteocytes as causal drivers of joint disease in osteoarthritis. In both human and mouse joints, osteoarthritic subchondral bone exhibits several outcomes of PLR suppression, including canalicular and collagen fiber disorganization, hypermineralization, and changes in PLR enzyme expression. Furthermore, osteocyte-intrinsic deficiency in the key PLR enzyme MMP13 is sufficient to suppress PLR and induce premature osteoarthritis, with subchondral sclerosis and cartilage damage in otherwise healthy young mice. This study highlights a new, causal role for osteocytic MMP13 in the regulation of cartilage homeostasis and suggests PLR suppression as a novel mechanism in OA. Therefore, osteocytes emerge as a potential cellular target of new therapeutics to block or reverse OA progression.

Several features of the bone phenotype in MMP13$^{ocy-/-}$ mice resemble those in other models of MMP13 ablation and PLR suppression. Col1-Cre$^{+/-}$;MMP13$^{fl/fl}$ and systemic MMP13$^{-/-}$ mouse models together implicate bone-derived MMP13 expression in trabecular bone remodeling, PLR, and bone quality (13, 30, 34). As in systemic MMP13$^{-/-}$ bone, osteocyte-specific MMP13 ablation increased trabecular bone mass and disrupted canalicular and collagen organization. However, whereas systemic ablation caused decreased postyield deflection and decreased fracture toughness, we observed changes to cortical bone stiffness and ultimate strength only. This was surprising because we previously observed severe defects in bending modulus, yield stress, and toughness in TβRII$^{ocy-/-}$ bone that also has severe PLR suppression (19). The less severe mechanical phenotype is, however, consistent with the more subtle changes to canalicular and collagen organization in MMP13$^{ocy-/-}$ bone. Possible explanations for these differences include the incomplete ablation of MMP13 in MMP13$^{ocy-/-}$ bone, the contribution of non-osteocytic MMP13 to the systemic MMP13$^{-/-}$ phenotype, partial rescue of the MMP13$^{ocy-/-}$ phenotype by diffusion of MMP13 from cells in which it is not ablated, or the coordinated repression of multiple PLR enzymes in TβRII$^{ocy-/-}$, but not in MMP13$^{ocy-/-}$ bone. Whereas Mmp2, Mmp13, Mmp14, Ctsk, and Acp5 were repressed in TβRII$^{ocy-/-}$ bone, MMP13$^{ocy-/-}$ bone showed both co-repression (Mmp2) and an apparent compensatory upregulation (Ctsk, Acp5) of PLR enzymes. Therefore, the partial reduction of PLR enzyme expression in the MMP13$^{ocy-/-}$ model may be insufficient to substantially impact material properties and postyield behavior measured at the whole-bone scale. Overall the MMP13$^{ocy-/-}$ model was sufficient to suppress PLR in cortical and subchondral bone, consistent with the subchondral bone changes seen in end-stage human OA.

This MMP13$^{ocy-/-}$ mouse model presented a unique opportunity to investigate the role of osteocytes in joint homeostasis. Since chondrocyte-derived MMP13 drives OA by cleaving collagen II (31), systemic MMP13 ablation is chondroprotective (32, 33). By preserving chondrocyte expression of MMP13 while reducing its expression in osteocytes, we observed evidence of osteocyte-dependent joint crosstalk, illustrating a novel cellular mechanism by which bone affects the overlying cartilage. Because off-target expression of the 9.6-kb DMP1-Cre promoter has been reported in non-skeletal tissues and in osteoblasts (36), it is impossible to rule out contributions from other cell types to the observed cartilage phenotype. We anticipate that the effect on cartilage of possible non-skeletal MMP13 ablation, which participates in wound healing and cell migration (49), would be most pronounced in sham or MLI animals. However, the cartilage phenotype in non-injured controls and sham-operated animals was consistent, and MLI surgery was not affected by genotype. Our immunostaining and RNA-seq results suggest that loss of MMP13 in osteocytes, rather than in chondrocytes or osteoblasts, is predominantly responsible for the MMP13$^{ocy-/-}$ cartilage phenotype. Indeed, MMP13 was not ablated in MMP13$^{ocy-/-}$ articular cartilage, but rather was elevated, along with other outcomes of cartilage degeneration.

Together the results of the current study address an important gap in understanding OA, namely the identification of mechanisms responsible for the coupled degeneration of cartilage and subchondral bone. We show here that suppression of osteocytic MMP13 causally contributes to the pathogenesis of OA, and several lines of evidence suggest that this is a PLR-dependent mechanism. First, MMP13 plays a key role in the induction and suppression of PLR. In a systemic model of MMP13 ablation and in glucocorticoid treatment, MMP13 expression in osteocytes is reduced and canaliculi are short and disorganized (13, 27). In lactation, MMP13 is strongly upregulated as lacunar area and canalicular size increase (10, 18). In human subchondral bone we show that MMP13 expression is tightly correlated with LCN area and canalicular length (Fig 3), and while the LCN phenotype is more subtle in MMP13$^{ocy-/-}$ subchondral bone than in humans, the relationship remains. Second, several groups have observed changes to osteocyte morphology in OA subchondral bone consistent with suppressed PLR (50–53). Our findings complement and extend beyond these prior reports of altered osteocyte morphology, viability, and gene expression in human OA subchondral bone (50–53) by describing the profound effect of OA on bone extracellular matrix organization, canalicular length, and lacunocanalicular network area. Furthermore, the most severe PLR suppression was evident in the medial compartment with the most cartilage damage. Finally, in mouse cortical bone, glucocorticoids repress MMP13 and other

PLR enzymes, resulting in canalicular degeneration, collagen disorganization, and hypermineralization of subchondral bone (27), all of which mimic the signs of PLR suppression in subchondral bone from another human joint disease, glucocorticoid-induced osteonecrosis (25, 26, 54). Nevertheless, it is possible that osteocytic MMP13 supports joint homeostasis through PLR-independent mechanisms, such as activation of latent growth factors (55–57), or control of osteocyte differentiation or embedding. Although RNA-seq analysis indicates that MMP13$^{ocy-/-}$ bone expresses normal levels of osteogenic differentiation markers, including Runx2, Sp7, and Atf4, an inducible model of MMP13 ablation would be needed to definitively rule out this possibility. The current findings, in which cartilage degeneration results from osteocyte-intrinsic ablation of PLR enzyme MMP13, strengthen the idea that osteocytes play a causal role in joint disease through PLR.

Much remains to be elucidated about the relative role of PLR in age-related joint degeneration and in post-traumatic OA (PTOA). Most animal models of OA involve a joint injury in which both bone and cartilage are affected, and which may additionally initiate inflammatory cascades (40, 42, 58–62), making it difficult to isolate the cell type responsible for cartilage degeneration. In our hands, MLI joint injury reduced canalicular length in both genotypes but did not affect MMP13$^{ocy-/-}$ cartilage more severely. This suggests that reduced subchondral bone MMP13 expression is sufficient to disrupt PLR and cartilage homeostasis, but that joint injury can override preexisting defects (63). In human bone, the more dramatic differences in the lacunocanalicular network may be due to a combination of biochemical and mechanical effects over many years that were not replicated in our injury model. Review of additional timepoints post-injury, or use of a milder injury model, may provide a clearer illustration of how osteocytic MMP13 and PLR contribute to PTOA pathogenesis. Basal phenotypes may be more representative of age-related joint degeneration, in which cartilage degeneration occurs without a known traumatic injury. The predisposition of mice with suppressed PLR to develop cartilage wear is consistent with the idea that subchondral bone sclerosis leads to cartilage breakdown. For example, in a guinea pig model of spontaneous OA, trabecular rod loss and plate thickening precede significant cartilage degradation (8). Likewise, in non-human primates that spontaneously develop OA, subchondral bone thickening appears to precede cartilage fibrillation (64). In humans, longitudinal tracking of bone marrow lesions by MRI reveals the clinical relationship of subchondral changes to OA progression and knee pain (44). Although similar end-stage OA phenotypes can arise from age, injury, or other causes (65), PLR may play a causal role in some of these pathological mechanisms, but not others. The role of PLR in OA in female patients and mice must also be considered separately since PLR, like OA, may have sexually dimorphic effects (66).

Unraveling the circumstances and mechanisms through which a bone-intrinsic defect in MMP13 suppresses PLR and induces OA will require further studies. PLR has the potential to affect subchondral bone vascularity, microarchitecture, and mechanics, cartilage strain distribution, and cell-cell signaling, any of which could impact bone-cartilage crosstalk. The LCN, maintained by PLR, is important for solute transport, and transport between subchondral bone and cartilage is altered in mouse and human OA (21, 67, 68). Changes in subchondral bone volume fraction (43, 69) and geometry (8), similar to those seen in MMP13$^{ocy-/-}$ bone, can precede cartilage pathology, possibly by changing strain distribution in the overlying cartilage. Based on our RNA-seq analyses, biological mechanisms might include autocrine or paracrine effects resulting from excessive acidification by osteocytes. If the critical points at which osteocytes cause and respond to cartilage degradation can be identified, these cells may emerge as a potential target of new therapies to prevent or treat OA. Although many questions remain about the role and regulation of PLR in OA, our data collectively suggests that osteocyte MMP13 dynamically maintains subchondral bone homeostasis and joint crosstalk, and that its disruption can exacerbate joint disease, likely through suppression of PLR.

Materials & Methods

Human donor population and specimen preparation

Five male subjects with clinically diagnosed stage IV osteoarthritis of the tibial plateau, who were scheduled for total knee arthroplasty, were recruited for this study (Supp. Figure 5.1a). Recruitment occurred through referral from orthopedic surgeons at a Department of Veterans Affairs Medical Center. All samples were collected from patients with OA of the femorotibial joint as described in protocols that were reviewed and approved by our Human Subjects Protection Program Institutional Review Board. Informed consent was obtained from each study participant prior to enrollment. Five freshly harvested cadaveric human tibial plateaus from age- and gender-matched donors without history of OA, osteonecrosis, osteoporosis, or fractures were collected through the Willed Body Program at University of California, San Francisco for use as controls. Patients with OA and healthy cadaveric controls had similar BMI. All samples used for immunohistochemistry and mineralization analysis were harvested within four days post-mortem to minimize effects of degradation. Integrity of the tissue and epitopes in histological analyses (Figures 5.1, 5.3, and Supp. Figure 5.1j-k) suggests that refrigerated storage of cadaveric samples for up to 4 days did not significantly affect the conclusions.

Each tibial plateau was removed *en bloc* (Supp. Figure 5.1c, d), and X-rays were collected to evaluate the severity of subchondral bone deterioration (Supp. Figure 5.1g-i). To facilitate comparison of the subchondral bone between the lateral and medial side of the joint, which was more severely affected by OA in these samples, each specimen was cut into 8-10 mm thick coronal slabs with a band saw (Supp. Figure 5.1e, f). Subchondral bone was compared between the medial and lateral regions of interest on the same osteoarthritic tibial plateau, as well as with comparable regions of cadaveric tibial plateaus. Data was collected from five samples per group for all outcomes unless otherwise specified in figure legends.

Mice

To test the role of osteocytic MMP13 in bone and joint health, we generated mice with osteocyte-specific ablation of MMP13. Homozygous MMP13$^{fl/fl}$ mice on an FVB background have loxP sites flanking exons 3, 4, and 5, which encode the enzyme's active site (34) (Table 2.1). Hemizygous DMP1-Cre$^{+\backslash -}$ mice (9.6-kb promoter) on a C57BL/6 background express Cre predominantly in osteocytes and odontoblasts (35). Mice were bred at UCSF to generate wildtype (DMP1-Cre$^{-/-}$; MMP13$^{fl/fl}$) and MMP13$^{ocy-/-}$ (DMP1-Cre$^{+/-}$; MMP13$^{fl/fl}$) mice with a mixed background. Littermate controls were used throughout. To match the VA population of human patient samples and to exclude the sexually dimorphic effects of both OA and PLR (66, 70), only male mice were utilized for this study. The procedures for animal experiments were approved by the Institutional Animal Care and Use Committee at the University of California, San Francisco. Six to eleven biological replicates were used for each outcome, with exact n given in figure legends.

Histology

Human tibial plateaus were fixed in 10% neutral buffered formalin (NBF) and incubated in 10% di- and tetra-sodium EDTA for 56-60 days until fully decalcified, or in an Ion Exchange Decalcification Unit (American Master Technologies) for 5-6 days, followed by serial ethanol dehydrations and paraffin embedding. Paraffin sections (7 μm thick) in the coronal plane were generated for polarized light microscopy, Safranin-O with Fast Green stain, Ploton silver stain, and immunohistochemistry. To standardize evaluation, a consistent region of subchondral bone was selected for evaluation in the medial and lateral areas of each specimen (Figure 5.1a). For each specimen, values were collected from 5 high-powered field images per region of interest. Within each region, these values were averaged to obtain a mean value for each specimen. Each quantitative average represents an average across all specimens.

Intact mouse knee joints and proximal femurs were fixed in 10% NBF and decalcified for two weeks in EDTA, followed by serial ethanol dehydration and paraffin embedding, as described in Chapter 2.

Safranin-O/ Fast Green stain and OA scoring

Safranin-O with Fast Green was used to visualize the cartilage quality of the tibial plateaus using a protocol adapted from University of Rochester (71). Briefly, sections were deparaffinized, rehydrated, and incubated in Weigert's Iron Hematoxylin for 3 minutes. Stained slides were then washed in water and differentiated in 1% Acid-Alcohol for 15 seconds. Slides were then stained with a 0.02% aqueous Fast Green solution for 5 minutes and differentiated with 1% acetic acid for 30 seconds. Slides were then washed with water and stained in a 1% Safranin-O solution for 10 minutes and subsequently dehydrated, cleared, and mounted.

For human tibial plateaus, standardized OARSI grading (72, 73) was used to assess OA in Safranin-O stained histological sections by two orthopedic surgeons. For murine samples, Safranin-O staining was conducted on sections of the knee in a plane where the ACL and PCL were visible to maintain constant region of interest. Each quadrant of the knee (medial and lateral tibia and femur) was graded by three blinded graders using OARSI (41) and modified Mankin (40) scales. For each sample, the numerical scores of all graders were averaged to obtain a mean score. Mean scores were then averaged within each group.

Analysis of collagen fiber orientation by picrosirius red stain

Polarized light microscopy was performed on picrosirius red-stained sections of femurs and subchondral bone, as described in Chapter 2. Statistical analysis was performed as described below.

Analysis of the lacunocanalicular network by Ploton silver stain

Ploton silver stain was performed on axial sections of femurs and frontal sections of subchondral bone, as described in Chapter 2. For human tibial plateau subchondral bone, quantification of the lacunocanalicular area was performed with ImageJ by thresholding 100x gray-scale images for dark, silver stained lacunae and canaliculi. The resulting area was normalized to total bone area in each image captured. Canalicular length was analyzed with ImageJ by individually measuring canaliculi surrounding osteocytes (average 10 canaliculi per osteocyte).

For murine cortical bone, two images were acquired in each quadrant of an axial section (medial, lateral, anterior and posterior). In murine tibial plateau subchondral bone, four images were captured on the medial and lateral side of the joint. In each of the 8 images, area of all visible lacunae was calculated with a custom, commercially available StrataQuest application (TissueGnostics), yielding approximately 90 measurements per animal. Additionally, 10 canaliculi on 3 osteocytes per image (24 osteocytes per animal) were traced using ImageJ to calculate mean canalicular length. To determine whether we had sampled canalicular length from enough osteocytes, we randomly sampled from within the 24 osteocyte averages per animal and found that group averages consistently stabilize once 15 osteocytes per animal are included in the analysis.

Analysis of PLR enzyme expression

Sections of medial and lateral human tibial plateau were deparaffinized and hydrated prior to incubation in Innovex Uni-Trieve low temperature retrieval solution (NB325) in a 40°C water bath for 24 hours. Endogenous peroxidase activity was quenched and the Innovex Universal Animal Immunohistochemistry Kit (329ANK) utilized for subsequent steps as detailed in Chapter 2.

Protein expression in murine cortical bone, subchondral bone, and cartilage was detected by immunofluorescence and immunohistochemistry as described in Chapter 2. For immunofluorescent detection of MMP13 in bone, sections were blocked with Background Buster (Innovex) for 10 minutes, then incubated with primary antibody overnight at room temperature. For cartilage, sections were blocked with 10% normal goat serum for one hour, then incubated with primary antibody overnight at 4 °C. Negative controls were performed by substituting rabbit IgG at the same concentration as primary antibody. The percentage of MMP13-expressing osteocytes and chondrocytes was calculated relative to the total number of cells in at least two 40x fields per sample for 6-9 mice per genotype.

Analysis of cell death by TUNEL assay

To detect osteocyte and chondrocyte death, mouse knee sections were deparaffinized and permeabilized in 0.1% sodium citrate with 0.1% Triton X-100 for 8 minutes. For a positive control, two sections were treated with DNase for 10 minutes at room temperature to induce DNA strand breaks. Then all samples were incubated with TUNEL reaction mix for 60 minutes at 37 °C (Roche). After washing, slides were mounted with Prolong Gold antifade reagent with DAPI and imaged on a Leica DMi8 confocal microscope. Total number of labeled osteocytes and chondrocytes per bone or cartilage area was calculated in the medial and lateral compartments of the tibia for six knees per group.

Synchrotron Radiation X-ray Computed Micro-Tomography (SRμT)

To visualize and quantify bone mineralization, 4-mm-wide specimens of cartilage and subchondral bone were imaged by SRμT at beamline 8.3.2 of the Advanced Light Source (ALS) (Lawrence Berkeley National Laboratory, Berkeley) as described (27). Briefly, transmission radiographs were taken over a 180° rotation with a monochromatic energy of 20 keV and an exposure time of 800 ms. Computational reconstruction of 3D images reveals bone microstructure at 1.3 μm/pixel (5X lens, LuAG scintillator). Images were segmented using ImageJ by binarization of the bone volume morphology. 3D visualization and quantification of bone mineral density was performed using Avizo (Visualization Sciences

Group). Data was collected from n=2 control medial, n=2 control lateral, n=4 OA medial, and n=5 OA lateral human tibial plateaus. Statistical analysis was performed only between medial and lateral regions of OA subchondral bone, as described below.

Micro-computed tomography (μCT)

For skeletal phenotyping, femurs were harvested from male mice at 13 weeks old and stored in 70% ethanol until scanning as described in Chapter 2. For subchondral bone analyses, knee joints were harvested from 16-week-old males and stored in saline solution at -20° C. A 4-mm region centered on the joint was scanned. Medial and lateral tibial subchondral bone were delineated 200 μm from the proximal surface of the tibia and extending for 250 μm distally. The medial and lateral femoral condyles were designated 200 μm from the distal end of the femur and extended proximally 200 μm.

RNA-seq and Quantitative RT-PCR analysis

Humeri from wildtype and MMP13$^{ocy-/-}$ mice were cleaned, homogenized in TRIzol, and purified as described in Chapter 2. qPCR was performed with TaqMan primers for Mmp13 and β-actin, and otherwise with SYBR primers (Table 2.3). Expression was quantified by the ΔΔCt method with β-actin as the housekeeping gene (79).

For RNA-seq, samples were sequenced on the Illumina HiSeq 4000 at the UCSF Functional Genomics Core. Single-end 50bp RNA-seq reads were aligned to the Ensembl mouse GRCm38.87 reference genome using STAR 2.5.2b aligner. We obtained 367.4 million total reads and average of 82.6% of these reads aligned uniquely to the mouse genome. The DESeq2 package in R Statistical Computing Environment was used to find differentially expressed genes with false discovery rate of 0.1 (77). To calculate gene signature scores, we generated gene sets of acidification-related genes (Figure 5.9b) and osteoblast differentiation-related genes (Runx2, Sp7, Atf4, Alpl, Col1a1, Col1a2, Dmp1, Sost, Bglap, Bglap2, Spp1, Phex, Mepe, Enpp1, Enpp2) (78), subtracted the mean from each element, and divided by the standard deviation. RNA-seq data have been deposited in the NCBI BioProject: PRJNA549974.

Flexural strength tests

Whole-bone biomechanical properties were measured in femurs isolated from 2-month and 4-month-old wildtype and MMP13$^{ocy-/-}$ mice. Bones were dissected, stored in HBSS, and tested on the same day as collection. One femur per mouse was broken in the direction of primary physiological bending (posterior compression) and the other was broken against the direction of physiological bending (anterior compression). An 8-mm span was chosen because it was approximately 50% of the bone length.

Whole-bone stiffness was calculated from the linear portion of the load-displacement curve and yield was designated as the point where a line representing a 10% loss in stiffness intersected the load-displacement curve (80). Following fracture, bone cross sections were imaged by scanning electron microscopy on a Sigma 500 VP FE-SEM (Zeiss) at an excitation voltage of 15 kV and a partial pressure of 35 Pa. Measurements of cross-sectional diameter and thickness were acquired in ImageJ and used to calculate moment of inertia assuming an elliptical cross section. These geometric parameters were used to convert the load-displacement data to stress-strain data in order to measure tissue modulus, tissue stress and tissue strain with standard beam theory equations (81).

MLI surgery

8-week-old male mice were separated into three groups: control, sham, and meniscal-ligamentous injury (MLI) (42). Under general isofluorane anesthesia, both hind limbs of MLI animals were shaved and sterilized. A bilateral approach was chosen in order to minimize effects of altered biomechanics arising from a single knee injury, as previously described (82, 83). Briefly, medial incisions through the skin and joint capsule were made adjacent to the patella to expose the medial collateral ligament, which was transected. The medial meniscus was then removed. Sham-injured animals received bilateral incisions without MCL transection or meniscus dissection. Skin incisions were closed with sutures and animals received an injection of long-acting buprenorphine analgesic. Control animals did not receive anesthesia or analgesics. All animals were allowed unrestricted activity, food, and water. At 16 weeks of age, animals were euthanized and hind limbs collected for histological and radiographic analyses.

Statistics

Comparisons between two groups were tested with unpaired two-tailed Student's t-test. Comparisons between disease state and region in human specimens or between genotype and injury in mice were tested with two-way ANOVA followed by Holm-Sidak post-hoc tests. Analyses were performed in GraphPad Prism 8 (GraphPad Software, Inc.). The Clinical and Translational Science Institute Statistical Consulting Service at UCSF evaluated significant differences in the distributions of human collagen organization and mineral density (SRμT) among each group using a mixed model with random intercepts. A linear model was used for the fixed effects, and the outcome was logarithmically transformed. In all figures, p-values less than 0.05 were considered statistically significant and are reported as such. As appropriate for each outcome, the mean is shown +/- SD or SEM, as specified in figure legends.

a

Patient number	Age (years)	Sex	BMI (kg/m^2)	Knee	PTOA Region	OARSI Score
1	65	M	37.5	Left	Medial	5
2	67	M	23.5	Left	Medial	5
3	54	M	31.4	Left	Medial	5
4	74	M	28.2	Right	Medial	4
5	68	M	32.2	Right	Medial	4
Control number	**Age (years)**	**Sex**	**BMI (kg/m^2)**	**Knee**	**PTOA Region**	**OARSI Score**
1	59	M	24.5	Left	None	2
2	79	M	35.7	Left	None	2
3	79	M	35.7	Right	None	2
4	64	M	19.6	Left	None	1
5	64	M	19.6	Right	None	1

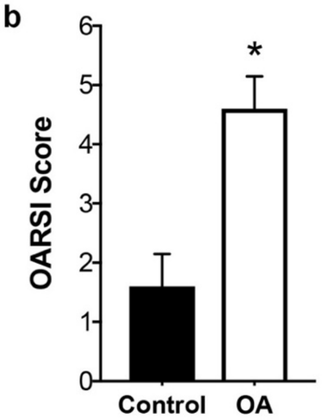

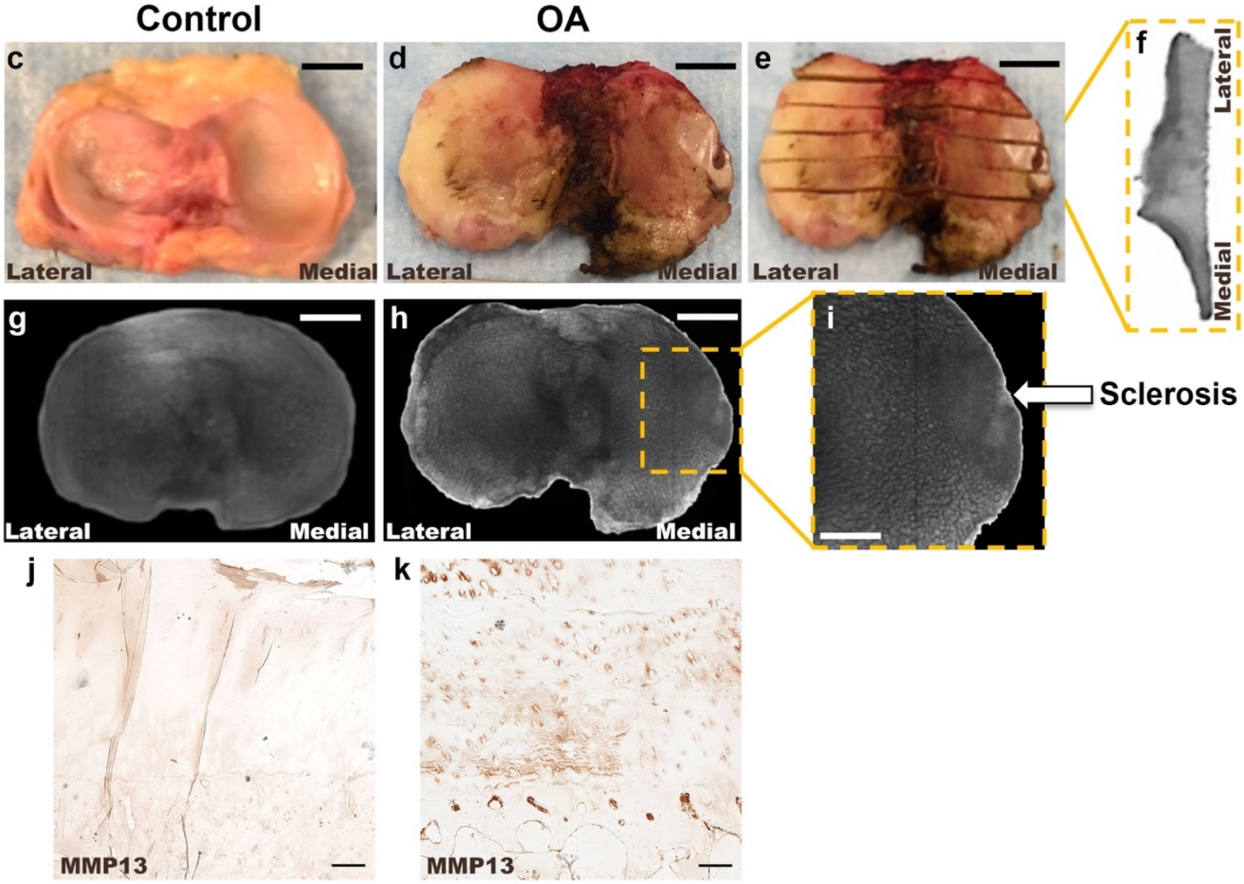

Supplemental Figure 5.1: Osteoarthritic human tibial plateaus have cartilage degradation and subchondral bone sclerosis compared to healthy controls. (a-i) Human tibial plateau specimens from patients with osteoarthritis (OA) undergoing total knee replacement surgery were compared to control cadaveric human tibial plateaus from donors with no history of OA, osteonecrosis, osteoporosis, or fractures. Donations were controlled for age, sex, and body mass index (BMI) (a). OARSI scores (b) were consistent with gross (c, d) and radiographic (g, h) evidence of OA in surgical specimens. Gross cartilage degradation and sclerosis predominated in the medial compartment of OA specimens (i). For further histological analysis, specimens were cut into six 8-10 mm thick coronal slabs (e, f). (j-k)

While control specimens (j) could not be fixed as quickly as OA specimens (k), immunohistochemical analysis of MMP13 suggests that this delay caused neither increased protease expression nor significant epitope degradation, since MMP13 expression in control samples is qualitatively lower in chondrocytes, but higher in subchondral osteocytes (Figure 3a-b) compared to in OA specimens. Scale bars are 2 cm in c-h, 1 cm in i, and 200 μm in j-k. Graph shows mean ± SD. *$p<0.05$ between groups by unpaired t-test.

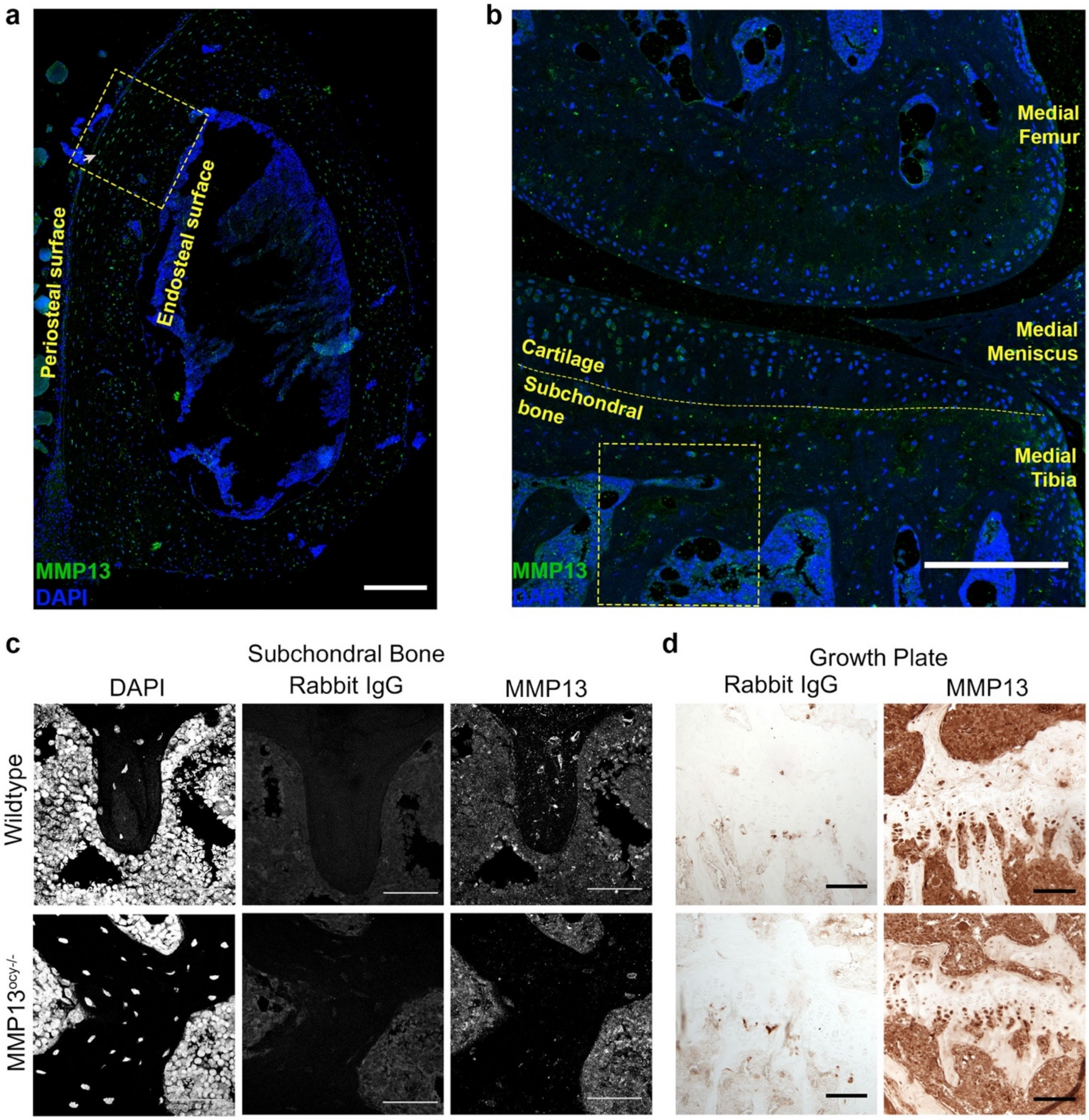

Supplemental Figure 5.2: Data supporting phenotyping of MMP13$^{ocy-/-}$ mice. (a) The yellow box on the axial section of murine femur demonstrates a representative region of interest for cortical bone images in Figure 4a (arrow indicates periosteal surface). (b) The medial femur, tibia, and meniscus are labelled in a frontal section of the murine knee. The yellow box demonstrates a representative region of interest for subchondral bone images in Figure 5.4b. Scale bars 200 μm. (c) Both immunofluorescence and immunohistochemistry were used to evaluate the efficiency and specificity of MMP13 ablation in osteocytes of MMP13$^{ocy-/-}$ mice. To better visualize this difference, DAPI staining is shown separately from MMP13 and negative control immunofluorescence corresponding with Figure 4b. Scale bars 50 μm. (d) MMP13 expression in growth plate chondrocytes is not significantly different between genotypes. Scale bars 100 μm.

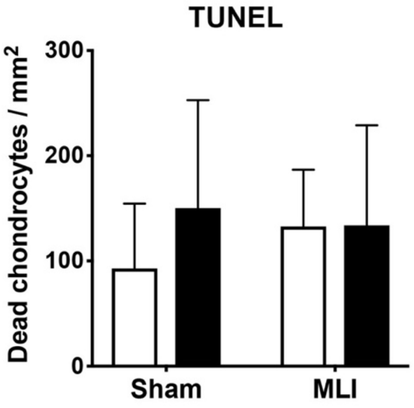

Supplemental Figure 5.3: No difference was detected in TUNEL-positive chondrocytes due to genotype or treatment (n=6).

References

1. Murray CJL, et al. (2012) Disability-adjusted life years (DALYs) for 291 diseases and injuries in 21 regions, 1990-2010: a systematic analysis for the Global Burden of Disease Study 2010. *Lancet (London, England)* 380(9859):2197–2223.
2. Cisternas MG, et al. (2016) Alternative Methods for Defining Osteoarthritis and the Impact on Estimating Prevalence in a US Population-Based Survey. *Arthritis Care Res (Hoboken)* 68(5):574–580.
3. Goldring SR, Goldring MB (2016) Changes in the osteochondral unit during osteoarthritis: Structure, function and cartilage bone crosstalk. *Nat Rev Rheumatol* 12(11):632–644.
4. Chen D, et al. (2017) Osteoarthritis: Toward a comprehensive understanding of pathological mechanism. *Bone Res*. doi:10.1038/boneres.2016.44.
5. Findlay DM, Kuliwaba JS (2016) Bone-cartilage crosstalk: a conversation for understanding osteoarthritis. *Bone Res* 4:16028.
6. Burr DB, Gallant MA (2012) Bone remodelling in osteoarthritis. *Nat Rev Rheumatol* 8(11):665–673.
7. Zhen GH, et al. (2013) Inhibition of TGF-beta signaling in mesenchymal stem cells of subchondral bone attenuates osteoarthritis. *Nat Med*. doi:Doi 10.1038/Nm.3143.
8. Chen Y, et al. (2018) Subchondral Trabecular Rod Loss and Plate Thickening in the Development of Osteoarthritis. *J Bone Miner Res* 33(2):316–327.
9. Bonewald LF (2011) The amazing osteocyte. *J Bone Miner Res* 26(2):229–38.
10. Qing H, et al. (2012) Demonstration of osteocytic perilacunar/canalicular remodeling in mice during lactation. *J Bone Miner Res* 27(5):1018–1029.

11. Bélanger LF (1969) Osteocytic osteolysis. *Calcif Tissue Res* 4(1):1–12.

12. Teti A, Zallone A (2009) Do osteocytes contribute to bone mineral homeostasis? Osteocytic osteolysis revisited. *Bone* 44(1):11–16.

13. Tang SY, Herber R-P, Ho SP, Alliston T (2012) Matrix Metalloproteinase-13 is Required for Osteocytic Perilacunar Remodeling and Maintains Bone Fracture Resistance. *J Bone Miner Res* 27(9):1936–1950.

14. Inoue K, et al. (2006) A crucial role for matrix metalloproteinase 2 in osteocytic canalicular formation and bone metabolism. *J Biol Chem* 281(44):33814–33824.

15. Holmbeck K, et al. (2005) The metalloproteinase MT1-MMP is required for normal development and maintenance of osteocyte processes in bone. *J Cell Sci* 118(Pt 1):147–156.

16. Nakano Y, Toyosawa S, Takano Y (2004) Eccentric localization of osteocytes expressing enzymatic activities, protein, and mRNA signals for type 5 tartrate-resistant acid phosphatase (TRAP). *J Histochem Cytochem* 52(11):1475–1482.

17. Kogawa M, et al. (2013) Sclerostin regulates release of bone mineral by osteocytes by induction of carbonic anhydrase 2. *J Bone Miner Res*. doi:10.1002/jbmr.2003.

18. Kaya S, et al. (2017) Lactation-Induced Changes in the Volume of Osteocyte Lacunar-Canalicular Space Alter Mechanical Properties in Cortical Bone Tissue. *J Bone Miner Res* 32(4):688–697.

19. Dole NS, et al. (2017) Osteocyte-Intrinsic TGF-β Signaling Regulates Bone Quality through Perilacunar/Canalicular Remodeling. *Cell Rep* 21(9):2585–2596.

20. Wang L, Ciani C, Doty SB, Fritton SP (2004) Delineating bone's interstitial fluid pathway in vivo. *Bone* 34(3):499–509.

21. Wang L (2018) Solute Transport in the Bone Lacunar-Canalicular System (LCS). *Curr Osteoporos Rep* 16(1):32–41.

22. Krempien B, Friedrich E, Ritz E (1978) Effect of PTH on osteocyte ultrastructure. *Adv Exp Med Biol* 103:437–450.

23. Marie PJ, Glorieux FH (1983) Relation between hypomineralized periosteocytic lesions and bone mineralization in vitamin D-resistant rickets. *Calcif Tissue Int* 35(4–5):443–448.

24. Rolvien T, et al. (2017) Vitamin D regulates osteocyte survival and perilacunar remodeling in human and murine bone. *Bone* 103:78–87.

25. Weinstein RS (2012) Glucocorticoid-Induced Osteoporosis and Osteonecrosis. *Endocrinol Metab Clin North Am* 41(3):595–611.

26. Assouline-Dayan Y, Chang C, Greenspan A, Shoenfeld Y, Gershwin ME (2002) Pathogenesis and natural history of osteonecrosis. *Semin Arthritis Rheum* 32(2):94–124.

27. Fowler TW, et al. (2017) Glucocorticoid suppression of osteocyte perilacunar remodeling is associated with subchondral bone degeneration in osteonecrosis. *Sci Rep* 7:44618.

28. Imhof H, et al. (2000) Subchondral bone and cartilage disease: A rediscovered functional unit. *Invest Radiol* 35(10):581–588.

29. Kawcak CE, McIlwraith CW, Norrdin RW, Park RD, James SP (2010) The role of subchondral bone in joint disease: a review. *Equine Vet J* 33(2):120–126.

30. Jauregui EJ, et al. (2016) Parallel mechanisms suppress cochlear bone remodeling to protect hearing. *Bone* 89:7–15.

31. Neuhold LA, et al. (2001) Postnatal expression in hyaline cartilage of constitutively active human collagenase-3 (MMP-13) induces osteoarthritis in mice. *J Clin Invest* 107(1):35–44.

32. Wang M, et al. (2013) MMP13 is a critical target gene during the progression of osteoarthritis. *Arthritis Res Ther* 15(1):R5.

33. Little CB, et al. (2009) Matrix metalloproteinase 13-deficient mice are resistant to osteoarthritic cartilage erosion but not chondrocyte hypertrophy or osteophyte development. *Arthritis Rheum* 60(12):3723–33.

34. Stickens D, et al. (2004) Altered endochondral bone development in matrix metalloproteinase 13-deficient mice. *Development* 131(23):5883–95.

35. Lu Y, et al. (2007) DMP1-targeted Cre expression in odontoblasts and osteocytes. *J Dent Res* 86(4):320–325.

36. Dallas SL, Xie Y, Shiflett LA, Ueki Y (2018) Mouse Cre Models for the Study of Bone Diseases. *Curr Osteoporos Rep* 16(4):466–477.

37. Alemi AS, et al. (2018) Glucocorticoids cause mandibular bone fragility and suppress osteocyte perilacunar-canalicular remodeling. *Bone Reports* 9:145–153.

38. Burstein AH, Zika JM, Heiple KG, Klein L (1975) Contribution of collagen and mineral to the elastic-plastic properties of bone. *J Bone Joint Surg Am* 57(7):956–61.

39. Wang X, Bank RA, TeKoppele JM, Agrawal CM (2001) The role of collagen in determining bone mechanical properties. *J Orthop Res* 19(6):1021–1026.

40. Furman BD, et al. (2007) Joint degeneration following closed intraarticular fracture in the mouse knee: a model of posttraumatic arthritis. *J Orthop Res* 25(5):578–592.

41. Glasson SS, Chambers MG, Van Den Berg WB, Little CB (2010) The OARSI histopathology initiative – recommendations for histological assessments of osteoarthritis in the mouse. *Osteoarthr Cartil* 18:S17–S23.

42. Kamekura S, et al. (2005) Osteoarthritis development in novel experimental mouse models induced by knee joint instability. *Osteoarthr Cartil* 13(7):632–641.

43. Fang H, et al. (2018) Early Changes of Articular Cartilage and Subchondral Bone in The DMM Mouse Model of Osteoarthritis. *Sci Rep* 8(1):2855.

44. Alliston T, Hernandez CJ, Findlay DM, Felson DT, Kennedy OD (2018) Bone marrow lesions in osteoarthritis: What lies beneath. *J Orthop Res* 36(7):1818–1825.

45. Lin C, et al. (2019) Activation of mTORC1 in subchondral bone preosteoblasts promotes osteoarthritis by stimulating bone sclerosis and secretion of CXCL12. *Bone Res* 7(1):5.

46. Maldonado M, Nam J (2013) The role of changes in extracellular matrix of cartilage in the presence of inflammation on the pathology of osteoarthritis. *Biomed Res Int* 2013:284873.

47. Anderson DD, et al. (2011) Post-traumatic osteoarthritis: improved understanding and opportunities for early intervention. *J Orthop Res* 29(6):802–9.

48. Sato T, et al. (2006) Comparative analysis of gene expression profiles in intact and damaged regions of human osteoarthritic cartilage. *Arthritis Rheum* 54(3):808–817.

49. Hartenstein B, et al. (2006) Epidermal development and wound healing in matrix metalloproteinase 13-deficient mice. *J Invest Dermatol* 126(2):486–496.

50. Jaiprakash A, et al. (2012) Phenotypic characterization of osteoarthritic osteocytes from the sclerotic zones: A possible pathological role in subchondral bone sclerosis. *Int J Biol Sci* 8(3):406–417.

51. van Hove RP, et al. (2009) Osteocyte morphology in human tibiae of different bone pathologies with different bone mineral density - Is there a role for mechanosensing? *Bone* 45(2):321–329.

52. Wong SYP, et al. (1987) The pathogenesis of osteoarthritis of the hip: evidence for primary osteocyte death. *Clin Orthop Relat Res*.

53. Hopwood B, Tsykin A, Findlay DM, Fazzalari NL (2007) Microarray gene expression profiling of osteoarthritic bone suggests altered bone remodelling, WNT and transforming growth factor-β/bone morphogenic protein signalling. *Arthritis Res Ther* 9(5):R100.

54. Jia J, et al. (2011) Glucocorticoid dose determines osteocyte cell fate. *FASEB J* 25(10):3366–3376.

55. Oursler MJ (1994) Osteoclast synthesis and secretion and activation of latent transforming growth factor β. *J Bone Miner Res* 9(4):443–452.

56. Lyons RM, Keski-Oja J, Moses HL (1988) Proteolytic activation of latent transforming growth factor-beta from fibroblast-conditioned medium. *J Cell Biol* 106(5):1659–1665.

57. Delgado-Calle J, et al. (2018) MMP14 is a novel target of PTH signaling in osteocytes that controls resorption by regulating soluble RANKL production. *FASEB J Off Publ Fed Am Soc Exp Biol* 32(5):2878–2890.

58. Ko FC, et al. (2013) In vivo cyclic compression causes cartilage degeneration and subchondral bone changes in mouse tibiae. *Arthritis Rheum* 65(6):1569–78.

59. Rai MF, et al. (2017) Post-Traumatic Osteoarthritis in Mice Following Mechanical Injury to the Synovial Joint. *Sci Rep* 7:45223.

60. Adebayo OO, et al. (2017) Role of subchondral bone properties and changes in development of load-induced osteoarthritis in mice. *Osteoarthr Cartil* 25(12):2108–2118.

61. Christiansen BA, et al. (2012) Musculoskeletal changes following non-invasive knee injury using a novel mouse model of post-traumatic osteoarthritis. *Osteoarthr Cartil* 20(7):773–782.

62. Glasson SS, Blanchet TJ, Morris EA (2007) The surgical destabilization of the medial meniscus (DMM) model of osteoarthritis in the 129/SvEv mouse. *Osteoarthr Cartil* 15(9):1061–9.

63. Felson DT (2013) Osteoarthritis as a disease of mechanics. *Osteoarthr Cartil* 21(1):10–15.

64. Carlson CS, et al. (1994) Osteoarthritis in cynomolgus macaques: A primate model of naturally occurring disease. *J Orthop Res* 12(3):331–339.

65. Choi R, Smith M, Clarke E, Little C (2018) Cellular, matrix, and mechano-biological differences in load-bearing versus positional tendons throughout development and aging: a narrative review. *Connect Tissue Res* 59(5):483–494.

66. Ma H-L, et al. (2007) Osteoarthritis severity is sex dependent in a surgical mouse model. *Osteoarthr Cartil* 15(6):695–700.

67. Pan J, et al. (2012) Elevated cross-talk between subchondral bone and cartilage in osteoarthritic joints. *Bone* 51(2):212–217.

68. Hwang J, et al. (2008) Increased hydraulic conductance of human articular cartilage and subchondral bone plate with progression of osteoarthritis. *Arthritis Rheum* 58(12):3831–42.

69. Smith RL, et al. (1992) Rabbit Knee Immobilization: Bone Remodeling Precedes Cartilage Degradation. *J Orthop Res* 10:88–95.

70. Dole NS, Yee CS, Mazur CM, Acevedo C, T A TGF-beta regulation of perilacunar/canalicular remodeling is sexually dimorphic. *bioRxiv* 737395.

71. University of Rochester Center for Musculoskeletal Research (2017) Safranin O/ Fast Green Stain for Cartilage. Available at: https://www.urmc.rochester.edu/musculoskeletal-research/core-services/histology/protocols.aspx [Accessed May 1, 2018].

72. Waldstein W, et al. (2016) OARSI osteoarthritis cartilage histopathology assessment system: A biomechanical evaluation in the human knee. *J Orthop Res* 34(1):135–140.

73. Pritzker KPH, et al. (2006) Osteoarthritis cartilage histopathology: Grading and staging. *Osteoarthr Cartil* 14(1):13–29.

74. Montes GS, Junqueira LC (1991) The use of the Picrosirius-polarization method for the study of the biopathology of collagen. *Mem Inst Oswaldo Cruz* 86(3):1–11.

75. Rezakhaniha R, et al. (2012) Experimental investigation of collagen waviness and orientation in the arterial adventitia using confocal laser scanning microscopy. *Biomech Model Mechanobiol* 11(3–4):461–73.

76. Ploton D, et al. (1986) Improvement in the staining and in the visualization of the argyrophilic proteins of the nucleolar organizer region at the optical level. *Histochem J* 18(1):5–14.

77. Love MI, Huber W, Anders S (2014) Moderated estimation of fold change and dispersion for RNA-seq data with DESeq2. *Genome Biol* 15(12):550.

78. Yoshida CA, et al. (2012) SP7 inhibits osteoblast differentiation at a late stage in mice. *PLoS One* 7(3):e32364.

79. Livak KJ, Schmittgen TD (2001) Analysis of Relative Gene Expression Data Using Real-Time Quantitative PCR and the 2−ΔΔCT Method. *Methods* 25(4):402–408.

80. Jepsen KJ, Silva MJ, Vashishth D, Guo XE, van der Meulen MCH (2015) Establishing biomechanical mechanisms in mouse models: practical guidelines for systematically evaluating phenotypic changes in the diaphyses of long bones. *J Bone Miner Res* 30(6):951–66.

81. Turner CH, Burr DB (1993) Basic biomechanical measurements of bone: A tutorial. *Bone* 14(4):595–608.

82. Hamilton CB, et al. (2015) Weight-bearing asymmetry and vertical activity differences in a rat model of post-traumatic knee osteoarthritis. *Osteoarthr Cartil* 23(7):1178–85.

83. Onur TS, et al. (2014) Joint instability and cartilage compression in a mouse model of posttraumatic osteoarthritis. *J Orthop Res* 32(2):318–323.

Chapter 6

Optimization of murine in vivo tibial loading protocol

Introduction

Bone is exquisitely mechanosensitive, adapting to loads it experiences by depositing or resorbing bone. Common examples include a tennis player's dominant arm gaining bone mass, whereas astronauts in microgravity, or people with spinal cord injuries lose bone mass rapidly (1–3). In many bone diseases, this balance between bone anabolism and applied load is disrupted, such that bone mass is lost and no longer meets the demands of normal physiological loads. The range of molecular, cellular, and tissue-level responses of bone to a wide variety of loading conditions is under investigation to better understand how bone mass and other contributors to bone fragility can be improved.

While rodents do not perfectly replicate human bone anatomy, they are valuable model systems for bone research because of their ease of use and numerous genetic models available for manipulation. In vivo loading models such as forced treadmill running, vertebral compression, tibial four-point bending, ulnar axial loading, and tibial axial loading are used to apply a range of loads intended to mimic physiologic and anabolic conditions. Loaded bones are then compared to either non-exercised animals or non-loaded internal control bones (4).

Murine axial tibial loading is one of the most common model systems for in vivo loading (5–9). Generally, the heel and knee are held between fixtures in line with an actuator and a load cell. Load is applied cyclically to one tibia while the mouse is under anesthesia, and the non-loaded limb is used as a control. It is generally accepted that any systemic effects of hind-limb loading are minimal compared to local effects (10). Within this general protocol, many variables exist, including but not limited to:

-Type of anesthesia administered

-Geometry of leg holders and resulting knee flexion

-Waveform shape (triangle, trapezoid, sine)

-Waveform frequency (11)

-Rest insertion between cycles (6)

-Maximum load (7)

-Strain rate of applied load

-Number of cycles applied per session (7, 8, 12)

-Number of loading sessions before analysis (7, 13)

Many studies have compared these variables to maximize the anabolic response of bone. Dynamic histomorphometry to measure rate of bone mineral deposition, microCT to measure bone size and shape, high resolution scans to measure mineral content and composition, and flexural testing describe the structural and mechanical outcomes of load.

Cellular and molecular mechanisms implicated in new bone formation are commonly measured with RNAseq, qPCR, immunohistochemistry, or mice with reporter constructs for osteogenic signaling pathways. As a result of these studies, loading protocols and their associated outcomes that are reported by multiple labs provide useful positive controls. For example, three to five consecutive days of axial tibial load followed by approximately a week of rest reproducibly induces bone formation. At the molecular level, Ptgs2 gene expression and Wnt signaling are upregulated and sclerostin expression is downregulated 3-24 hours after a single loading session (9, 14–16). Anabolic markers such as osteocalcin, Col1a1, alkaline phosphatase, and Timp1 are also upregulated after a variety of loading protocols (9, 13, 15, 17). The response of bone to load is complex and varies with time post-load, site analyzed, and with age, but these published outcomes provide helpful guidance for troubleshooting our own loading protocol.

The goal of this research, described further in Chapter 8, is to measure changes in bone quality induced by anabolic loads. I began with the murine axial tibial loading protocol established in the Alliston lab by Nguyen et al, which increased cortical bone mass, repressed sclerostin expression in osteocytes, and repressed the transforming growth factor beta (TGFβ) signaling effector pSmad3 on Western blots (18). Beginning with the published methods, I sought to replicate the loading protocol and the positive control outcomes established by Nguyen et al and others. Anticipating quick success, I also measured Mmp13 expression in some experiments as an indicator of perilacunar remodeling activity. This chapter details the optimization process leading to the loading protocol eventually used to evaluate mechanosensitive changes in bone quality.

Methods

Mice

SBE-Luciferase mice express luciferase in response to pSmad2/3 activity. Mice were bred at UCSF, and 8-week-old male mice were used for experiments (Table 2.1).

In vivo loading model

The loading model previously validated in our lab was designed to simulate the forces applied by vigorous jumping (approximately ten times body weight) (18). A BOSE Electroforce ELF3200 desktop load frame was fitted with custom fixtures to cup the mouse heel and knee and provide axial compressive load to the tibia. Before loading, mice are anesthetized with injectable ketamine/xylazine anesthesia (100 mg/kg ketamine and 16 mg/kg xylazine) and lack of response to a toe pinch is confirmed before the right leg is placed into the load frame. The actuator is programmed to displace until it applies -3.5 N (compressive load) to the limb, then to back off to -0.5 N. This cycle is repeated in a sinusoidal pattern 600 times at 1 Hz in load-control mode (Figure 6.1 A), after which the mouse is returned to a warm cage to recover and then ambulate normally until the next loading session or predetermined harvest time. After harvest, the non-loaded tibia serves as an internal control for each animal, as others have determined that the anabolic response to load is not systemic (10).

During optimization and troubleshooting of the in vivo loading protocol, several variations of this protocol were tested, as detailed in the Results. At the conclusion of this process, the variables used to apply load in our in vivo loading model were changed as follows. The final dosage of injectable ketamine/xylazine anesthesia is 100 mg/kg ketamine and 10 mg/kg xylazine. A 50 lb load cell is now used instead of a 10 lb load cell, and a new lower fixture maintains the mouse ankle at approximately 30° of flexion (Figure 6.1 B-C). Due to the decreased sensitivity of the 50 lb load cell, the waveform is now run on displacement control. Once the mouse is anesthetized and positioned, the actuator is manually displaced until the load feedback reads the desired maximum load (usually between -3.5 and -6 Newtons) and then the desired minimum load (-0.5 Newtons). The actuator is then set to cycle between these two positions for 600 cycles at 1 Hz in displacement control mode. The load and displacement data are recorded at 10 Hz in order to calculate the actual applied loads and displacements for each loading session for each mouse.

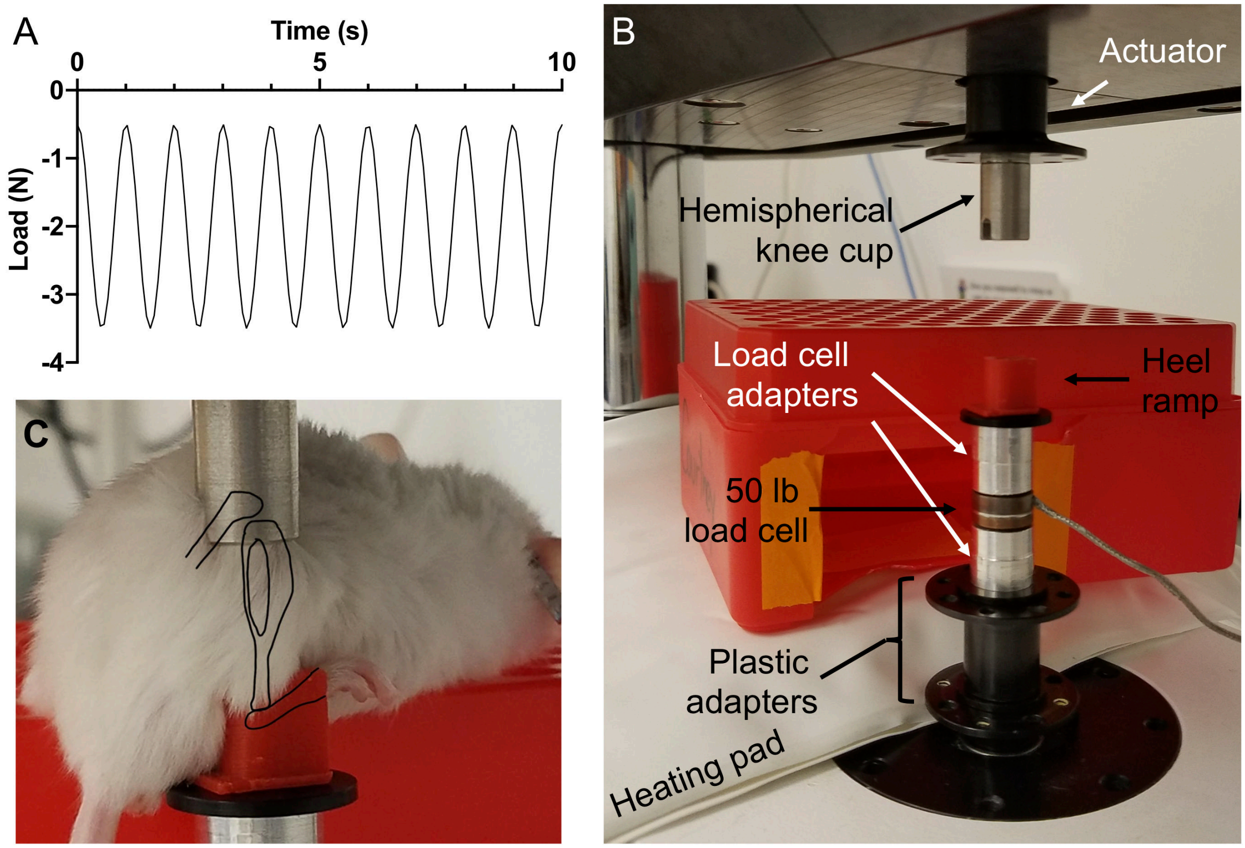

Figure 6.1: Waveform and setup for murine in vivo tibial axial loading. (A) Target waveform for in vivo axial tibial loading. (B) Photo of adapters and fixtures used for final loading setup. (C) Illustration of mouse hindlimb in loading configuration.

MicroCT

Right legs were loaded for five consecutive days, and loaded and non-loaded tibias were collected 3 days later. Bones were dissected, fixed in 10% NBF for 24 hours, then stored in 70% EtOH. MicroCT scans were performed at the University of Oklahoma Health Sciences Center.

Quantitative RT-PCR analysis

Loaded and non-loaded tibias were dissected, epiphyses trimmed, marrow centrifuged out, and periosteum cleaned. For Figure 6.3 and 6.4, foil-wrapped bones were stored in liquid nitrogen until RNA extraction using TRIzol. qPCR was performed with SYBR primers (Table 2.3) and expression quantified by the ΔΔCt method with the housekeeping genes designated in figure legends. For Figures 6.13 – 6.15, the proximal and distal portions of tibias were snap-frozen in liquid nitrogen, homogenized in 1 mL QIAzol, and stored at -80 °C. qPCR experiments with SYBR primers happened in multiple batches, so samples in each batch were combined to generate a standard curve for each gene being assessed. Results were calculated in terms of nanograms transcript relative to nanograms β-actin. Loaded expression was then compared to non-loaded expression of each gene for each mouse.

Protein extraction from bone

Loaded and non-loaded tibias were dissected, epiphyses trimmed, marrow centrifuged out, and periosteum scraped away. Foil-wrapped bones were stored in liquid nitrogen until protein extraction. RIPA buffer (Chapter 2) was prepared fresh on the day of protein harvest.

In the initial protocol, porcelain mortars and pestles are pre-chilled in a bath of liquid nitrogen at least 50% the height of the mortars. Bones are removed from liquid nitrogen storage and pulverized one by one with clean mortars and pestles. The powder lysate is scraped into an Eppendorf tube and resuspended in 80 μL ice cold RIPA. In the final protocol, bones are homogenized in individual tubes with a bead mill homogenizer (Chapter 2).

After bone lysate is in RIPA, samples are incubated on ice for 30 minutes, sonicated, and centrifuged to clarify protein. The initial protocol suffers from loss of product during the transfer out of the mortar, which often made it difficult to detect signal from the distal portion of the tibia. The final protocol suffers from loss of product during the final transfer of liquid protein lysate from a flat-bottomed tube, but it provides more consistent high-yield protein that enables comparison of distal and proximal tibia regions.

Western blotting

Protein from loaded and non-loaded bones was quantified using the Bradford Assay as described in Chapter 2. Equal quantities of protein from each bone were resolved on 8.5% SDS-polyacrylamide gels, as described in Chapter 2, and probed with antibodies for pSmad3 and β-actin (Table 2.2).

Flexural strength tests

To determine whether the range of applied loads was causing bone damage, loaded and non-loaded tibias were collected within one hour of a single loading session with a low (4 - 5.5 N) or high (6.5 – 8 N) peak compressive load. Tibias were gently cleaned of muscle and stored in HBSS-soaked gauze at -20 °C. Bones were brought to room temperature before testing. Tibias were broken in 3-point bending on a 6 mm span with the postero-lateral surface in compression. The distal tibiofibular junction was aligned with one side of the span and the central loading point was just distal to the tibial crest. Whole-bone stiffness was calculated from the linear portion of the load-displacement curve and ultimate load was defined as the maximum bending load sustained.

Strain gaging

To determine the surface strain engendered by compressive loads applied to the tibia, we attached strain gages to the antero-medial surface of the right tibia 50% of the distance between the tibiofibular junctions. Five animals were euthanized and the right tibia exposed. The middle of the antero-medial surface was gently scraped to remove periosteum and then cleaned with 70% ethanol.

Pre-wired strain gages (0.38 mm x 0.50 mm) were purchased from VPG Sensors and connected to a Micro-Measurements system (8000-8-SM) for data acquisition. Strain gages were prepared by brushing with a thin layer of catalyst C on the bonding surface (M-Bond 200 kit). A thin layer of adhesive was applied, and the gages were adhered to the bone surface aligned axially with the tibia and held with finger pressure for at least one minute. After curing, the mouse was positioned in the load frame and its right tibia was loaded in displacement control at increasing amplitudes. Load-displacement data was recorded through WinTest 8 and strain data was collected simultaneously through StrainSmart 8000.

Statistics

Paired t-tests between loaded and non-loaded bones from the same animal are used throughout.

Results & Discussion

Experiments were initially conducted using the lab's existing setup. A mouse's right leg was held vertically between two hemispherical cups that each had a cutout to accommodate a foot or thigh. A 1 Hz sinusoidal waveform was run on load-control with a 10-lb load cell providing feedback. 600 cycles were applied, and the entire length of the tibia was collected for analysis. Five consecutive days of loading to a maximum load of 3.5 N with this method had previously caused a significant increase in cortical thickness (18). In my hands, the load-induced changes in bone mass were more modest than anticipated. Five days of loading with a maximum load of 3.5 N caused small but non-significant increases in cortical bone volume fraction at the tibial midshaft. No further changes were detected when the maximum load was increased to 5 N (Figure 6.2).

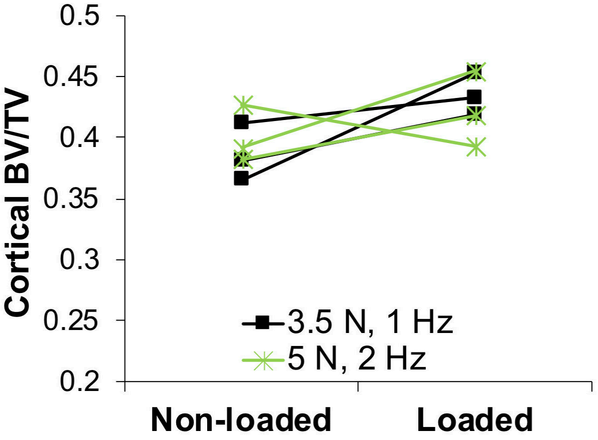

Figure 6.2: MicroCT of the cortical midshaft of loaded and non-loaded mouse tibias. n=6. p=0.09.

Since structural changes may be slower to develop than transcriptional changes following load, qPCR was also performed on whole bones. Mice were again loaded for 5 consecutive days to a maximum of 3.5 N and harvested three days later. Our lab previously found that TGFβ signaling is repressed following load, and the TGFβ-responsive gene

Serpine1 was significantly downregulated here (Figure 6.3). However, we expected other known mechanosensitive genes to be differentially expressed. Sost was not downregulated and anabolic markers Col1a1, OC and AP were not upregulated, suggesting insufficient stimulus or improper timing of the analysis. Attention was instead turned to shorter timepoints for faster troubleshooting.

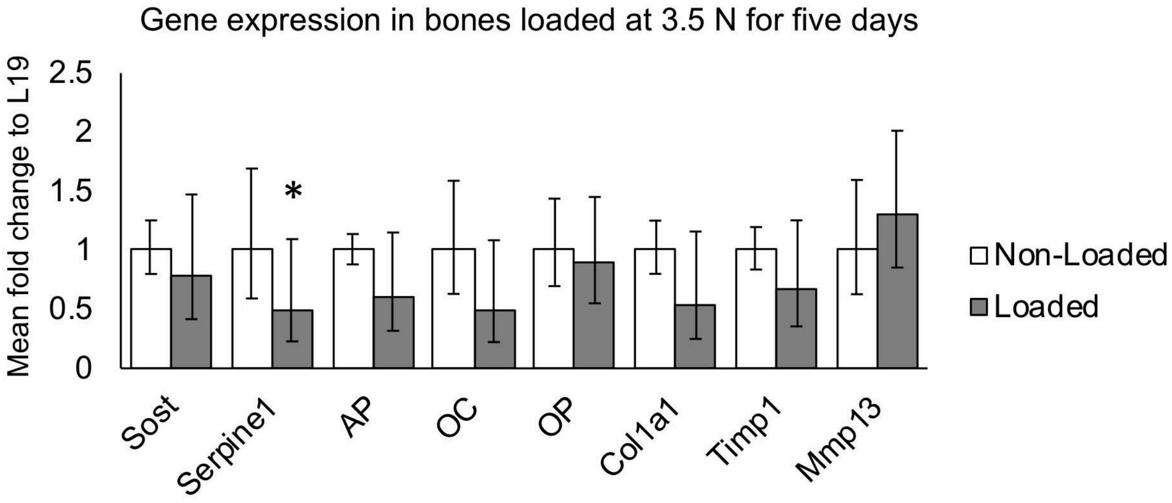

Figure 6.3: Gene expression in whole tibias loaded for five consecutive days. Serpine1 is significantly downregulated by paired t-test. n=4. *p<0.05.

At 30 minutes to 2 hours after a single loading session, we expected to find upregulation of the rapidly mechanoresponsive gene Ptgs2 in addition to possible downregulation of Sost and Serpine1. At 30 minutes post-load, Sost repression was nearly significant (p=0.11), but no other gene expression was as anticipated (Figure 6.4).

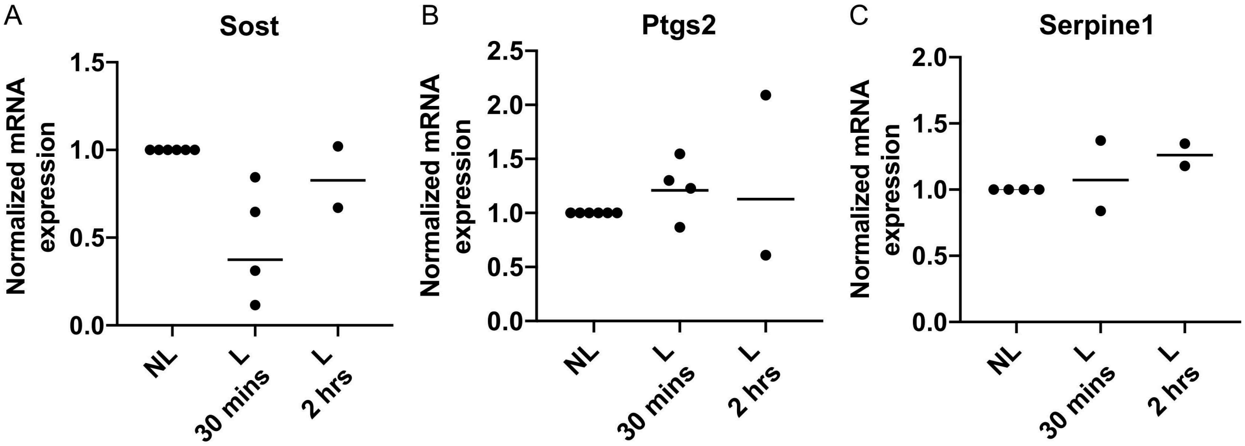

Figure 6.4: Gene expression in whole tibias shortly after one 10-minute loading session. mRNA expression is normalized to 18s and then to the non-loaded internal control bone. Bars show geometric mean. n=2-4 per timepoint.

Previous in vivo tibial loading in our lab characterized post-translational responses to load more than transcriptional outcomes, so I collected protein from loaded and non-loaded bones to determine whether I could replicate load-induced repression of pSmad3. Bones collected 2 hours after a single load showed inconsistent changes to Smad2/3 phosphorylation. Instead of repression, pSmad3 was induced or unchanged (Figure 6.5).

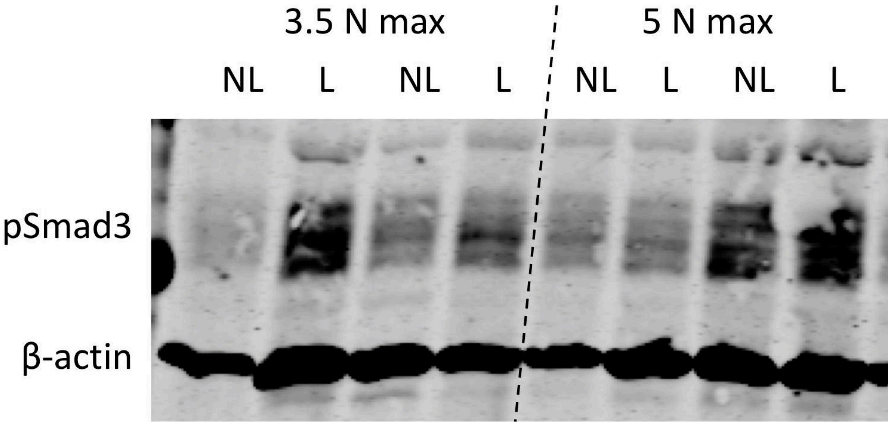

Figure 6.5: pSmad3 expression two hours after a single loading session. The whole length of the tibia was collected after 10 minutes of loading to the indicated magnitude on load-control.

I later learned that the previous experiments showing post-load pSmad3 repression were conducted on only a middle region of the tibia, distal to most of the trabecular bone. This region mainly contains cortical bone, and it was difficult to harvest sufficient protein to visualize on a Western blot using a mortar & pestle. When it was possible, and after applied loads as high as 8 N, no load-induced changes were obvious (Figure 6.6 B). It was much easier to collect protein from the more proximal, cancellous-rich region of the tibia. After maximum loads of 8 N, induction of pSmad3 was apparent in the proximal tibia (Figure 6.6 A). Given the apparent induction of pSmad3 in whole bone (Figure 6.5) and in proximal tissue, I hypothesized that the proximal region of the tibia may be so cellular that it masks the possibly unique load response happening more distally when the entire tibia is homogenized together. Quantification of RNA yield from whole tibias, proximal regions, and distal regions supports the possibility that molecular outcomes from whole tibias are dominated by proximal tissue (Figure 6.6 C). Given the difficulties of harvesting bone lysate from the distal region, bones were still harvested in their entirety until methods could be improved.

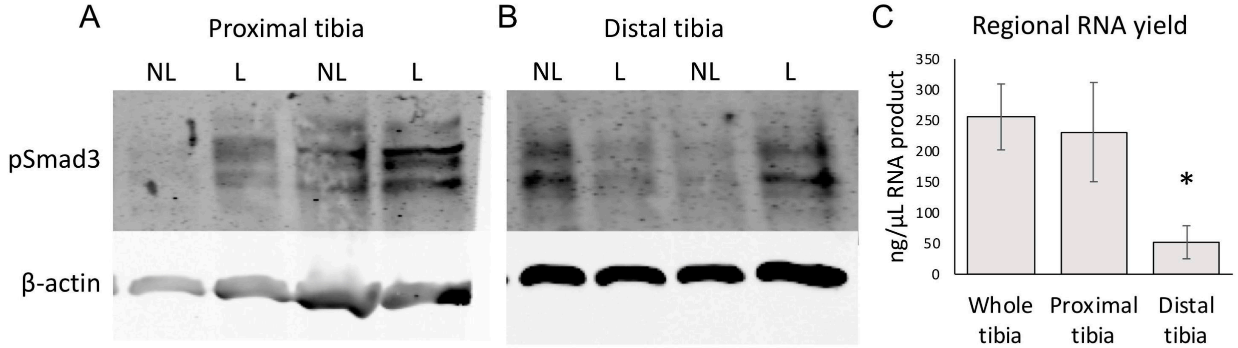

Figure 6.6: Regional differences in pSmad3 expression post-load and in RNA yield. (A-B) pSmad3 expression in proximal and distal tibia two hours after a single loading session to a maximum load of 8 N on load feedback. (C) RNA yield in 35 μL volume from whole tibias compared to tibia regions harvested individually. n=4-6. *p<0.0001.

Since the loading sessions described thus far were all performed in load-control mode, the applied load depends heavily on the accuracy of the load cell. The displacement amplitude for loads cycling between 0.5 N and 3.5 N compression were consistently 0.2 - 0.25 mm. Over the 10 minute loading protocol, the displacement amplitude tended to decrease, and the maximum applied displacement increased, perhaps compromising for shifting of soft tissues (Figure 6.7). A major weakness of this load setup was that the metal foot holder does not provide consistent resistance for the mouse foot. In many cases, the foot slipped completely out of the holder, indicating that load had not been applied perfectly axially.

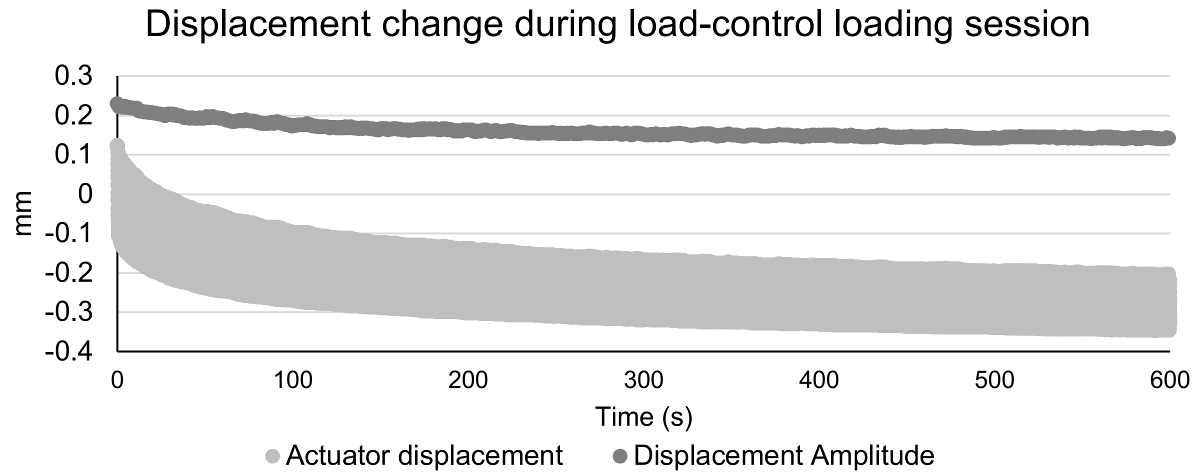

Figure 6.7: Representative load track from the 10 lb load cell run on load control between 0.5 N and 3.5 N compression.

The frequent foot slipping was likely caused by a bent connector on the 10 lb load cell that shifted the foot holder out of axial alignment, so future loading was performed on the intact 50 lb load cell. Preliminary experiments were conducted to determine whether load-controlled waveforms were still appropriate for a load cell with lower sensitivity or if displacement feedback would provide better accuracy. Initial tests with the 50 lb load cell were run on load-control, and results suggested suppression of pSmad3 in lysate from the entire tibia (Figure 6.8). This suggested that with the tibia aligned more vertically, the expected mechanosensitive response could actually be stimulated. However, the load cell seemed insensitive to the differences between 3.5, 5, and 8 Newton maximum loads, as the displacement amplitude selected in the case of these three trials was identical.

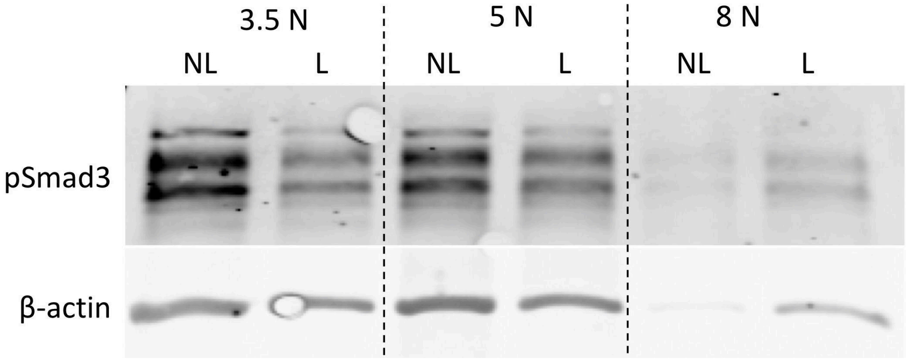

Figure 6.8: pSmad3 expression after loading with the 50 lb load cell on load-control. The whole length of the tibia was collected two hours after 10 minutes of loading to the indicated magnitude.

Across multiple experiments, mechanosensitive repression of pSmad3 was not consistent after loading with the 50 lb load cell on load-control. After learning that previous loading experiments in the lab had in fact used the 50 lb load cell on displacement-control, I switched to this configuration. Displacement control relies less on the real-time computation of feedback from the load cell. In this scenario, the mouse leg is positioned in the foot and knee holders and the actuator is manually displaced to determine positions that will apply the desired maximum and minimum forces. The actuator then cycles between those positions 600 times without gathering input from the loadcell.

Over the course of a 10 minute loading session run on displacement-control, the displacement amplitude remains constant, but the applied load sensed by the load cell decreases over time (Figure 6.9). This again may be due to shifting of soft tissues that provide less resistance to load over time, but it suggests that overshooting the applied load on the first few cycles may be necessary in order to achieve the desired load through the end of the 10 minute protocol. Displacement-control removes the necessity of fast and accurate load-cell readouts for tuning of the waveform in real-time but may introduce additional variation in terms of actual load applied to each subject. The response of pSmad3 to load was not obviously different when applied via load-control or displacement-control (Figure 6.10).

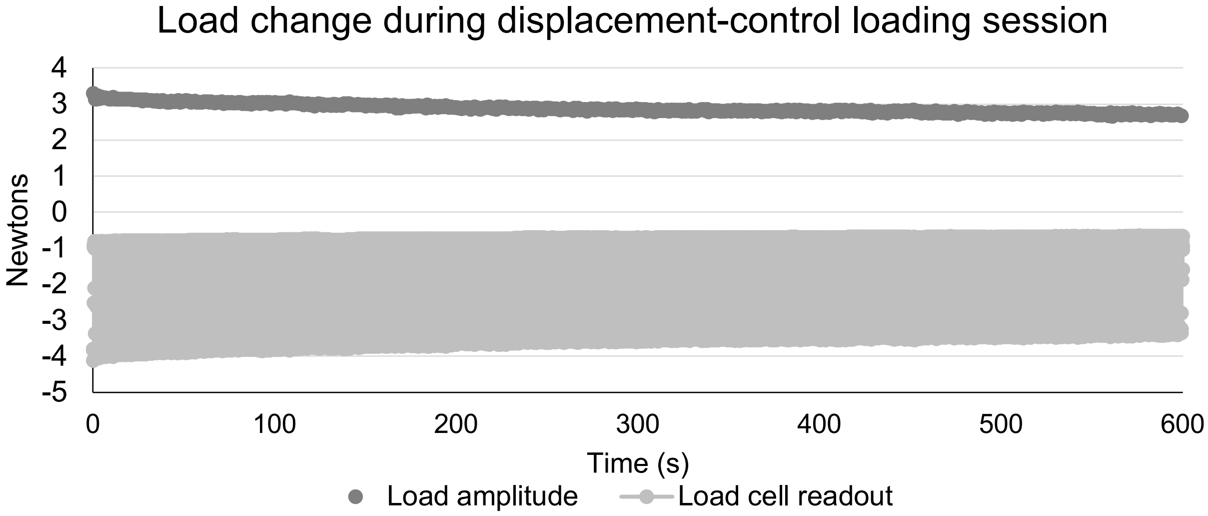

Figure 6.9: Representative load track from 50 lb load cell run on displacement-control for goal loads between 3.5 N and 0.5 N compression.

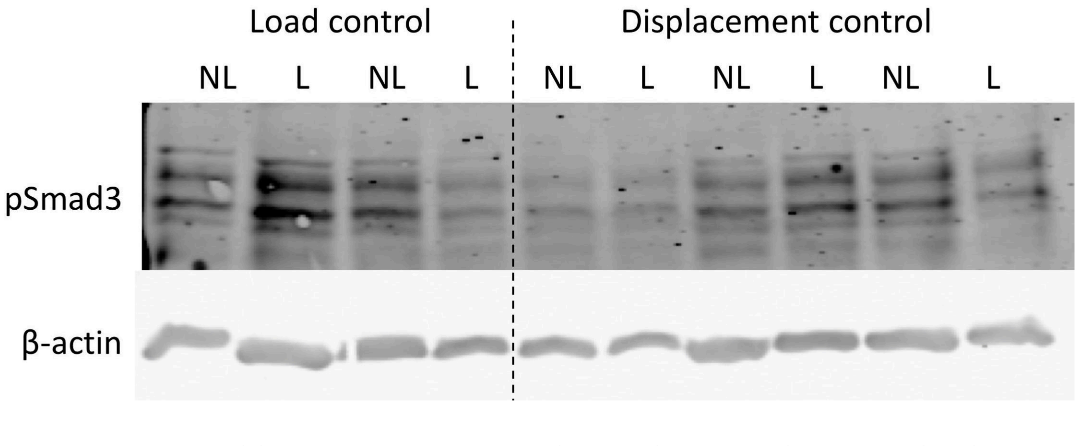

Figure 6.10: Western blot comparing pSmad3 mechanoregulation in load control and displacement control. The whole length of the tibia was collected two hours after one 10-minute loading session to a maximum of 3.5 N compression on the 50 lb load cell.

In August of 2016 I learned that the existing loading protocol which caused repression of pSmad3 did not use an anesthesia recovery agent, atipamezole, that I had thus far been using at the end of each loading session. My interpretation of the Western blots below was that without atipamezole, pSmad3 was suppressed by load, but that with atipamezole it was increased by load (Figure 6.11). This finding instigated the results detailed in Chapter 7 regarding adrenergic regulation of TGFβ signaling and mechanosensation. While the effect of atipamezole on load-induced Smad3 phosphorylation was not significant across multiple experiments, the mice did not appear to suffer from its omission, and so atipamezole was not used in the remainder of the loading experiments.

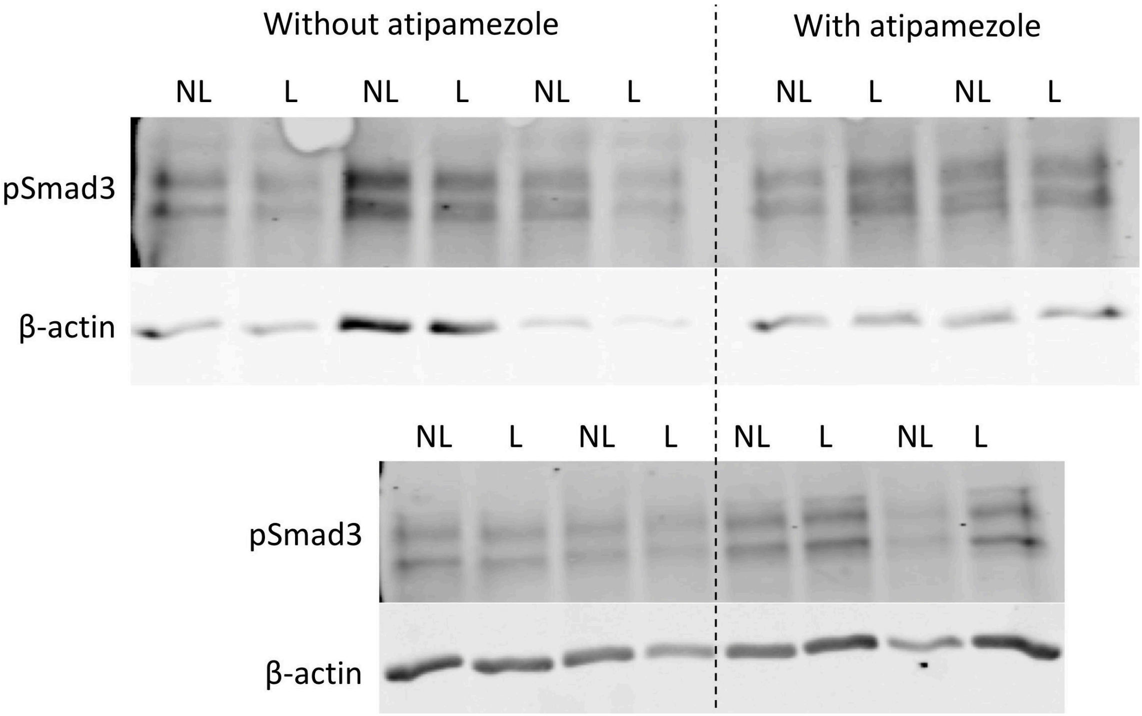

Figure 6.11: Effect of atipamezole on the mechanoregulation of pSmad3. The whole length of the tibia was collected four hours after one 10-minute loading session run on displacement-control with goal loads between 3.5 N and 0.5 N compression. Mice were either injected with atipamezole recovery agent immediately following loading or simply moved to a warm cage for recovery.

After the cessation of atipamezole administration, two other factors were changed in quick succession. First, to aid in mouse recovery from anesthesia, the concentration of xylazine in the injectable anesthesia mix was lowered from the original dose of 16 mg/kg to 10 mg/kg. Second, methods for protein harvest from loaded tibias were changed when the lab purchased a bead mill homogenizer that lyses bones with ceramic beads in individual tubes. This device helped me increase protein yield and produce Western blots with more even protein content across lanes. This blot (Figure 6.12) represents results from the nearly finalized loading parameters, with a displacement-controlled loading protocol being run to an attempted load of 3.5 N using the 50 lb load cell. Here, three different mice loaded to approximately 3N of maximum compression regulated pSmad3 in three different ways after load (upregulation, downregulation, and no change). Because Westerns are inherently semiquantitative, we turned to qPCR for further troubleshooting.

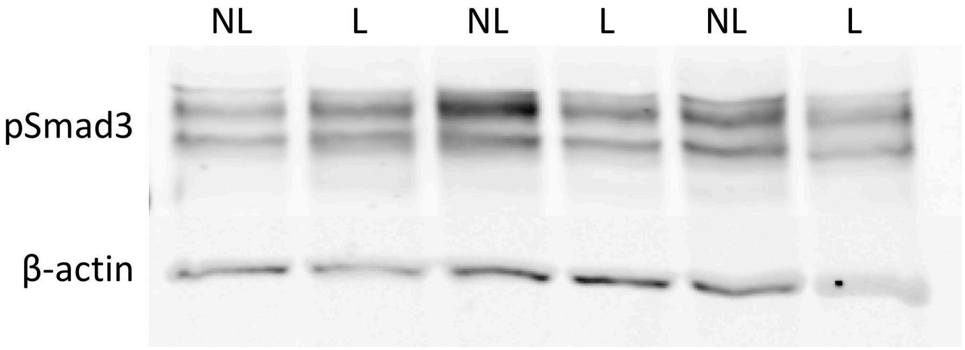

Figure 6.12: pSmad3 expression after loading with reduced xylazine in anesthesia. The whole length of the tibia was collected three hours after one 10-minute loading session run in displacement-control with goal loads between 3.5 N and 0.5 N compression. Xylazine in the anesthesia was reduced to 10 mg/kg and no atipamezole recovery agent was administered.

To evaluate the transcriptional response of bones to load in our system, tibias were loaded in displacement control to achieve maximum load amplitudes of 3-6 N. Loaded and non-loaded bones were harvested 24 hours post-load and processed for RNA. At 24 hours post-load, we evaluated sclerostin (Sost) and osteocalcin (OC) as positive controls, expecting that Sost would be downregulated and OC upregulated after load (9). Mmp13 was used as a metric of PLR activity. In whole tibias, in which we expect the signal to be dominated by proximal tissue, we found that Sost was significantly downregulated, but neither OC nor Mmp13 showed consistent load-dependent effects (Figure 6.13 A-C).

Additional mice were loaded to harvest and analyze gene expression in the distal portion of the tibia. In the distal tibia, both Sost and Mmp13 were significantly downregulated 24 hours post-load (Figure 6.13 D-E), and their mechanoregulation tended to be related within individual mice (Figure 6.13 F). The apparent co-regulation of Sost and Mmp13 in the distal tibia, and the absence of this relationship in the proximal-rich whole tibia, supports the possibility that distinct transcriptional responses occur in a location-dependent manner. The critical location-dependent factors could be related to local strains and fluid flow velocities, distinct mechanosensory mechanisms, or crosstalk with other nearby cell types.

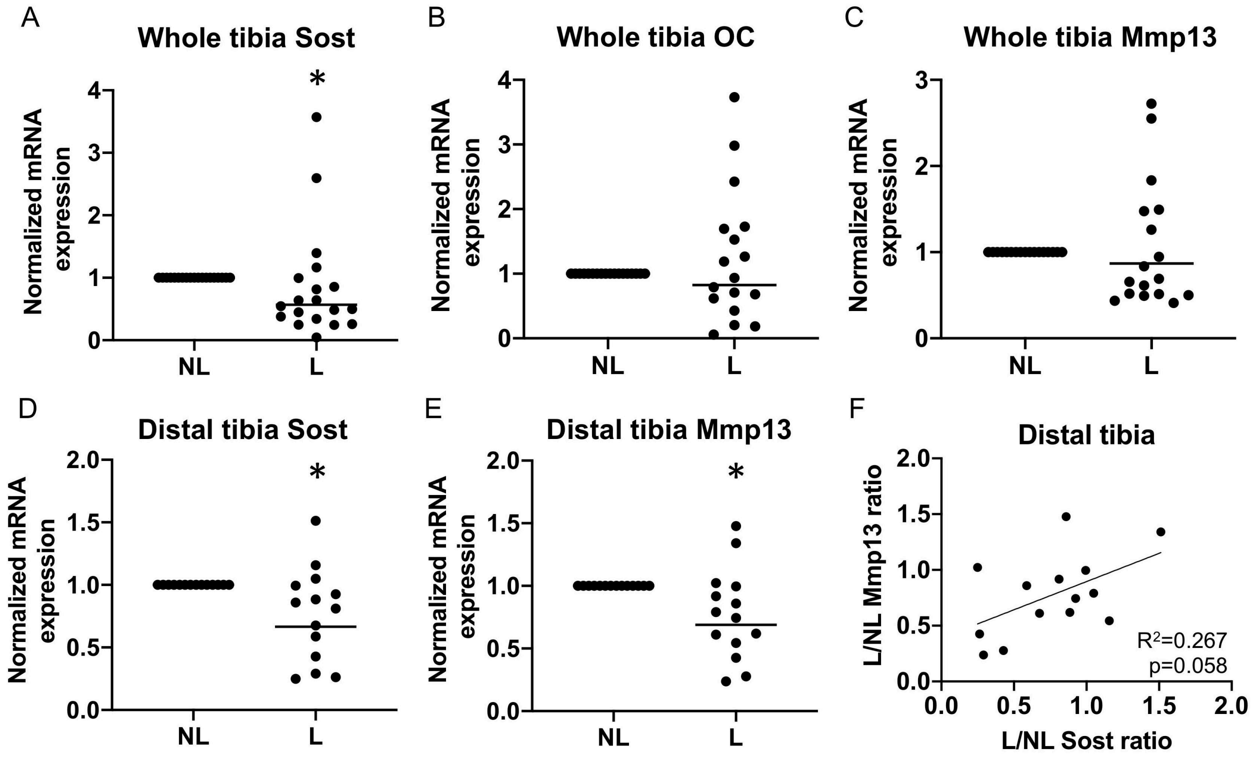

Figure 6.13: qPCR performed on tibias collected 24 hours after one 10-minute loading session. (A-C) Expression of Sost in the entire tibia is significantly downregulated, but OC and Mmp13 are not significantly changed. n=17-19. (D-E) In the distal region of the tibia, Sost and Mmp13 are both significantly downregulated. n=14. Bars show geometric mean. *p=0.02 by ratio paired t-test. (F) Mechanoregulation of Sost and Mmp13 is related within each distal tibia sample. β-actin was used as the housekeeping gene throughout.

Because the transcriptional response to load is dynamic, we also analyzed gene expression in proximal and distal tibias at 3 hours post-load. Based on prior studies on the effects of load on mouse bone gene expression in a hindlimb loading model, we expected Sost to be downregulated and Timp1 to be upregulated (9). We found no significant changes in Sost, Timp1, or Mmp13 expression post-load in proximal or distal tibia sections (data not shown). Although Sost was not significantly regulated by load, using proximal and distal sections of tibias rather than comparing whole tibias to distal tibias allowed pair-wise comparison of regional transcriptional control within each bone. We found a significant relationship between proximal and distal Sost expression, which was absent for Mmp13 (Figure 6.14). While use of different bones for regional comparisons at 24 hours post-load precludes the exact same analysis, the differences between Sost and Mmp13 expression at both timepoints might suggest that while Sost transcription is governed similarly throughout the whole bone, genes like Mmp13 have more site-specific mechanoregulation.

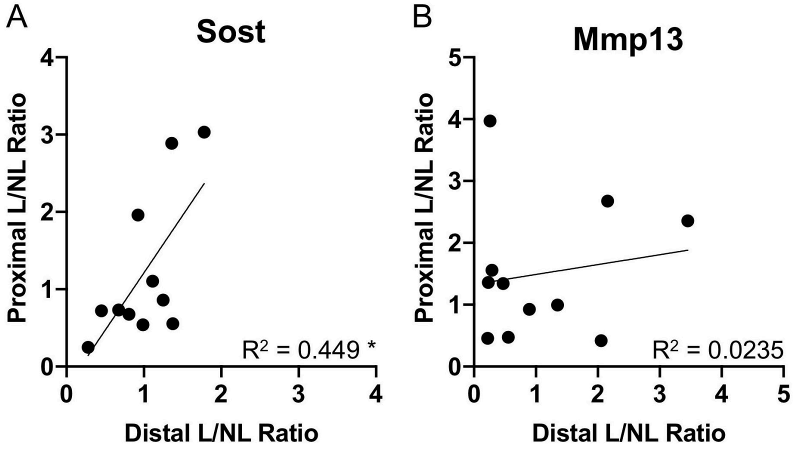

Figure 6.14: Regional relationships of gene expression in the tibia 3 hours after one 10-minute loading session. The ratio of gene expression in loaded to non-loaded samples is compared between the distal and proximal region, where each point represents one mouse. (A) Sost mechanoregulation is significantly correlated between regions of the same bone, *p=0.024, but (B) Mmp13 does not show the same relationship. β-actin was used as the housekeeping gene.

With the inherent variation in load applied when samples are individually calibrated for loading in displacement control, we expected that sclerostin expression might vary as a function of load applied to each mouse (16). Instead we found that no such relationship existed, and despite the wide range of loads experienced by different tibias, suppression of sclerostin seemed to occur randomly (Figure 6.15 A-B).

Investigation into the lack of anticipated relationship between Sost expression and load magnitude revealed that no relationship existed between actuator displacement amplitude and load feedback recorded during hindlimb loading sessions (Figure 6.15 C). This was concerning, because displacements were being determined based on load feedback in the first 30 seconds of setup for each mouse and were expected to correlate.

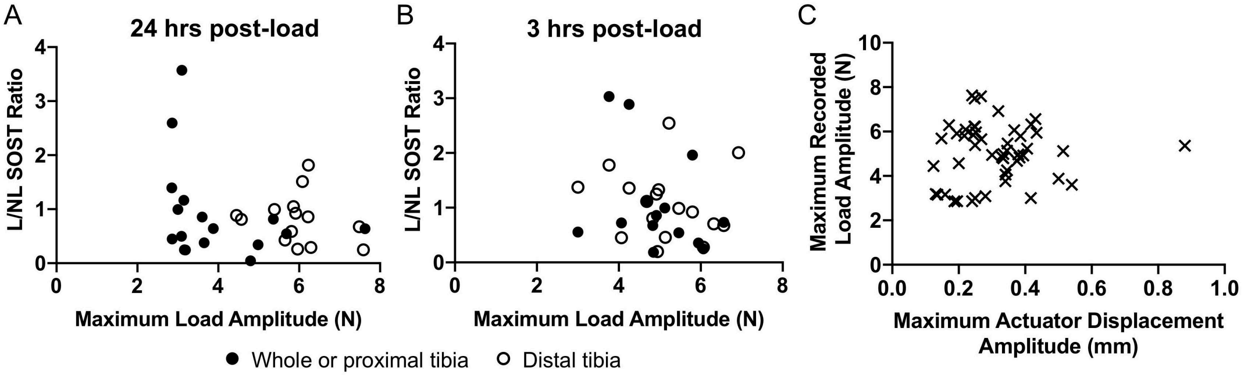

Figure 6.15: Relationship of Sost gene expression to applied load. (A-B) Sost gene expression data shown in Figure 6.13-6.14 is plotted relative to the amplitude of compressive load experienced by each loaded limb. No significant relationship is found. (C) The amplitude of compressive loading experienced by each loaded limb is plotted relative to the displacement settings used to run the loading session in displacement control. Each point represents one mouse used for RNA analysis at 3 or 24 hours. No significant relationship is found (n=49, p=0.65).

Further troubleshooting of the 50 lb load cell revealed that there was electrical interference causing an artificially high load readout of at least one Newton. When the actuator was set to cycle at a small displacement amplitude, the metal adapters connecting the load cell to the load frame caused a load readout to register despite the fact that nothing was touching the load cell. This false load readout in the non-loaded condition was corrected by the addition of plastic adapters to electrically isolate the load cell from the load frame (Figure 6.16, left).

Applying a small displacement amplitude to a mouse tibia in the original setup generated a much higher load response readout than that recorded in the same tibia when the load cell was electrically isolated (Figure 6.16, right). While the load amplitude appears similar in both mouse loading cases, the magnitude of applied load is artificially high when electrical interference is allowed. This finding suggested that when I had previously set up displacement control waveforms without isolation, the load readout appeared sufficiently high when the displacement amplitude was relatively small, causing a displacement amplitude that was lower than truly necessary to be selected for each mouse.

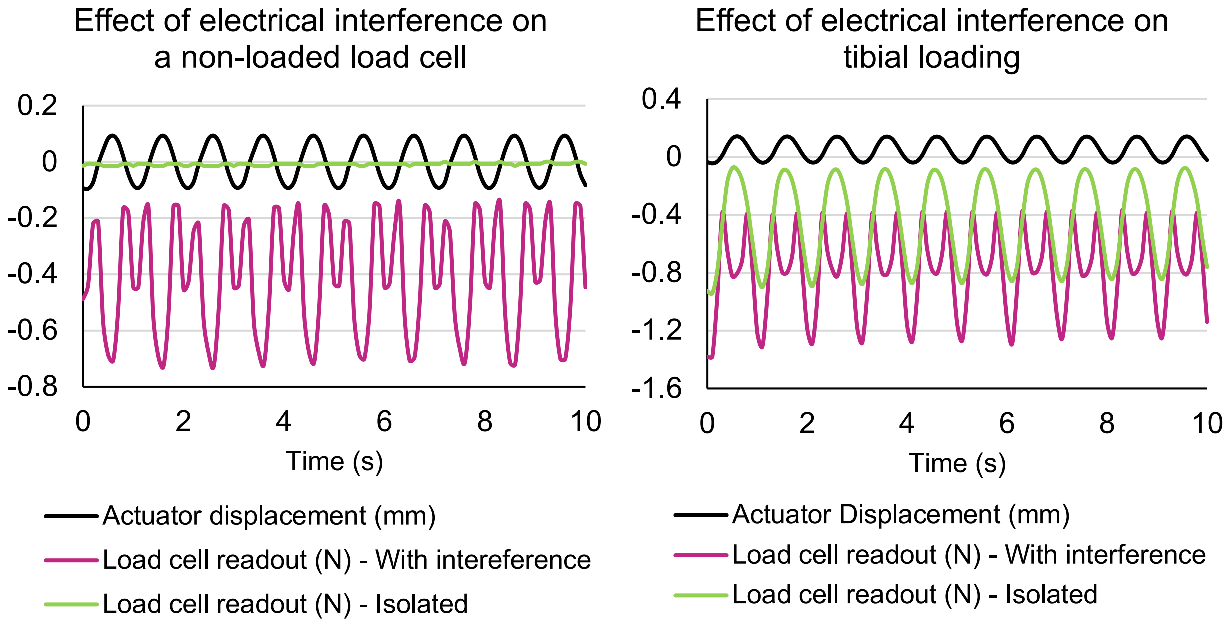

Figure 6.16: Effect of electrical interference on load readouts. Left panel: Load data registered while no mouse limb is in place to provide resistance to cyclic actuator displacement. Electrical interference causes false loads to register. Right panel: Load data registered on the same mouse limb under the same cyclic actuator displacement, with and without electrical isolation.

To further test the effects of electrical interference on displacement-controlled loading, I set up a waveform to apply a 5 N target load to a mouse tibia in both adapter configurations. As expected, a significantly higher displacement amplitude was required to achieve the desired load when the load cell was electrically isolated (Figure 6.17). The final load cell setup now includes plastic adapters and washers in order to minimize electrical interference.

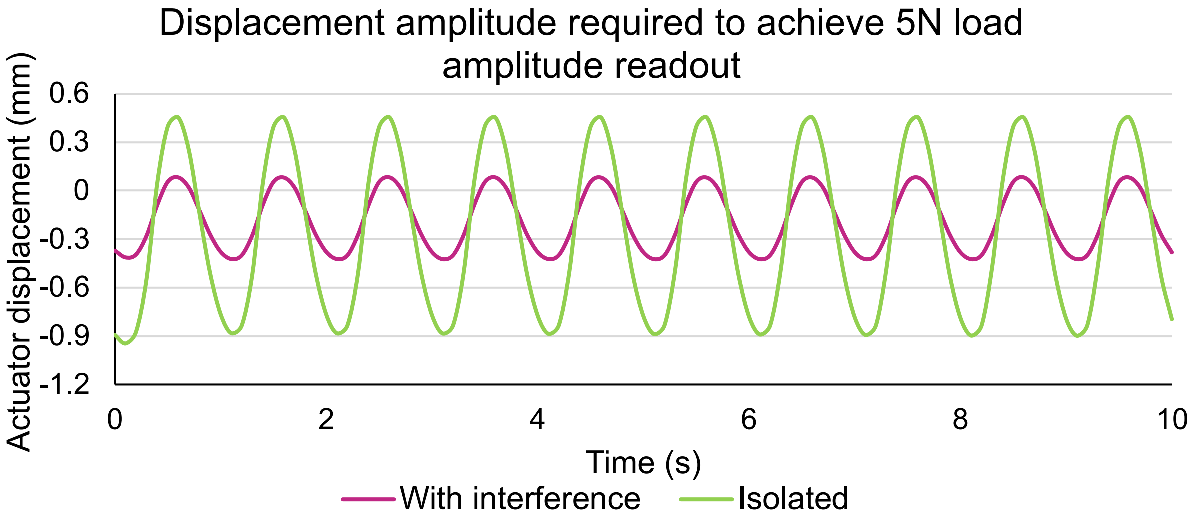

Figure 6.17: Effect of electrical interference on displacement amplitude selection. The displacement waveforms required to engender maximum compressive load of 5 N on the same mouse tibia with and without electrical interference are shown.

Posthoc analysis of waveforms from mouse tibial loading sessions between 2016-2019 demonstrates a significant load-displacement relationship when the load cell is isolated (Figure 6.18). Extrapolation of this data also suggests, but cannot confirm, that loads applied to mice on the 50 lb load cell while electrical interference was occurring were likely in the range of 2-4 N peak amplitude. Therefore, previous experiments performed on the 50 lb load cell (Figures 6.8 – 6.15) are not strictly invalidated by the finding that electrical interference was present. Rather, the high variability of mechanosensitive responses may be partially explained by the low magnitude of mechanical stimuli. Similarly, loading sessions conducted on the 10 lb load cell (Figures 6.2 – 6.7), while not affected by electrical interference, also likely provided quite small stimuli due to the non-axial alignment.

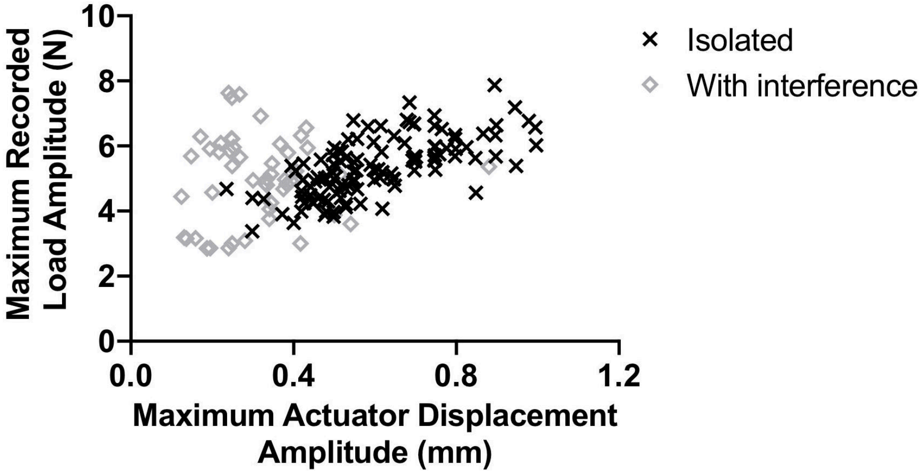

Figure 6.18: Relationship between actuator displacement and recorded load. Each point represents one loading session for one mouse. The amplitude of compressive loading experienced by each loaded limb is plotted relative to the displacement settings used to run the loading session in displacement control. The "with interference" points are the same as those shown in Figure 6.15 C, replotted here for comparison. A significant correlation exists when the load cell is electrically isolated (n=116 , p<0.0001).

To better secure the mouse foot during application of new higher loads, I generated a foot holder that constrains the foot laterally and maintains the ankle at a slight angle to prevent slipping of the heel into a non-axial loading position (Figure 6.1 C). When mouse tibias are axially loaded in this configuration, we see load-dependent phosphorylation of Akt and load-dependent increases in mineral apposition rate and bone formation rate measured from double fluorochrome labelling (Chapter 8).

To check whether any of the applied loads are damaging, we dissected loaded and non-loaded tibias immediately after a single loading session and tested their flexural properties in three-point bending (Figure 6.19). No significant differences in stiffness or ultimate load were observed between loaded and non-loaded bones in either load range tested. Importantly, axial applied loads up to 8 N have not been observed to cause ACL tears in our setup.

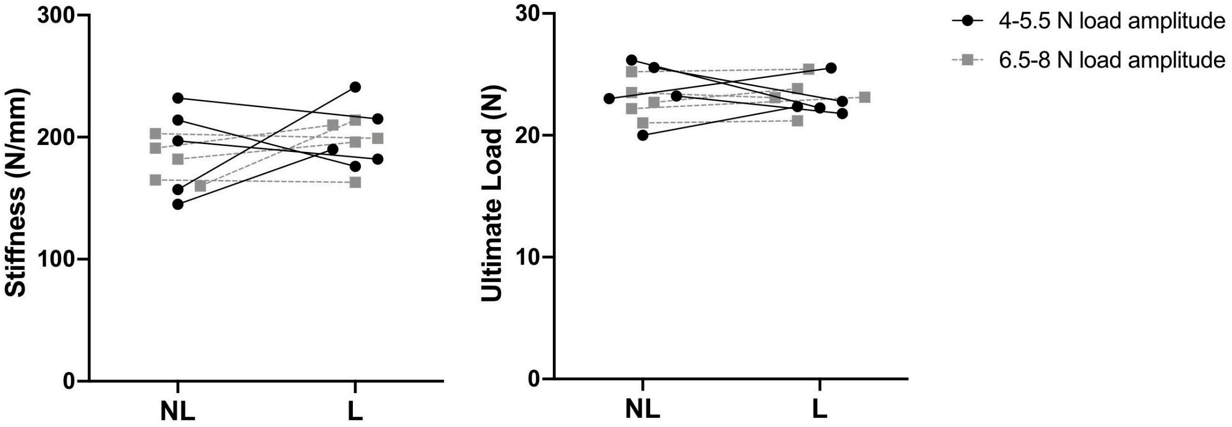

Figure 6.19: Flexural properties of tibias collected immediately after a single 10-minute loading session. Lines connect non-loaded and loaded tibias from the same animal. No load-induced changes in mechanical properties were observed at either load range. n=5 per group.

Finally, to calculate the load-induced strains on the tibia, a separate set of euthanized mice were used. Muscle was dissected from the right tibia and strain gages were adhered to the antero-medial surface of the bone. The mouse was then situated in the load frame and displacement-controlled sinusoidal waveforms of increasing amplitude were applied to induce a range of loads and strains, which were recorded in real time. The relationship between applied load and tensile strain on the anteromedial surface was linear, with loads of 6 N generating approximately 1050 microstrain (Figure 6.20). These results were comparable to numerous other tibial loading studies (5, 19–22). However, in our loading setup, likely due to the high degree of knee flexion, loads of 10-13 N tended to tear the ACL, which precludes us from consistently engendering strains above 1500.

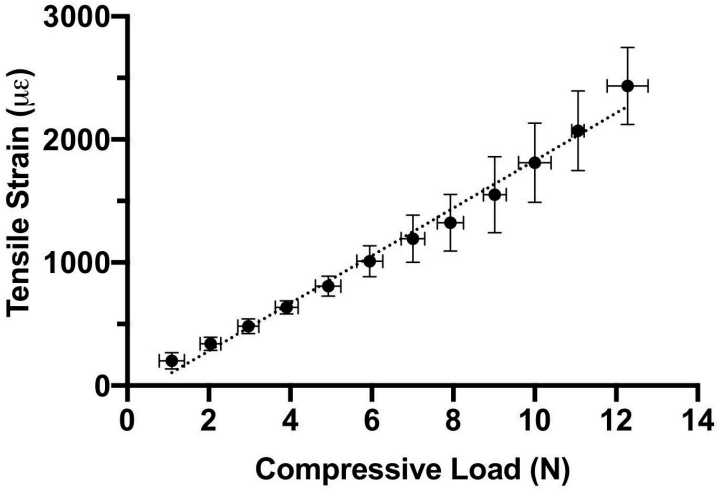

Figure 6.20: Tensile strain engendered on the anteromedial surface of the mouse tibia by compressive loads applied through the flexed knee. n=5 legs. R^2 = 0.91. p<0.0001.

The murine axial tibial loading protocol is now optimized within the constraints of currently available materials at UCSF. For future optimization, I suggest purchasing a new load cell that is aligned, not prone to electrical interference, and sensitive enough to run on load control. New custom adapters could also be machined to decrease the number of connections in the setup and allow the mouse knee to rest at 90 degrees of flexion during loading. Biological conclusions about the effect of load on TGFβ signaling and PLR-related gene expression are reserved for Chapter 8, in which the optimized loading protocol is consistently applied.

References

1. McClanahan BS, et al. (2002) Side-to-side comparisons of bone mineral density in upper and lower limbs of collegiate athletes. *J strength Cond Res* 16(4):586–590.
2. LeBlanc A (1995) *Space flight bone studies*.
3. BIERING-SØRENSEN F, BOHR HH, SCHAADT OP (2008) Longitudinal study of bone mineral content in the lumbar spine, the forearm and the lower extremities after spinal cord injury. *Eur J Clin Invest* 20(3):330–335.
4. Main RP, et al. (2019) Murine Axial Compression Tibial Loading Model to Study Bone Mechanobiology: Implementing the Model and Reporting Results. *J Orthop Res* n/a(n/a). doi:10.1002/jor.24466.
5. Fritton JC, Myers ER, Wright TM, Van Der Meulen MCH (2005) Loading induces site-specific increases in mineral content assessed by microcomputed tomography of the mouse tibia. *Bone* 36(6):1030–1038.
6. Srinivasan S, Weimer DA, Agans SC, Bain SD, Gross TS (2002) Low-Magnitude Mechanical Loading Becomes Osteogenic When Rest Is Inserted Between Each Load Cycle. *J Bone Miner Res* 17(9):1613–1620.
7. Sun D, Brodt MD, Zannit HM, Holguin N, Silva MJ (2018) Evaluation of loading parameters for murine axial tibial loading: Stimulating cortical bone formation while reducing loading duration. *J Orthop Res* 36(2):682–691.
8. Yang H, Embry RE, Main RP (2017) Effects of Loading Duration and Short Rest Insertion on Cancellous and Cortical Bone Adaptation in the Mouse Tibia. *PLoS One* 12(1):e0169519–e0169519.
9. Kelly NH, Schimenti JC, Ross FP, van der Meulen MCH (2016) Transcriptional

profiling of cortical versus cancellous bone from mechanically-loaded murine tibiae reveals differential gene expression. *Bone* 86:22–29.

10. Sugiyama T, Price JS, Lanyon LE (2010) Functional adaptation to mechanical loading in both cortical and cancellous bone is controlled locally and is confined to the loaded bones. *Bone* 46(2):314–321.
11. Warden S., Turner C. (2004) Mechanotransduction in the cortical bone is most efficient at loading frequencies of 5–10 Hz. *Bone* 34(2):261–270.
12. Robling AG, Hinant FM, Burr DB, Turner CH (2002) Improved bone structure and strength after long-term mechanical loading is greatest if loading is separated into short bouts. *J Bone Miner Res* 17(8):1545–1554.
13. Holguin N, Brodt MD, Silva MJ (2016) Activation of Wnt Signaling by Mechanical Loading Is Impaired in the Bone of Old Mice. *J Bone Miner Res* 31(12):2215–2226.
14. Lara-Castillo N, et al. (2015) In vivo mechanical loading rapidly activates β-catenin signaling in osteocytes through a prostaglandin mediated mechanism. *Bone* 76:58–66.
15. Zaman G, et al. (2010) Loading-related regulation of gene expression in bone in the contexts of estrogen deficiency, lack of estrogen receptor α and disuse. *Bone* 46(3):628–642.
16. Robling AG, et al. (2008) Mechanical stimulation of bone in vivo reduces osteocyte expression of Sost/sclerostin. *J Biol Chem* 283(9):5866–5875.
17. Roosa SMM, Liu Y, Turner CH (2011) Gene Expression Patterns in Bone Following Mechanical Loading. *J bone Miner Res* 26(1):100–112.
18. Nguyen J, Tang SY, Nguyen D, Alliston T (2013) Load Regulates Bone Formation and

Sclerostin Expression through a TGF b -Dependent Mechanism. *PLoS One* 8(1):e53813.

19. Jing D, et al. (2014) In situ intracellular calcium oscillations in osteocytes in intact mouse long bones under dynamic mechanical loading. *FASEB J* 28(4):1582–1592.

20. Weatherholt AM, Fuchs RK, Warden SJ (2013) Cortical and trabecular bone adaptation to incremental load magnitudes using the mouse tibial axial compression loading model. *Bone* 52(1):372–379.

21. Berman AG, Clauser CA, Wunderlin C, Hammond MA, Wallace JM (2015) Structural and Mechanical Improvements to Bone Are Strain Dependent with Axial Compression of the Tibia in Female C57BL/6 Mice. *PLoS One* 10(6). doi:10.1371/journal.pone.0130504.

22. Sugiyama T, et al. (2012) Bones' adaptive response to mechanical loading is essentially linear between the low strains associated with disuse and the high strains associated with the lamellar/woven bone transition. *J Bone Miner Res* 27(8):1784–1793.

Chapter 7

Interactions between adrenergic signaling and TGFβ in vitro

Introduction

A large body of work supports the role of the central and peripheral nervous system in bone development, homeostasis, and anabolism (1). The periosteum is densely innervated with sensory and sympathetic nerves, and nerves accompany blood vessels through the mineralized bone and into the marrow (2, 3). Nerve fibers have even been observed in direct contact with osteoblasts and hematopoietic cells (4). In humans, spinal cord injury causes rapid loss of bone mass that is greater than would be expected from disuse alone, supporting a critical role for the nervous system in bone homeostasis (5). Innervation by sensory nerves is essential for proper ossification during development and contributes to load-induced bone formation (6–8). The sympathetic nervous system regulates bone mass through local and systemic mechanisms (9). Given the many possibilities for crosstalk between bone and the nervous system, it is important to better understand the role of the nervous system in bone.

Furthermore, it is essential to understand the effects on bone of experimental agents used in research that act by manipulating the molecular pathways involved in the nervous system, such as anesthetics and sedatives.

The effect of the sympathetic nervous system (SNS) on bone has garnered substantial interest due to the numerous pharmacologic agents targeting adrenergic receptors, which mediate most of the effects of the SNS. Adrenergic signaling involves three main types of transmembrane G-protein coupled receptors: α1, α2, and β. In response to neurotransmitters like norepinephrine (NE) or circulating epinephrine, α1 receptors activate phospholipase C and increase protein kinase C activity, which mediates further downstream effects. Signaling through α2 receptors inhibits adenylyl cyclase activity, whereas β-type receptors activate adenylyl cyclase (Figure 7.1). When adenylyl cyclase is active, it generates cyclic AMP, which activates protein kinase A (PKA), which can phosphorylate transcription factors like Creb. β-blockers, generally prescribed for management of blood pressure, decrease sympathetic tone and have a modest but significant beneficial effect on bone mass and fracture risk (10, 11). Clonidine, which decreases sympathetic activity via α2-adrenergic receptors, increases bone resorption in humans (12). These seemingly contradictory effects demonstrate the receptor-specific control of sympathetic activity and emphasize the large gap in knowledge regarding the specific regulatory mechanisms linking the SNS to bone homeostasis.

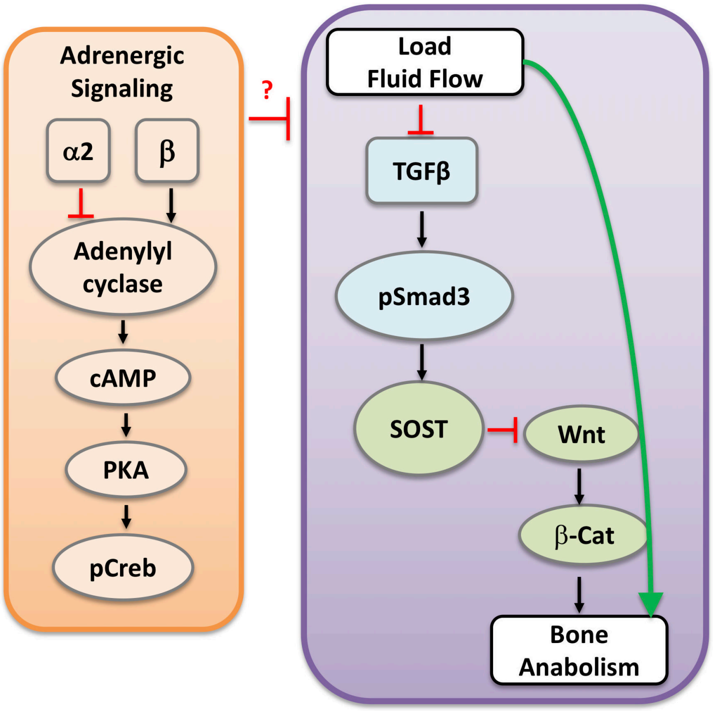

Figure 7.1: α2 and β-adrenergic receptors have opposing effects on downstream adrenergic signaling and may modulate the normal response of TGFβ signaling to mechanical stimulation.

In addition to expression within the nervous system, α2- and β-adrenergic receptors are also expressed in osteoblasts, osteoclasts, and osteocytes (13). The ability of sympathetic hyperactivity to induce osteopenia has been attributed to NE signaling through osteoblastic β2-adrenergic receptors, which promotes RANKL expression and subsequent bone loss (14). This relationship between β-adrenergic signaling and RANKL expression has also been demonstrated in osteocytes (15, 16). However, systemic ablation of two inhibitory α2 isoforms in mice caused sympathetic hyperactivity, high plasma NE and a high bone mass phenotype even though β2-adrenergic receptors were intact (13). Recent work has demonstrated that osteoblasts and osteocytes in cortical bone express norepinephrine transporter, which acts to limit the extracellular concentration of NE (17). Thus, in addition to presynaptic reuptake of NE, osteocytes can participate in regulating NE in their local environment that may otherwise interact with α- or β-receptors. Despite the demonstrated importance of adrenergic signaling at the cellular level in bone, the specific signaling pathways linking α2- and β-adrenergic receptors to changes in bone mass are incompletely understood.

In the course of troubleshooting the in vivo tibial loading protocol that had previously caused repression of transforming growth factor beta (TGFβ) signaling in osteocytes (Chapter 6), a possible role for adrenergic signaling in the mechanosensitive regulation of TGFβ signaling was identified. To sedate and anesthetize mice for loading sessions, injectable ketamine-xylazine bypasses the spatial constraints and human exposure concerns of inhaled isofluorane. Ketamine, an uncompetitve NMDA receptor antagonist, and xylazine, an adrenergic α2 receptor agonist, together act on the central nervous system to provide sedative and analgesic effects for 10-30 minutes. Specifically, xylazine mimics NE in the synapse, binds to presynaptic autoreceptors, and inhibits further NE release. To hasten recovery from anesthesia, this effect can be reversed by α2 antagonists like atipamezole, which prevent NE feedback to autoreceptors and stimulate further neurotransmitter release. In humans, atipamezole can increase norepinephrine and epinephrine levels detectable in the circulation (18). Atipamezole in particular became an interesting variable because its use seemed to cause consistent upregulation of pSmad3 post-load, whereas experiments conducted without atipamezole more often found repression of pSmad3 post-load (19)(Chapter 6).

Several studies have described interactions between TGFβ signaling and adrenergic signaling, but none have identified this relationship in bone. Serpine1 expression in cardiac fibroblasts is stimulated by neurotransmitter norepinephrine and acts additively with TGFβ

(20). In cancer cells, norepinephrine stimulated production of TGF-β ligand (21). TGFβ may also be able to act on adrenergic signaling pathways, as low concentrations of TGFβ were found to induce PKA activity in Mv1Lu cells (22). This raised the possibility that adrenergic signaling was interacting with TGFβ in the context of mechanosensation, either through a cell-intrinsic mechanism, innervation of bones, or delivery of epinephrine and norepinephrine through the circulation (Figure 7.2). Given the important role of TGFβ in the skeleton and the known interactions between TGFβ signaling and adrenergic signaling in other cell types, we tested the hypotheses that adrenergic signaling regulates TGFβ in osteocytes and that physical cues, such as fluid flow shear stress, interfere with this regulation.

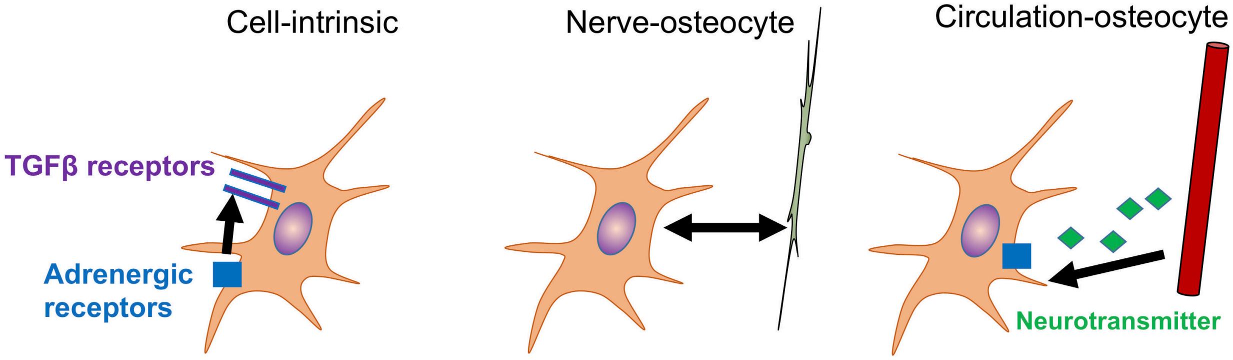

Figure 7.2: Possible mechanisms of crosstalk between adrenergic signaling and TGFβ signaling in osteocytes. Left, atipamezole could directly stimulate α2-adrenoreceptors on osteocytes and integrate with TGFβ in a cell-intrinsic manner. Center, atipamezole's effects on the sympathetic nervous system could propagate to osteocytes through nerves. Right, neurotransmitters released into circulation after atipamezole administration could stimulate multiple adrenergic receptors on osteocytes.

Methods

Cells

Osteocyte MLO-Y4 and OCY454 cell lines were cultured as described in Chapter 2. OCY454 cells were differentiated at 37 °C for 14 days before treatment. While MLO-Y4 cells do not express sclerostin, OCY454 cells differentiated for 14 days robustly express osteocytic markers Dmp1, Sost, and Phex (Figure 7.3). Additionally, human epithelial kidney cells (HEK293) were selected for their known expression of adrenergic receptors. HEK293 cells were cultured on tissue culture plastic in DMEM with 10% FBS and 1% P/S at 37 °C.

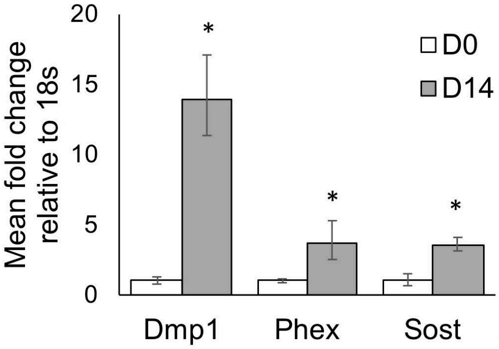

Figure 7.3: Osteocytic gene expression in OCY454 cells. RNA was collected from confluent, undifferentiated cells (D0) and cells differentiated for 14 days (D14) after one hour in treatment media containing 1% FBS. Bars represent mean +/- SD from three replicates in one experiment. *p<0.01.

Cell treatments

Treatment media contained 10% of the serum of culture media. Aliquots of treatment media were prepared with drugs and equal concentrations of vehicle, then split over wells of different timepoints. Forskolin (F3917) stocks were prepared in DMSO at 40 mM and stored at -20 °C. (-)-norepinephrine (A7257) is initially dissolved at 80 mM in 100 μm HCl, then diluted 4x in sterile water, aliquoted, and stored at -20 °C. Isoproterenol (I5627) stocks were prepared in sterile water at 100 mM. H-89 (B1427) stocks were prepared in DMSO at

50 mM and stored at -20 °C. Atipamezole (5 mg/mL stock) and xylazine (100 mg/mL stock) are liquid formulations stored at room temperature. TGFβ1 ligand (Peprotech) is prepared in sterile water at 5 μg/mL, and all treatments were given at 5 ng/mL.

Western blotting

At the end of treatment, media was aspirated and cell culture wells were washed with cold D-PBS. Plates were placed on ice, and cell lysis buffer (50 mM Tris pH 7.5, 150 mM NaCl, 2 mM EDTA, 0.5% NP-40, 0.25% sodium deoxycholate, supplemented with protease and phosphatase inhibitor tablets) was added to wells. Cell lysate was then collected, sonicated in an ice water bath for 5 15-second bursts, centrifuged at 12,000 g for 10 minutes, and liquid supernatant stored at -20 °C. Equal volumes of protein from each condition or replicate were loaded in 10% SDS-polyacrylamide gels for electrophoresis. Primary antibodies used for Western blots are described in Table 2.2.

Quantitative RT-PCR and PCR

At the end of treatment, media was aspirated and cell culture wells were washed with cold D-PBS. Plates were placed on ice, and TRIzol was added to wells. Cell lysate was then collected and stored at -80 °C until RNA harvest, reverse transcription, and qPCR, as described in Chapter 2. Expression was quantified by the ΔΔCt method with the housekeeping genes designated in each figure.

For PCR, RNA was additionally collected from mouse kidney and mouse tibia without marrow by homogenization in TRIzol. Equal concentrations of cDNA from mouse tissues and untreated OCY454 cells were used for PCR with primers for adrenergic receptors (Table 2.3).

Results

Adrenergic signaling is functionally intact in osteocytes and dominated by β-adrenergic receptors

Expression of adrenergic receptors and existence of the signaling cascade from adenylyl cyclase to PKA have been identified in osteocytes (13, 23, 24), but their functional coupling and ability to stimulate pCreb in osteocytes has not been demonstrated (Figure 7.1). To test whether adrenergic signaling can occur in an osteocyte-intrinsic manner, we treated cells in culture with forskolin and with norepinephrine.

As expected in HEK293 cells, forskolin stimulation of adenylyl cyclase induced rapid, dose-dependent Creb phosphorylation (Figure 7.4). In MLO-Y4 and OCY454 osteocyte cell lines, forskolin also stimulated pCreb within 15 minutes of exposure. In all cells, the magnitude of the effect was sustained through 30 minutes.

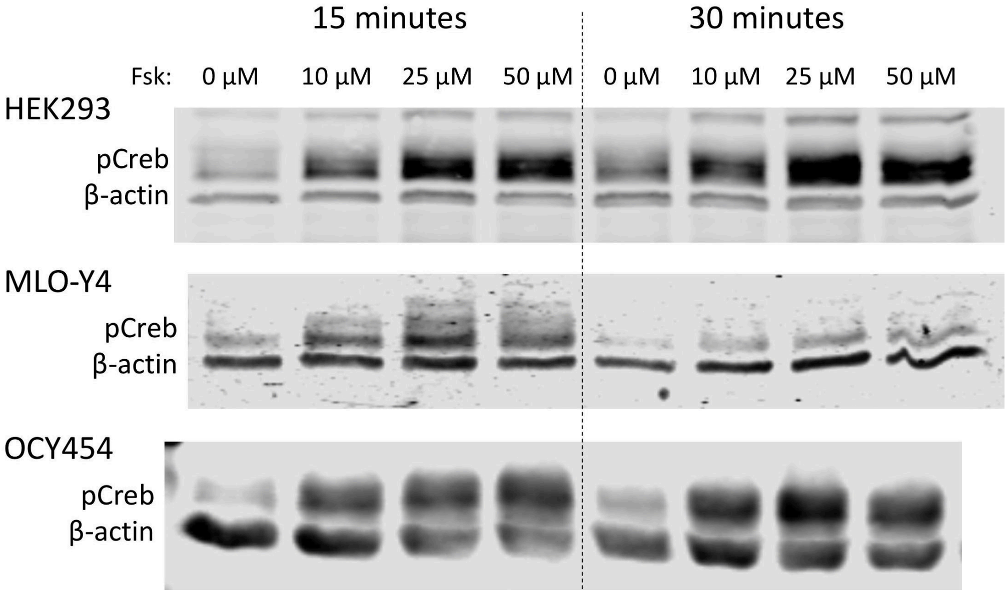

Figure 7.4: Intracellular signaling from adenylyl cyclase to pCreb is intact in osteocytes. Cells were cultured with forskolin (Fsk) at the indicated concentrations or with an equal volume of DMSO vehicle for 15 or 30 minutes.

Since norepinephrine can interact with α2- and β-adrenoreceptors to induce opposing effects on adenylyl cyclase (Figure 7.1), we were not sure whether we would see induction or repression of pCreb if osteocytic adrenergic receptors were indeed functional. In all three cell types, norepinephrine induced pCreb at most concentrations by 30 minutes (Figure 7.5 A). Results collected at 60 minutes showed a similar trend. We performed PCR on OCY454 cells and on cDNA from mouse kidneys and tibias to confirm the expression of both α2- and β-adrenergic receptors in our samples. As reported by Fonseca et al, we found that α2a, α2c, and β2 receptors are expressed in bone. OCY454 cells expressed predominantly α2a and β2 receptors. We focused on the β2 subtype because it has previously been shown to play a key role in sympathetic regulation of bone mass (14). Therefore, adrenergic signaling from the receptor level to the effector pCreb is intact in osteocytes, and while osteocytes express α2- and β-adrenoreceptors, the adenylyl cyclase-activating β-receptors appear to be functionally predominant.

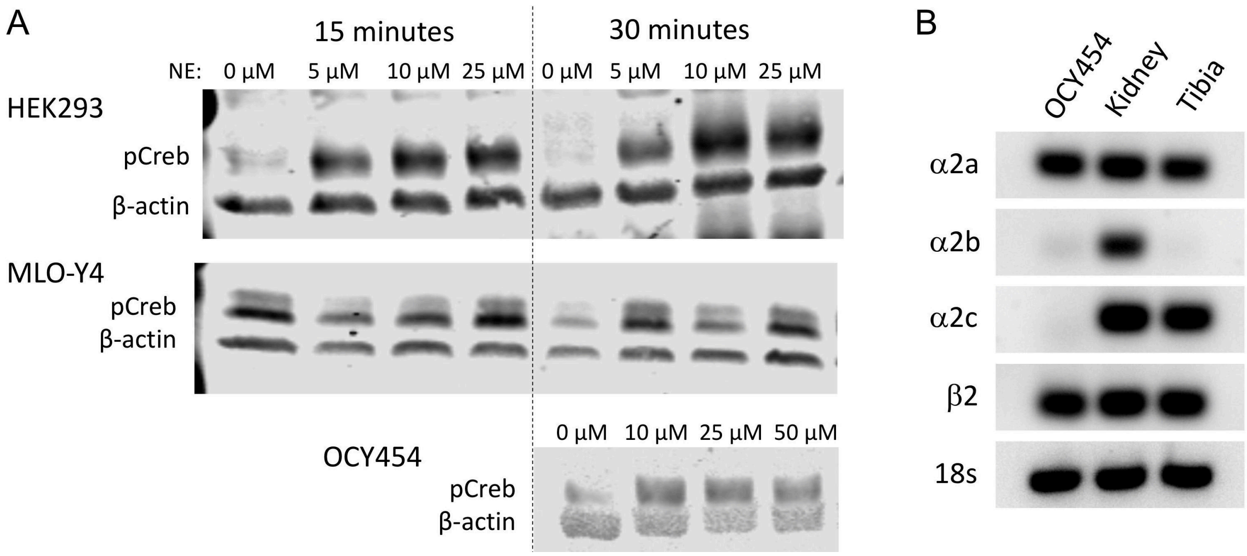

Figure 7.5: Adrenergic signaling from norepinephrine to pCreb is intact in osteocytes. (A) Western blots of cells treated with norepinephrine (NE) at the indicated concentrations or

with an equal volume of acid vehicle for 15 or 30 minutes. (B) PCR of adrenoreceptor subtybes expressed in OCY454, mouse kidney, and mouse tibia.

We hypothesized that if β-adrenergic receptors dominate the norepinephrine response in osteocytes, then direct stimulation of β-adrenergic receptors would induce a similar pCreb response. Indeed, a 1 μM dose of isoproterenol, a non-selective agonist of β-adrenergic receptors, was sufficient to double Creb phosphorylation in OCY454 cells, an effect that strengthened and persisted longer with higher doses (Figure 7.6). Therefore, if neurotransmitters released into circulation after atipamezole treatment reach osteocytes, they may induce an osteocyte-intrinsic signaling cascade through β-adrenergic receptors.

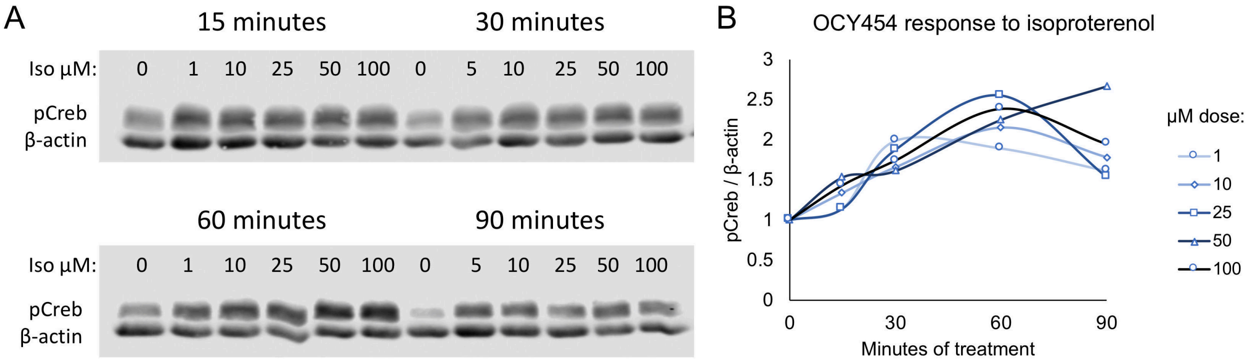

Figure 7.6: Isoproterenol stimulates pCreb in osteocytes. (A) Western blots of OCY454 cells treated with isoproterenol (Iso) at the indicated concentrations for 15-90 minutes. (B) Quantification of pCreb relative to β-actin control for n=1 replicate per condition/timepoint.

Direct action of xylazine and atipamezole on osteocytes is unlikely

The anesthesia component xylazine and the reversal agent atipamezole both act on α2 receptors, but their ability to initiate downstream signaling in an osteocyte-intrinsic manner is unknown. Xylazine, an agonist of inhibitory α2 receptors, would be expected to repress pCreb. The effect was actually more complex than expected, with a possible short-term upregulation of pCreb followed by slight repression. HEK293 cells and OCY454 cells, in particular, showed a slight reduction in pCreb after 30-60 minutes of treatment (Figure 7.7).

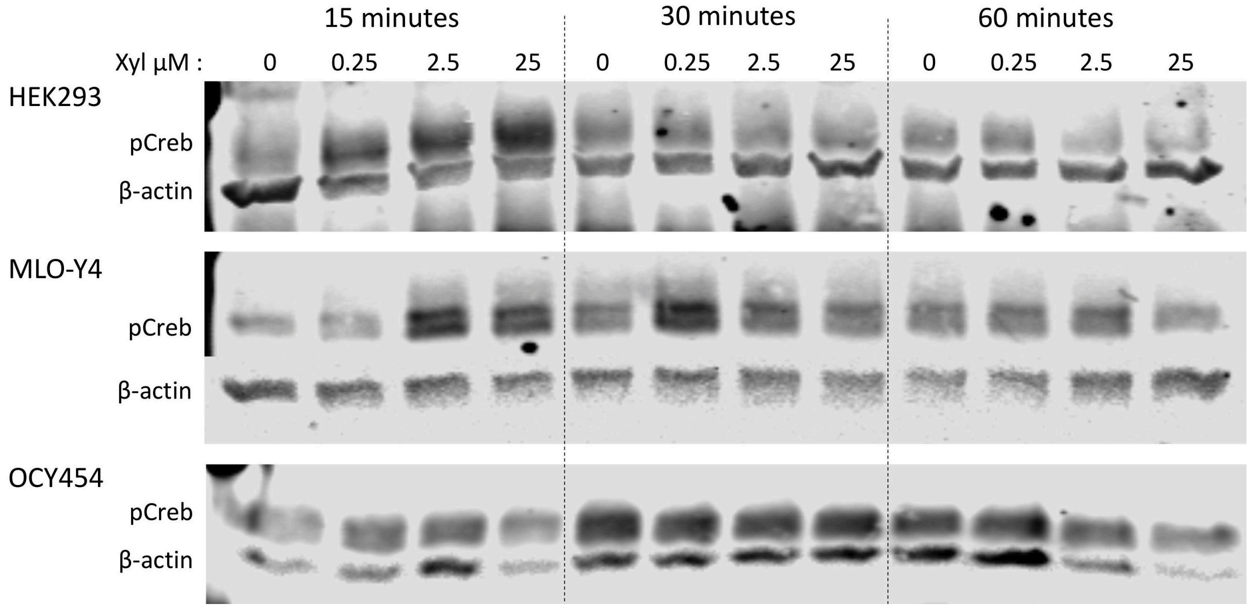

Figure 7.7: Xylazine may repress pCreb in osteocytes. Cells were treated with xylazine (Xyl) at the indicated concentrations for 15-60 minutes. n=1 replicate per condition/timepoint.

Atipamezole, as an antagonist of the inhibitory α2 receptors, would be expected to increase pCreb. We saw a modest increase in pCreb in two cell types with low doses of atipamezole (Figure 7.8), but it would probably cause a bigger increase in conjunction with isoproterenol-induced activation of β-adrenergic receptors.

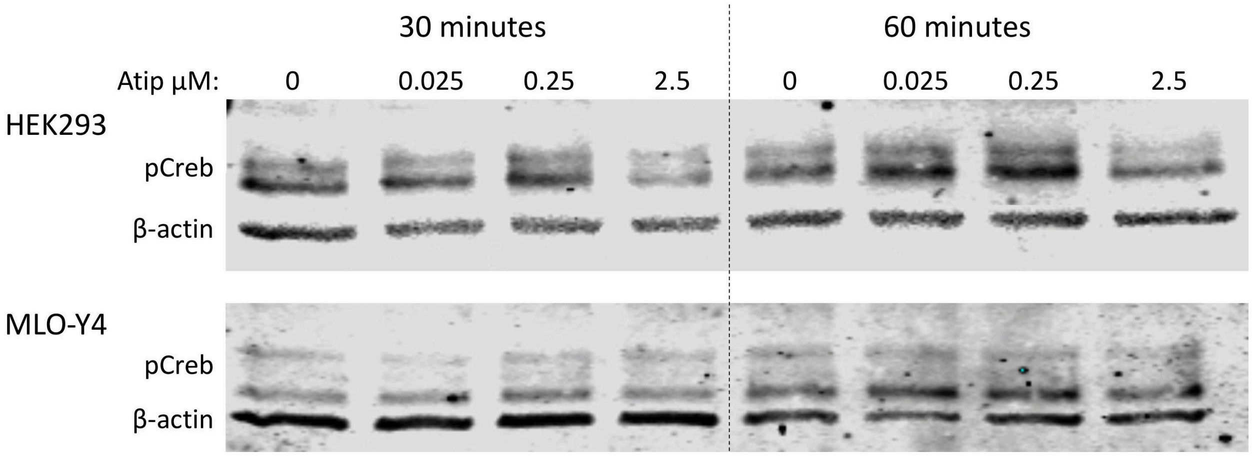

Figure 7.8: Atipamezole may induce pCreb in osteocytes. Cells were treated with atipamezole (Atip) at the indicated concentrations for 30-60 minutes. n=1 replicate per condition/timepoint.

Compared to stimulation of β-adrenergic receptors, osteocyte-intrinsic stimulation and inhibition of α2-adrenergic receptors cause a weaker effect. We therefore hypothesize that xylazine and atipamezole do not act directly on osteocytes in vivo, and the more meaningful stimulus is the change in norepinephrine in circulation and from local sympathetic nerves which serves to activate β-adrenergic receptors on osteocytes to interfere with TGFβ signaling.

Forskolin regulates canonical and non-canonical TGFβ signaling in osteocytes

To test the hypothesis that β-adrenergic signaling regulates TGFβ signaling, we used forskolin to stimulate the intracellular signaling cascade following β-AR activation. As expected, forskolin significantly induced pCreb in OCY454 cells with 15-90 minutes of treatment (Figure 7.9). To determine the effect of forskolin on TGFβ signaling, we evaluated its ability to regulate canonical effector pSmad3 and non-canonical effectors p-p38 and pAkt. p-p38 and pAkt were significantly induced and repressed, respectively, by forskolin treatment, indicating robust adrenergic regulation of non-canonical TGFβ signaling. The effect of forskolin on pSmad3 was modest but significant at 15 min, but not at other time points. However, in multiple independent experiments on OCY454 and MLO-Y4 cells (Figure 7.10), we consistently saw forskolin-induced upregulation of pSmad3 with 15-30 minutes of treatment and downregulation of pSmad3 to 50%-90% of untreated levels after 60-90 minutes of treatment. Therefore, forskolin regulates canonical and non-canonical TGFβ effectors.

We also investigated the effect of 1 μM isoproterenol on TGFβ signaling. We found that pCreb and pSmad3 were significantly induced by β-adrenergic stimulation after 60 minutes of treatment, but the difference was not significant by 90 minutes (n=3, data not shown). This may indicate that the signaling timeline is lengthened by stimulating at the receptor level rather than activating adenylyl cyclase. Additional experiments with longer treatments or higher concentrations of isoproterenol will be necessary to discern any receptor-specific effects.

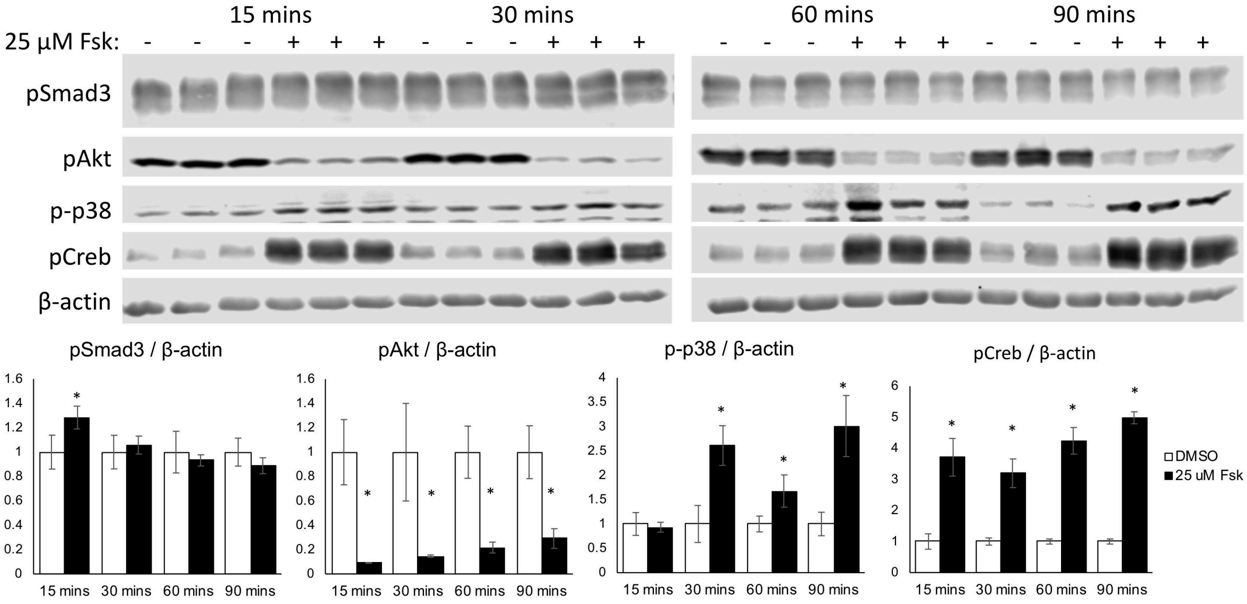

Figure 7.9: Forskolin regulates TGFβ effectors in osteocytes. OCY454 cells were treated with 25 µM forskolin or DMSO vehicle for the indicated times. Graphs show mean +/- SD of three replicates for each timepoint. *p<0.05.

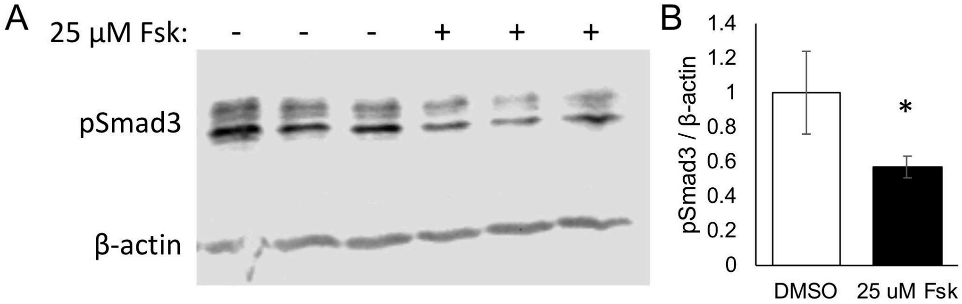

Figure 7.10: Forskolin represses pSmad3 in MLO-Y4 cells. (A) Western blot of MLOY4 cells treated with 25 µM forskolin or DMSO vehicle for 90 minutes. (B) Quantification of pSmad3 relative to β-actin control. Graph shows mean +/- SD of three replicates. *p<0.05.

Since we previously observed a possible in vivo effect of adrenergic signaling on pSmad3, we decided to further probe the relationship between forskolin and canonical TGFβ signaling. To determine whether the effects of forskolin on pSmad3 are dependent on PKA, we used the PKA inhibitor H-89. We tested a range of doses of H-89 on OCY454 cells and two different pretreatment durations before applying forskolin. We found that regardless of pretreatment time, the highest 25 μM dose of H-89 was needed to lower the pCreb response to forskolin, but this dose still did not return pCreb to non-forskolin-treated levels. In these experiments, 30 minutes of forskolin slightly raised pSmad3 levels, but pretreatment with H-89 at 25 μM blocked this response (Figure 7.11). Followup experiments suggested that pretreatment is not strictly necessary, and 25 μM H-89 is effective at reducing pCreb if added to cells at the same time as forskolin. These results show that adrenergic regulation of pSmad3 is indeed dependent on PKA.

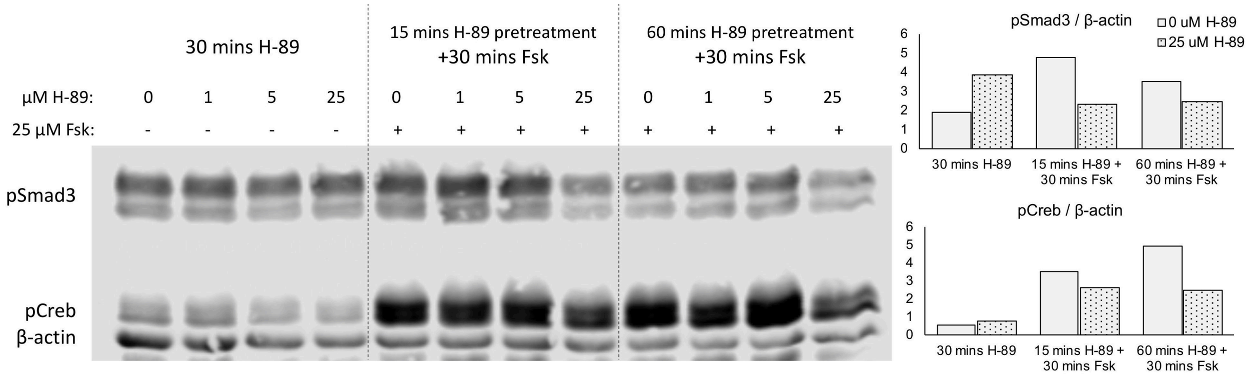

Figure 7.11: Induction of pCreb and pSmad3 by forskolin depends on PKA. OCY454 cells were treated with 25 μM forskolin or DMSO vehicle with or without H-89. Graphs show quantification of one replicate per condition/timepoint.

Forskolin reduces the response of osteocytes to TGFβ ligand

Another group has reported additive effects of TGFβ and norepinephrine in cardiac fibroblasts (20), so we hypothesized that regulation of pSmad3 by forskolin would be stronger in the presence of TGFβ ligand. A maximal pSmad3 response to TGFβ generally occurs around 60 minutes of treatment, so we treated OCY454 cells with TGFβ and forskolin together for 30-90 minutes. As expected, TGFβ significantly induced Smad3 phosphorylation at all timepoints (Figure 7.12). No forskolin-dependent effects on pSmad3 were observed between 30-60 minutes of treatment, consistent with Figure 7.9. At 90 minutes, however, forskolin suppressed pSmad3 relative to vehicle-treated cells in the control and TGFβ-treated groups (Figure 7.12).

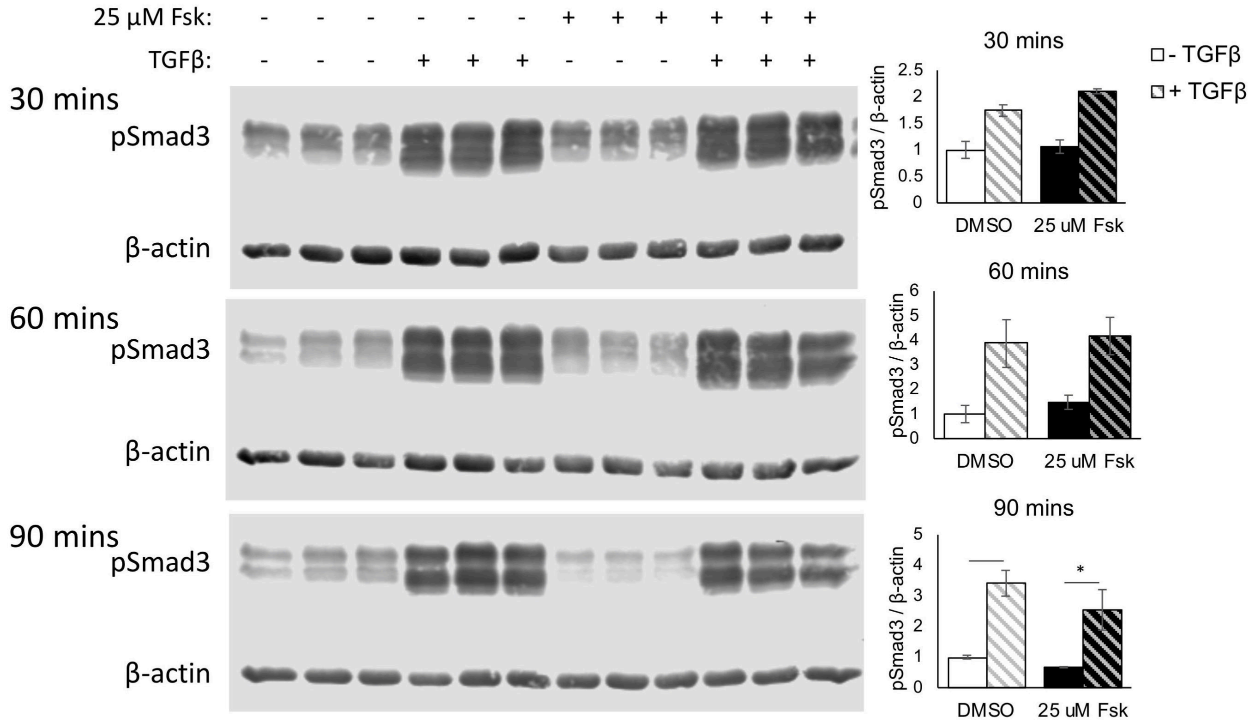

Figure 7.12: Forskolin represses TGFβ-induced pSmad3. OCY454 cells were treated with 25 µM forskolin or DMSO vehicle concurrently with 0 or 5 ng/mL TGFβ for the indicated times. Graphs show mean +/- SD of pSmad3 relative to β-actin control for three replicates of each condition. *$p<0.05$ effect of forskolin by two-way ANOVA.

To determine if adrenergic and TGFβ signaling pathways interact in their effects on downstream gene expression, we examined the expression of c-fos, Serpine1, Ptgs2 and Sost. C-fos serves as a positive control for forskolin treatment, and Serpine1 serves as a positive control for TGFβ treatment, while Ptgs2 and Sost are involved in the response to mechanical stimuli. All genes were subject to significant regulation by forskolin, with c-fos and Ptgs2 upregulated and Sost and Serpine1 downregulated (Figure 7.13). Mmp13 was also significantly induced by forskolin after three hours of treatment (data not shown). While Serpine1 is responsive to TGFβ in the presence of DMSO, the overall effect of TGFβ is diminished in the presence of forskolin. This result is consistent with the repression of pSmad3 after long-duration forskolin treatment but inconsistent with the upregulation of pSmad3 observed in loaded, atipamezole-treated bones. Nevertheless, these results illustrate both post-translational and transcriptional modulation of TGFβ signaling by forskolin treatment.

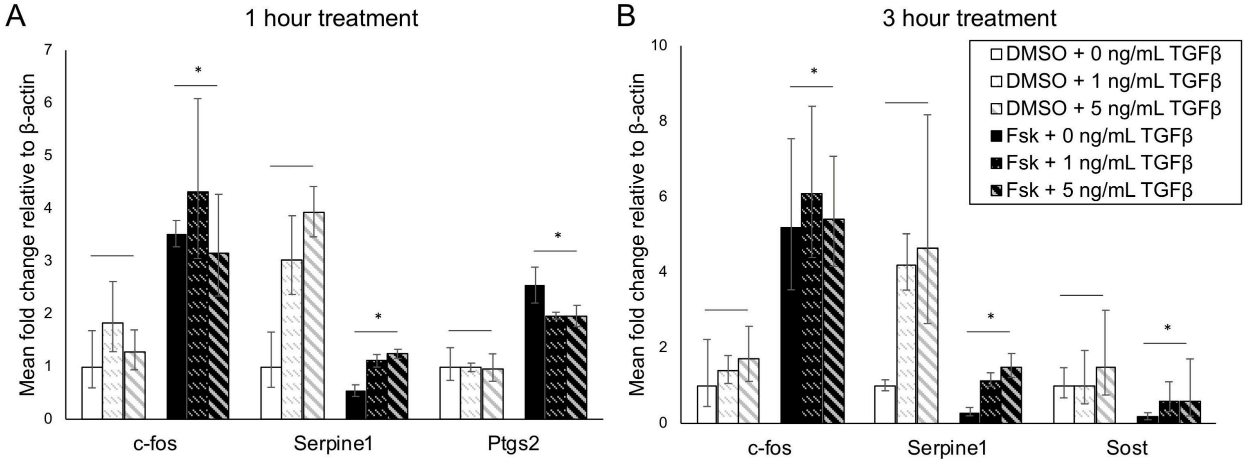

Figure 7.13: Forskolin diminishes the transcriptional response of Serpine1 to TGFβ. RNA was collected from OCY454 after (A) one hour or (B) three hours of treatment with 25 μM Fsk or DMSO vehicle concurrently with 0, 1, or 5 ng/mL TGFβ. Graphs show mean +/- SD of three replicates of each condition. *$p<0.05$ effect of forskolin by two-way ANOVA.

Discussion

These results establish that TGFβ signaling is subject to regulation by adrenergic signaling in osteocyte cell lines. Activating β2 receptors and inhibitory α2 receptors are expressed and functional in osteocytes. When signaling through adenylyl cyclase, cAMP, PKA and pCreb is activated, the canonical TGFβ effector pSmad3 is dynamically regulated, and multiple non-canonical effectors are rapidly induced or repressed. Therefore, the systemic changes in neurotransmitter availability expected to occur after atipamezole treatment can have an osteocyte-intrinsic effect on TGFβ signaling that may disrupt its normal mechanosensitive response.

Osteocytes in vitro are particularly sensitive to the activating stimuli of isoproterenol and norepinephrine (NE) through β-adrenergic receptors (ARs). This is consistent with prior work demonstrating the expression of β-ARs in the osteoblast lineage (13) and the sensitivity of bone mass to β-adrenergic stimulation and inhibition (11, 14). While current reports are extremely dose-, time-, receptor subtype-, and target tissue-specific, stimulation of β2-ARs both reduces bone formation and induces resorption in rodents (14, 25–27). The regulation of canonical TGFβ signaling in bone by adrenergic signaling pathways may be one driver of these changes in bone mass (28).

Sympathetic control of mechanosensitive bone remodeling has also received extensive research attention. While antagonizing β2-ARs with propranolol did not affect the magnitude of load-induced bone formation in young mice (29), it was found to suppress unloading-induced bone loss (30). Adenylyl cyclase has an established role in osteocytes as a mediator of mechanosensitive gene expression (23), and we found here that forskolin upregulated mechanosensitive Ptgs2. The forskolin-induced upregulation of Ptgs2 and downregulation of Sost would be expected after load, however their global regulation by sympathetic hyperactivity may mask further mechanosensitive responses in a single loaded limb. Bone loading during treadmill exercise was recently found to suppress sympathetic tone through action of bone-derived PGE2 on sensory nerves (31). This finding suggests that mechanosensation in bones involves the hypothalamus to change systemic SNS activity and favor bone anabolism. High plasma NE availability and activation of osteocytic β-ARs after atipamezole administration would compete with this existing signaling mechanism, which may partially explain the absence of normal mechanosensitive anabolism in our earlier mouse experiments (Figure 6.2). Future work should determine the magnitude and dynamics of NE release after atipamezole administration in mice.

While sympathetic tone is regulated on a somewhat systemic level, control of bone remodeling also depends on local signaling, at least in part through the TGFβ pathway. Past work found that loading at low, physiological magnitudes repressed canonical effector pSmad3, and that mice with inhibition of TGFβ signaling are insensitive to load (19). Therefore the long-term suppression of pSmad3 by forskolin in vitro, and the diminished transcriptional response of osteocytes to TGFβ ligand after forskolin treatment in vitro (Figure 7.13), may suggest that atipamezole treatment in mice leads to systemic TGFβ inhibition. Similarly, the short-term induction of pSmad3 by adrenergic signaling was consistent with the post-load upregulation of pSmad3 observed after atipamezole treatment in vivo, and may mask further mechanosensitive changes in Smad3 phosphorylation. Since β-agonists reduce bone mass, maybe in addition to a RANKL-dependent mechanism, the short-term induction of pSmad3 initiates an anti-anabolic signaling cascade. Together this work illustrates that TGFβ signaling through multiple effectors is a new possibility for the local effects of sympathetic nerve activity on mechanosensitive bone remodeling.

References

1. Elefteriou F (2018) Impact of the autonomic nervous system on the skeleton. *Physiol Rev* 98(3):1083–1112.
2. Mach DB, et al. (2002) Origins of skeletal pain: Sensory and sympathetic innervation of the mouse femur. *Neuroscience* 113(1):155–166.
3. Chartier SR, Mitchell SAT, Majuta LA, Mantyh PW (2018) The Changing Sensory and Sympathetic Innervation of the Young, Adult and Aging Mouse Femur. *Neuroscience* 387:178–190.
4. Serre CM, Farlay D, Delmas PD, Chenu C (1999) Evidence for a dense and intimate innervation of the bone tissue, including glutamate-containing fibers. *Bone* 25(6):623–629.
5. BIERING-SØRENSEN F, BOHR HH, SCHAADT OP (2008) Longitudinal study of bone mineral content in the lumbar spine, the forearm and the lower extremities after spinal cord injury. *Eur J Clin Invest* 20(3):330–335.
6. Heffner MA, Anderson MJ, Yeh GC, Genetos DC, Christiansen BA (2014) Altered bone development in a mouse model of peripheral sensory nerve inactivation. *J Musculoskelet Neuronal Interact* 14(1):1–9.
7. Tomlinson RE, et al. (2016) NGF-TrkA Signaling by Sensory Nerves Coordinates the Vascularization and Ossification of Developing Endochondral Bone. *Cell Rep* 16(10):2723–2735.
8. Tomlinson RE, et al. (2017) NGF-TrkA signaling in sensory nerves is required for skeletal adaptation to mechanical loads in mice. *Proc Natl Acad Sci*:201701054.
9. Elefteriou F, Campbell P, Ma Y (2014) Control of bone remodeling by the peripheral

sympathetic nervous system. *Calcif Tissue Int* 94(1):140–151.

10. Yang S, Nguyen ND, Eisman JA, Nguyen T V. (2012) Association between beta-blockers and fracture risk: A Bayesian meta-analysis. *Bone* 51(5):969–974.

11. Turker S, Karatosun V, Gunal I (2006) β-blockers increase bone mineral density. *Clinical Orthopaedics and Related Research* 443: 73–74.

12. Limonard EJ, et al. (2016) Clonidine increases bone resorption in humans. *Osteoporos Int* 27(3):1063–1071.

13. Fonseca TL, et al. (2011) Double disruption of α2A- and α2C -adrenoceptors results in sympathetic hyperactivity and high-bone-mass phenotype. *J Bone Miner Res* 26(3):591–603.

14. Elefteriou F, et al. (2005) Leptin regulation of bone resorption by the sympathetic nervous system and CART. *Nature* 434(7032):514–520.

15. Liang H, et al. (2019) Selective β2-adrenoreceptor signaling regulates osteoclastogenesis via modulating RANKL production and neuropeptides expression in osteocytic MLO-Y4 cells. *J Cell Biochem* 120(5):7238–7247.

16. Yao Q, et al. (2017) Beta-adrenergic signaling affect osteoclastogenesis via osteocytic MLO-Y4 cells' RANKL production. *Biochem Biophys Res Commun* 488(4):634–640.

17. Zhu Y, Ma Y, Elefteriou F (2018) Cortical bone is an extraneuronal site of norepinephrine uptake in adult mice. *Bone Reports* 9:188–198.

18. Scheinin H, et al. (1998) Reversal of the sedative and sympatholytic effects of dexmedetomidine with a specific alpha2-adrenoceptor antagonist atipamezole: a pharmacodynamic and kinetic study in healthy volunteers. *Anesthesiology* 89(3):574–584.

19. Nguyen J, Tang SY, Nguyen D, Alliston T (2013) Load Regulates Bone Formation and Sclerostin Expression through a TGF b -Dependent Mechanism. *PLoS One* 8(1):e53813.

20. Akiyama-Uchida Y, et al. (2002) Norepinephrine Enhances Fibrosis Mediated by TGF-in Cardiac Fibroblasts. doi:10.1161/01.HYP.0000025443.61926.12.

21. Zhang J, et al. (2016) Norepinephrine induced epithelial-mesenchymal transition in HT-29 and A549 cells in vitro. *J Cancer Res Clin Oncol* 142(2):423–435.

22. Yang H, et al. (2013) Protein kinase A modulates transforming growth factor-β signaling through a direct interaction with Smad4 protein. *J Biol Chem* 288(12):8737–49.

23. Kwon RY, Temiyasathit S, Tummala P, Quah CC, Jacobs CR (2010) Primary cilium-dependent mechanosensing is mediated by adenylyl cyclase 6 and cyclic AMP in bone cells. *FASEB J* 24(8):2859–2868.

24. Cherian PP, et al. (2003) Effects of Mechanical Strain on the Function of Gap Junctions in Osteocytes are Mediated through the Prostaglandin EP2 Receptor. *J Biol Chem* 278(44):43146–43156.

25. Bonnet N, et al. (2007) Doping dose of salbutamol and exercise: Deleterious effect on cancellous and cortical bones in adult rats. *J Appl Physiol* 102(4):1502–1509.

26. Bonnet N, et al. (2006) Dose effects of propranolol on cancellous and cortical bone in ovariectomized adult rats. *J Pharmacol Exp Ther* 318(3):1118–1127.

27. Swift JM, Swift SN, Allen MR, Bloomfield SA (2014) Beta-1 adrenergic agonist treatment mitigates negative changes in cancellous bone microarchitecture and inhibits osteocyte apoptosis during disuse. *PLoS One* 9(9).

doi:10.1371/journal.pone.0106904.

28. Mohammad KS, et al. (2009) Pharmacologic inhibition of the TGF-beta type I receptor kinase has anabolic and anti-catabolic effects on bone. *PLoS One* 4(4):e5275.

29. de Souza RL, Pitsillides AA, Lanyon LE, Skerry TM, Chenu C (2005) Sympathetic Nervous System Does Not Mediate the Load-Induced Cortical New Bone Formation. *J Bone Miner Res* 20(12):2159–2168.

30. Kondo H, et al. (2005) Unloading induces osteoblastic cell suppression and osteoclastic cell activation to lead to bone loss via sympathetic nervous system. *J Biol Chem* 280(34):30192–30200.

31. Chen H, et al. (2019) Prostaglandin E2 mediates sensory nerve regulation of bone homeostasis. *Nat Commun* 10(1):181.

Chapter 8

Mechanosensitive regulation of PLR

Introduction

Skeletal tissue has the remarkable ability to adapt to the mechanical demands it experiences. In cases of microgravity or disuse, bone mass is resorbed (1). After high loads, bone cells change their transcriptional profile and increase bone deposition in order to meet similar mechanical demands in the future (2, 3). Bone strength is determined not only by bone mass, but also by bone quality. Therefore, a major question in the field is whether bone quality is also mechanosensitively regulated.

In addition to evaluating the mechanosensitivity of bone mass, many studies have utilized the same rodent models of loading or exercise in order to characterize load-induced changes in bone material quality at multiple length scales. Three weeks of treadmill running affected strain to failure, yield stress, ultimate stress in the tibia (4, 5), with further significant increases in ultimate stress and modulus after two weeks of recovery time (6). At a smaller scale, treadmill running also affects carbonate-to-phosphate ratio (7) and collagen crosslinking (8). Two weeks of tibial loading at 2000 με affects mineral crystal size and mineralization ratio measured with Raman spectroscopy in addition to tibia ultimate stress and toughness (9, 10). Therefore in addition to changes in bone mass, and sometimes even in its absence, metrics of bone quality are mechanosensitive. The response of bone mass and quality to load varies with the magnitude of the loading stimulus and with location within the bone (10–13), suggesting the existence of specific, calibrated cellular mechanisms that regulate bone quantity and quality. Studies of bone quality have been largely descriptive, so the cellular and molecular mechanisms linking applied loads to changes in quality parameters are unknown.

Osteocytes are major regulators of both bone mass and bone quality. In response to glucocorticoids, hormones, TGFβ signaling, and expression of individual proteases, they increase or decrease their perilacunar/canalicular remodeling activity with implications for the organization and strength of the surrounding bone matrix. In addition to their role in maintaining their local environment, osteocytes also communicate extensively with osteoblasts and osteoclasts in response to physical and biochemical stimuli. Osteocytes are the major mechanosensory cells in bone, and they relay these signals to osteoblasts and osteoclasts to control bone mass. Receptor activator of nuclear factor-κB ligand (RANKL), for example, is released by osteocytes during bone disuse, which recruits osteoclasts and increases resorption at the bone surface (14). Expression of sclerostin by osteocytes is repressed following load, which relieves inhibition on the Wnt/β-catenin signaling pathway that ultimately increases osteoblast deposition (15). Despite their known ability of osteocytes to respond to load with paracrine signaling, it is not known whether osteocyte perilacunar/canalicular remodeling itself is a mechanosensitive process.

Several studies provide cellular evidence for and against the mechanosensitivity of PLR. Exercise and hind-limb loading induce a dynamic transcriptional response in bone including changes in PLR-related genes Acp5, Mmp14, Fgf23, and Timp1 (2, 7, 16, 17). Botox paralysis of a hindlimb for four weeks caused a decrease in lacunar density, and 15 days of spaceflight increased both lacunar area and canalicular diameter measured by NanoCT (18, 19). Neither 3-4 weeks of hindlimb suspension, nor three weeks of treadmill running were sufficient to induce a change in lacunar area (7, 20). However, osteocyte dendrites are much more mechanosensitive than cell bodies (21, 22), and we have often observed changes to canalicular morphology without corresponding changes to lacunae (23, 24). To our knowledge, the mechanosensitive regulation of canalicular remodeling in response to increased load has not been investigated.

Canalicular length and bone material quality are highly dependent on homeostatic TGFβ signaling. Systemic inhibition or induction at the ligand, receptor or effector level alters bone mass, toughness and elastic modulus (25–27). Osteocyte-specific inhibition of TGFβ signaling reduces expression of PLR enzymes, PLR-mediated organization of the lacunocanalicular network, flexural properties, and toughness (23). If the expression of PLR enzymes and markers of bone quality are controlled by TGFβ signaling in osteocytes, then mechanosensitive perturbations in TGFβ signaling could also affect PLR and bone quality.

TGFβ signaling is mechanoregulated at the ligand, receptor and effector levels, processes which are especially relevant in a tissue exposed to as many mechanical cues as bone (28). Our lab showed in 2012 that mechanosensitive anabolism depends on intact TGFβ signaling (29). Additionally, preliminary data has shown that *in vivo* load leads to a rapid repression of MMP13, known to be under the control of TGFβ and essential for control of bone quality (30). While TGFβ signaling and osteocytes themselves are each known to be mechanosensitive, their interactions to regulate bone quality have not been elucidated. By examining enzymes involved in PLR, and the organization and strength of bone at the tissue-level, this project tests the *hypothesis that osteocyte PLR controls bone quality in a mechanosensitive and TGF*β*-dependent manner.*

Methods

In vivo axial tibial loading

The mice used for these experiments were 8-week old male SBE-luciferase mice, which express luciferase when Smad2/3-dependent TGFβ signaling is active (Table 2.1). After troubleshooting and optimization (Chapter 6), the final protocol for murine axial tibial loading is described in Chapter 2. Briefly, mice are anesthetized with injectable ketamine/xylazine anesthesia (100 mg/kg ketamine and 10 mg/kg xylazine) and the right knee and heel are positioned between custom jigs on a BOSE Electroforce ELF3200 desktop load frame. 600 cycles of axial, compressive load between approximately -0.5 N and -6 N are applied at 1 Hz in displacement control. The load and displacement data are recorded at 10 Hz in order to calculate the actual applied loads and displacements for each loading session for each mouse.

At the end of loading, mice are returned to a warm cage to recover and then ambulate normally until the next loading session or predetermined harvest time. Loading was applied for either one 10-minute session, or for one 10-minute session per day on three consecutive days. After harvest, the non-loaded tibia serves as an internal control for each animal, as others have determined that the anabolic response to load is not systemic (3).

Protein harvest and Western blotting

3-4 hours after a single 10-minute load session, mice were euthanized and both tibias dissected. Marrow was centrifuged out, proximal and distal regions cut apart (Figure 8.1 A), and bone portions stored in liquid nitrogen. Protein was extracted from loaded and non-loaded bones using a bead mill homogenizer, quantified with the Bradford assay, and separated on 8.5% SDS-polyacrylamide gels. Primary antibodies are shown in Table 2.2.

Protein was detected on an Odyssey Infrared Imager (Licor) and images quantified in ImageStudio Lite software. Signal from test protein bands was normalized to signal from corresponding β-actin control bands for each sample. Normalized protein expression for loaded bone regions was then compared to corresponding non-loaded samples for each mouse.

Quantitative RT-PCR analysis

3 hours and 24 hours after a single 10-minute loading session and 4 hours after the last of three loading sessions, mice were euthanized and both tibias dissected. Marrow was centrifuged out, proximal and distal regions cut apart (Figure 8.1 A), and bone portions snap-frozen in liquid nitrogen. Bone portions were immediately homogenized in QIAzol and the lysate stored at -80 °C until RNA extraction and purification with the miRNeasy Kit. 1000 ng or 15 uL of RNA was reverse transcribed and cDNA concentration normalized to 10 ng/uL. qPCR was performed with TaqMan primers (Table 2.3) and normalized by the $\Delta\Delta$Ct method with β-actin as the housekeeping gene.

Dynamic histomorphometry

Mice used for histomorphometry were loaded for 10 minutes per day on three consecutive days. Calcein (20 mg/kg) was injected three days after the first load, and alizarin (30 mg/kg) was injected 8 days after the first load. Mice were euthanized 10 days after the first load, and both tibias were stored in 70% ethanol. Tibias were embedded in PMMA and sectioned axially at a site approximately 50% of the distance between the two tibiofibular junctions. Imaging was performed on a confocal microscope and quantification conducted in ImageJ. Mineralizing surface per bone surface (MS/BS), mineral apposition rate (MAR), and bone formation rate (BFR) were calculated for periosteal and endosteal surfaces (31). Due to a lack of double labeling observed on the periosteal surface, only endosteal values are reported. Samples without endosteal double labeling are not included in the MAR and BFR graphs.

Histology

24 hours after a single 10-minute loading session, and 10 days after the first of three consecutive days of loading, mice were euthanized and both tibias dissected. Tibias were fixed in 10% NBF, decalcified in EDTA, embedded in paraffin, and sectioned in the axial plane. Immunohistochemistry and silver nitrate staining were performed as detailed in Chapter 2.

For immunofluorescence, sections were deparaffinized and antigens were retrieved with 0.25% trypsin-EDTA at 37 °C for 25 minutes. Sections were blocked with Background Buster (Innovex) for 10 minutes, then incubated overnight with anti-sclerostin antibody at 4 °C, as described in Chapter 2. Sections chosen for analysis were selected at comparable axial positions approximately 50% of the distance between tibiofibular junctions.

For 3D canalicular analysis, decalcified bones were incubated in sucrose solution and then embedded in OCT. 50 μm sections were generated on a Cryostat, mounted on slides, and then infiltrated with phalloidin, DiI, and DAPI (32).

Results

To evaluate the possible mechanoregulation of PLR, I first sought to validate the loading model with established mechanosensitive outcomes. I loaded the right hindlimbs of 8-week old mice for 10 minutes and collected the loaded and non-loaded control bones 4 hours later to measure the mechanosensitive phosphorylation of Akt (33)(Figure 8.1 A, D). I found that loads above 5 N tended to induce pAkt in the loaded bone compared to the non-loaded bone, indicating effective mechanosensation (Figure 8.1 B, E). The relationship between load and pAkt was particularly strong in the distal region of the tibia, from the midpoint between tibiofibular junctions to the distal tibiofibular junction (Figure 8.1 A-C). The magnitude of pAkt induction in the loaded limb is even more strongly related to the load applied when it is normalized to the weight of the mouse, suggesting that individual bones are calibrated for their physiological experience (Figure 8.1 C). In the more proximal portion of bone, which contained cortical and cancellous bone, 4 N loads were often sufficient to induce Akt phosphorylation, and the magnitude of response was not increased further with higher loads (Figure 8.1 A, E, F).

Analyses of strain at the midpoint between tibiofibular junctions indicate that loads of 4-6 N, which induce pAkt, engender 650-1050 microstrain on the bone surface (Chapter

6). To determine whether these load and strain magnitudes were sufficient to induce bone formation, I loaded the right hindlimbs of mice on three consecutive days. Dynamic histomorphometric measurements at the midpoint between tibiofibular junctions indicated that loads of 4-6 N were indeed sufficient to induce bone formation (Figure 8.1 G-K). Endocortical mineralizing surface (MS/BS), mineral apposition rate (MAR), and bone formation rate (BFR) were significantly increased in the loaded limb compared to the non-loaded limb. We expect that a loading protocol that induces mechanosensitive changes related to bone mass would also be sufficient to induce changes in bone quality.

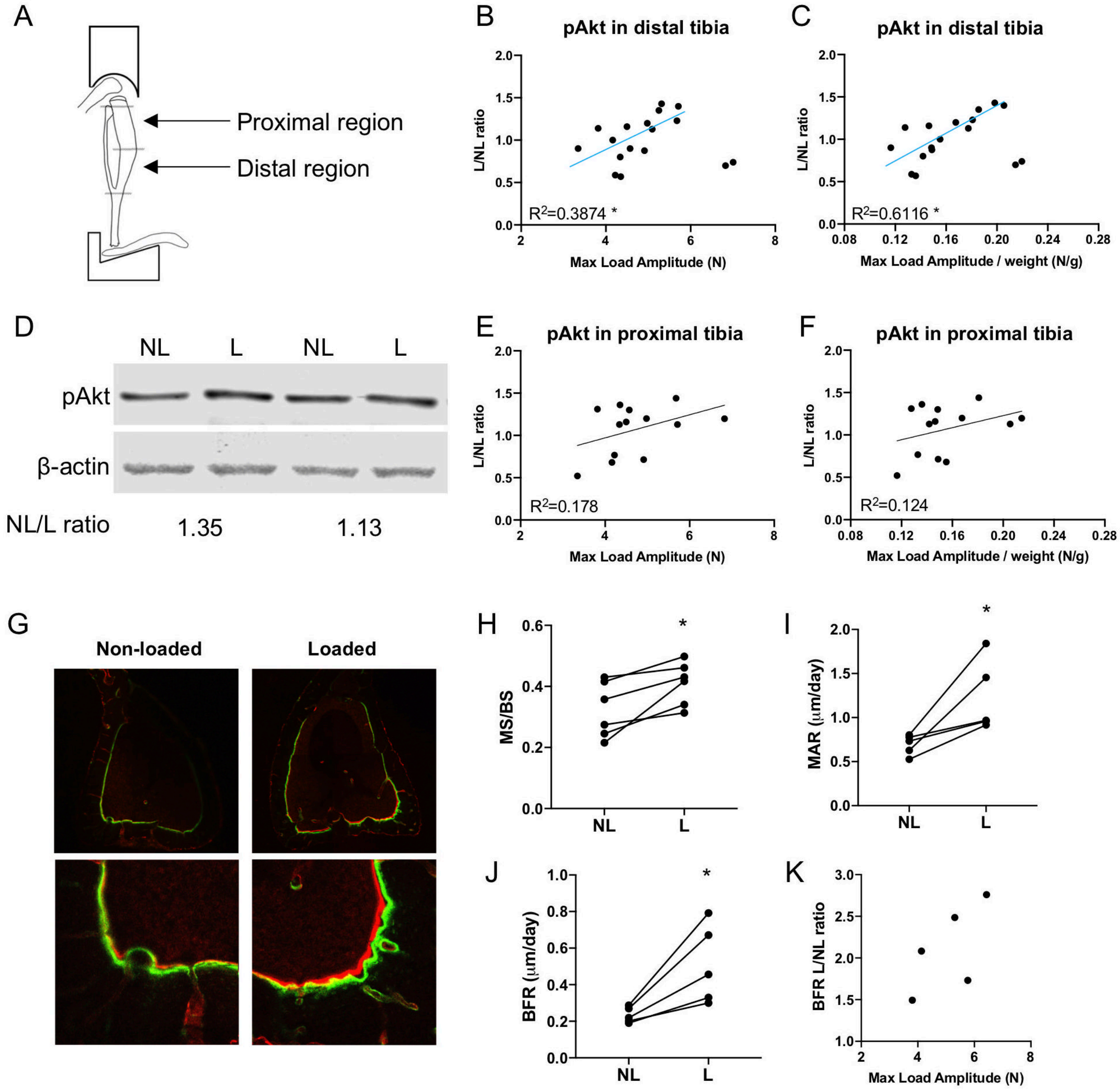

Figure 8.1: Validation of murine axial tibial loading protocol. (A) Diagram of murine tibial loading setup showing where proximal and distal regions of the tibia were separated for bulk analyses. (B-F) Western blot analysis of pAkt in loaded limbs compared to non-loaded control limbs of the same animals. The ratio of pAkt expression in loaded and non-loaded bone is plotted for the (B, C) distal and (E, F) proximal regions relative to (B, E) the load applied to the whole tibia or (C, F) the load normalized to mouse body weight. n=13-15. *p<0.05 excluding outliers. (G-K) Dynamic histomorphometric analysis at the midpoint between tibiofibular junctions. (H) Mineralizing surface per bone surface (MS/BS), (I) mineral apposition rate (MAR), and (J) bone formation rate (BFR) are plotted with non-loaded and loaded limbs from the same animal connected by a line. (K) The ratio of BFR in loaded and non-loaded tibias is plotted relative to load applied to the whole tibia. n=5-6, because no double labeling was observed in one animal. *p<0.05.

The transcriptional activity of bone cells in response to high loads (9-11 N, ≥1200 $\mu\varepsilon$) at high frequencies (2-4 Hz) has been described (2, 16, 17), but the effect of physiological load on genes encoding enzymes associated with PLR has not. To begin to address this question, I applied load to the right hindlimbs of mice for three consecutive days (34), separated the proximal and distal portions of the tibia, and measured expression of mechanosensitive gene Gja1, which encodes connexin 43 (35). I found that after three consecutive days of load, connexin 43 mRNA was significantly upregulated in the distal portion of the tibia (Figure 8.2 A). Interestingly, connexin 43 tended to be downregulated in the proximal tissue of the same loaded bones (Figure 8.2 B). Given that TGFβ signaling is mechanosensitive and is involved in PLR (23, 28, 29), I expected to observe mechanoregulation of the TGFβ-responsive gene Serpine1, but its regulation was not significant (Figure 8.2 C-D). However, across distal and proximal regions, the mechanoregulation of Gja1 and Serpine1 were strongly co-regulated in individual samples (Figure 8.2 E). Combined with the Western blot data showing the mechanosensitive phosphorylation of Akt, this illustrates the site-specificity of the molecular response to load in the tibia. Analysis of PLR genes including Mmps, Cathepsin K, and Acp5 by Nanostring is in progress.

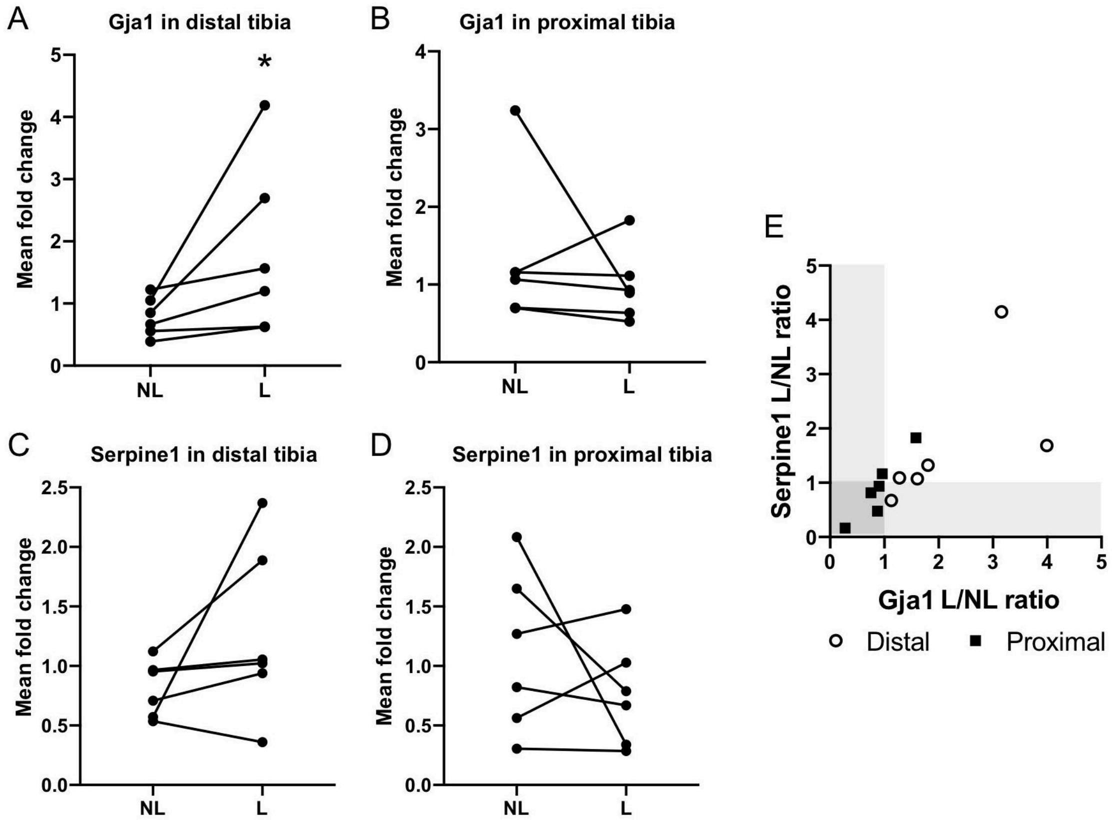

Figure 8.2: Gene expression in distal and proximal tibias loaded on three consecutive days. (A-B) Gja1 (Connexin 43) is upregulated in the distal tibia 4 hours after the last of three loading sessions, but it is not mechanoregulated in the proximal tibia, n=6 *p<0.02. (C-D) Serpine1 is not significantly mechanoregulated at this timepoint in either region. Gene expression in loaded and non-loaded bones from the same animal are connected by a line. (E) Serpine1 expression is related to Gja1 expression in the same samples. Grey shaded regions indicate repression.

To learn whether proteins involved in mechanosensation and PLR were regulated in our loading model, we used immunofluorescence and immunohistochemistry to analyze osteocyte expression of sclerostin and MMP13. Loaded and non-loaded bones were collected 24 hours after a single loading session, and sections at the midpoint between tibiofibular junctions were analyzed. At the highest loads tested – 6 N or above 0.2 N/g body weight – the mechanosensitive protein sclerostin was repressed compared to non-loaded controls (Figure 8.3 A-C). While regions predominantly experiencing tension and compression were analyzed separately in anticipation of site-specific differences (15), the mechanosensitive changes in sclerostin were uniform across the axial cross section. Expression of the PLR enzyme MMP13 was quantified in the posterior quadrant of the axial tibial cross section, where a similar response to load was observed. MMP13 appeared to be mechanosensitive, with higher loads causing more repression (Figure 8.3 D-F). This result may indicate that while high, anabolic loads repress PLR enzyme expression, lower loads allow normal PLR or even induce it. More bones loaded at higher magnitudes are being processed for analysis.

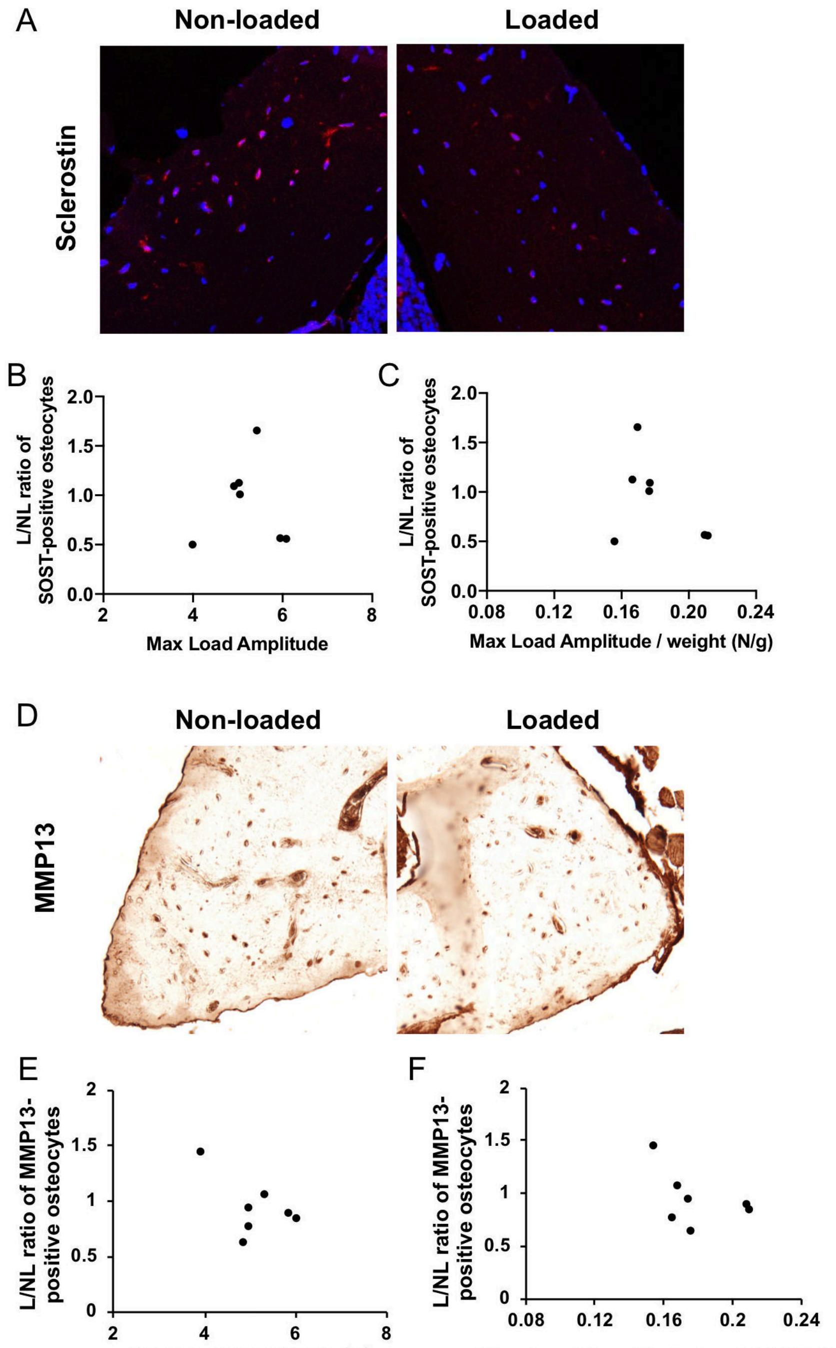

Figure 8.3: Mechanosensitive expression of sclerostin and MMP13 in osteocytes. (A) Representative immunofluorescence images of sclerostin 24 hours after load. (B-C) The ratio of sclerostin expression in loaded and non-loaded osteocytes is plotted relative to (B) applied load and (C) load normalized to mouse body weight. (D) Representative immunohistochemistry images of MMP13 24 hours after load. (E-F) The ratio of MMP13 expression in loaded and non-loaded osteocytes is plotted relative to (E) applied load and (F) load normalized to mouse body weight. n=7.

To determine the ability of osteocytes to remodel their lacunocanalicular network in response to mechanical load, we conducted 2D and 3D canalicular analyses. Bones were loaded for three consecutive days at low (4 N) and high (6 N) loads within our range of interest. Preliminary analysis reveals qualitative differences in canalicular morphology with load, such as increased canalicular length and density (Figure 8.4). Quantitative analyses are underway.

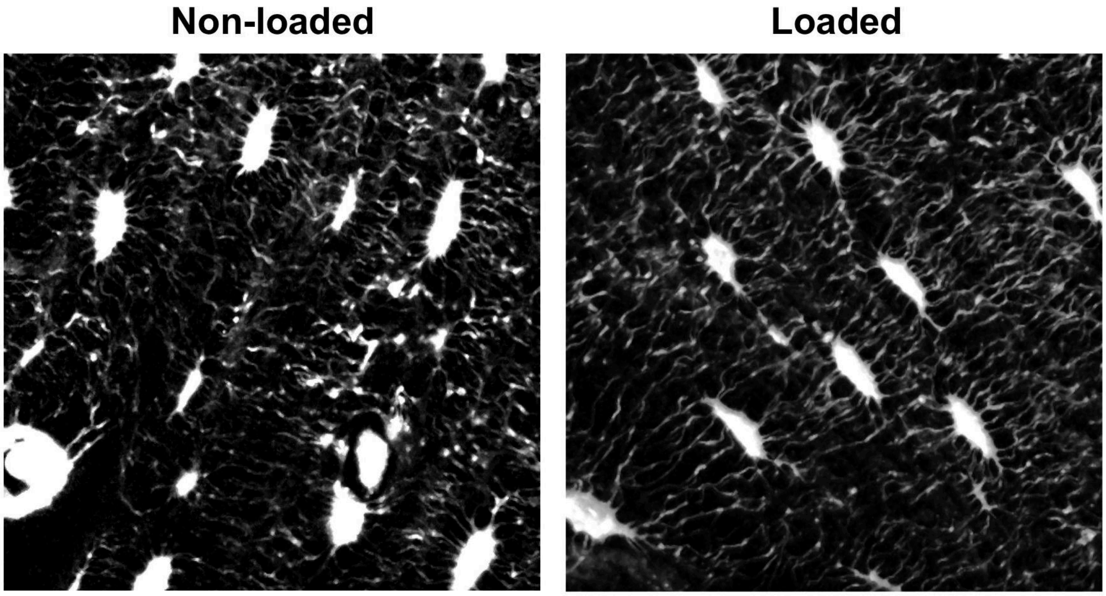

Figure 8.4: 3D whole-mount staining of the lacunocanalicular network in the distal tibia.

Discussion

To determine the extent to which PLR is mechanoregulated in vivo, we investigated cellular and tissue-level hallmarks of PLR in loaded and non-loaded mouse tibias. We found that bone anabolism was sensitive to load magnitude at lower loads and incident strains than are commonly reported (12, 13). Loads of 4-6 N were sufficient to induce a dynamic response in mRNA and protein expression of enzymes associated with PLR and may also affect the morphology of the lacunocanalicular network. Together this study provides evidence in support of the hypothesis that PLR is mechanosensitively regulated in a way that may couple load to control of bone quality.

In contrast to studies that focus on mechanosensitive changes to bone mass, we used physiological loads to determine their effect on osteocyte behavior. Reports on in vivo strain gaging of mouse tibias have found that normal walking and jumping engenders approximately 200-600 microstrain of tension on the middle of the medial bone surface (12, 36). Our applied loads between 4-6 N engendered between 650-1050 microstrain, and were sufficient to induce modest but significant changes in Akt phosphorylation and MAR. There was minimal double labeling observed on the periosteal surface of bone, consistent with the low strains engendered relative to other work (37, 38). We also found load-depended changes in MMP13 expression and canalicular morphology consistent with mechanoregulation of PLR.

The observed responses to load were highly dependent on the magnitude of applied load and strain. MMP13 protein expression, for example, may be slightly upregulated at low loads, but downregulated at higher loads within our tested range. This switch from upregulation to downregulation does not appear to coincide with the loads at which anabolism is induced, which challenges the existing paradigm in which low loads fall within a “lazy zone” that does not induce a mechanosensitive response. The switch may involve sequential activation of cellular mechanosensors with different sensitivities, crosstalk with nerves or vasculature in bone, or other as-yet unidentified mechanisms.

Our previous findings that inhibition of TGFβ signaling reduces osteocyte PLR and bone quality and that pSmad3 is repressed with load would together suggest that load suppresses processes that are required for the maintenance of healthy bone quality, however, exercise is overall beneficial for reducing risk of fracture (39, 40). Therefore it was ultimately not surprising to find that the response of PLR hallmarks to load is intricately regulated in a manner that could allow for cyclic induction and repression of osteocyte activity in response to different types of mechanical stimuli. For example, relatively low loads may induce PLR activity, whereas higher loads could repress local osteocyte remodeling through PLR while upregulating paracrine signaling to induce anabolism. As detailed in Chapter 6, there are many variables in the application of load, and other magnitudes, frequencies, durations or recovery periods may induce different effects. The differences between load applied directly to the hindlimb and loading induced through exercise are also likely important.

Together this study and related ongoing work provides evidence for the mechanosensitivity of osteocyte PLR. The dependence of this phenotype on TGFβ signaling will be reserved for separate investigation using a different strain of mice. Further studies will be needed in order to link mechanosensitive changes in bone quality to PLR and to inform clinical decision-making on best practices for modifying bone quality in vivo.

References

1. LeBlanc A (1995) *Space flight bone studies*.
2. Kelly NH, Schimenti JC, Ross FP, van der Meulen MCH (2016) Transcriptional profiling of cortical versus cancellous bone from mechanically-loaded murine tibiae reveals differential gene expression. *Bone* 86:22–29.
3. Sugiyama T, Price JS, Lanyon LE (2010) Functional adaptation to mechanical loading in both cortical and cancellous bone is controlled locally and is confined to the loaded bones. *Bone* 46(2):314–321.
4. Kohn DH, Sahar ND, Wallace JM, Golcuk K, Morris MD (2009) Exercise alters mineral and matrix composition in the absence of adding new bone. *Cells Tissues Organs* 189(1–4):33–7.
5. Wallace JM, et al. (2007) Exercise-induced changes in the cortical bone of growing mice are bone- and gender-specific. *Bone* 40(4):1120–1127.
6. Wallace JM, Ron MS, Kohn DH (2009) Short-Term Exercise in Mice Increases Tibial Post-Yield Mechanical Properties While Two Weeks of Latency Following Exercise Increases Tissue-Level Strength. *Calcif Tissue Int* 84(4):297–304.
7. Gardinier JD, Al-Omaishi S, Morris MD, Kohn DH (2016) PTH signaling mediates perilacunar remodeling during exercise. *Matrix Biol*:162–175.
8. Wallace JM, Golcuk K, Morris MD, Kohn DH (2010) Inbred strain-specific effects of exercise in wild type and biglycan deficient mice. *Ann Biomed Eng* 38(4):1607–1617.
9. Berman AG, Clauser CA, Wunderlin C, Hammond MA, Wallace JM (2015) Structural and Mechanical Improvements to Bone Are Strain Dependent with Axial Compression of the Tibia in Female C57BL/6 Mice. *PLoS One* 10(6).

doi:10.1371/journal.pone.0130504.

10. Bergström I, et al. (2017) Compressive loading of the murine tibia reveals site-specific micro-scale differences in adaptation and maturation rates of bone. *Osteoporos Int* 28(3):1121–1131.
11. Weatherholt AM, Fuchs RK, Warden SJ (2013) Cortical and trabecular bone adaptation to incremental load magnitudes using the mouse tibial axial compression loading model. *Bone* 52(1):372–379.
12. De Souza RL, et al. (2005) Non-invasive axial loading of mouse tibiae increases cortical bone formation and modifies trabecular organization: a new model to study cortical and cancellous compartments in a single loaded element. *Bone* 37(6):810–8.
13. Hsieh YF, Robling a G, Ambrosius WT, Burr DB, Turner CH (2001) Mechanical loading of diaphyseal bone in vivo: the strain threshold for an osteogenic response varies with location. *J Bone Miner Res* 16(12):2291–2297.
14. Bonewald LF (2011) The amazing osteocyte. *J Bone Miner Res* 26(2):229–38.
15. Robling AG, et al. (2008) Mechanical stimulation of bone in vivo reduces osteocyte expression of Sost/sclerostin. *J Biol Chem* 283(9):5866–5875.
16. Zaman G, et al. (2010) Loading-related regulation of gene expression in bone in the contexts of estrogen deficiency, lack of estrogen receptor α and disuse. *Bone* 46(3):628–642.
17. Roosa SMM, Liu Y, Turner CH (2011) Gene Expression Patterns in Bone Following Mechanical Loading. *J bone Miner Res* 26(1):100–112.
18. Gatti V, et al. (2019) Botox-induced muscle paralysis alters intracortical porosity and osteocyte lacunar density in skeletally mature rats. *J Orthop Res* 37(5):1153–1163.

19. Blaber EA, et al. (2013) Microgravity Induces Pelvic Bone Loss through Osteoclastic Activity, Osteocytic Osteolysis, and Osteoblastic Cell Cycle Inhibition by CDKN1a/p21. *PLoS One* 8(4). doi:10.1371/journal.pone.0061372.

20. Qing H, et al. (2012) Demonstration of osteocytic perilacunar/canalicular remodeling in mice during lactation. *J Bone Miner Res* 27(5):1018–1029.

21. Thi MM, Suadicani SO, Schaffler MB, Weinbaum S, Spray DC (2013) Mechanosensory responses of osteocytes to physiological forces occur along processes and not cell body and require αVβ3 integrin. *Proc Natl Acad Sci U S A* 110(52):21012–21017.

22. Cabahug-Zuckerman P, et al. (2018) Potential role for a specialized β(3) integrin-based structure on osteocyte processes in bone mechanosensation. *J Orthop Res* 36(2):642–652.

23. Dole NS, et al. (2017) Osteocyte intrinsic TGFβ signaling regulates bone quality through perilacunar/canalicular remodeling. *Cell Rep* 21(9):2585–2596.

24. Mazur CM, et al. (2019) Osteocyte dysfunction promotes osteoarthritis through MMP13-dependent suppression of subchondral bone homeostasis. *Bone Res* 7(1):34.

25. Balooch G, et al. (2005) TGF-beta regulates the mechanical properties and composition of bone matrix. *Proc Natl Acad Sci U S A* 102(52):18813–18818.

26. Mohammad KS, et al. (2009) Pharmacologic inhibition of the TGF-beta type I receptor kinase has anabolic and anti-catabolic effects on bone. *PLoS One* 4(4):e5275.

27. Edwards JR, et al. (2010) Inhibition of TGF-beta signaling by 1D11 antibody treatment increases bone mass and quality in vivo. *J Bone Miner Res* 25(11):2419–2426.

28. Rys JP, Monteiro DA, Alliston T (2016) Mechanobiology of TGFbeta signaling in the skeleton. *Matrix Biol* 52–54:413–425.

29. Nguyen J, Tang SY, Nguyen D, Alliston T (2013) Load Regulates Bone Formation and Sclerostin Expression through a TGF b -Dependent Mechanism. *PLoS One* 8(1):e53813.

30. Tang SY, Herber R-P, Ho SP, Alliston T (2012) Matrix Metalloproteinase-13 is Required for Osteocytic Perilacunar Remodeling and Maintains Bone Fracture Resistance. *J Bone Miner Res* 27(9):1936–1950.

31. Dempster DW, et al. (2013) Standardized nomenclature, symbols, and units for bone histomorphometry: A 2012 update of the report of the ASBMR Histomorphometry Nomenclature Committee. *J Bone Miner Res* 28(1):2–17.

32. Tiede-Lewis LAM, et al. (2017) Degeneration of the osteocyte network in the C57BL/6 mouse model of aging. *Aging (Albany NY)* 9(10):2187–2205.

33. Norvell SM, Alvarez M, Bidwell JP, Pavalko FM (2004) Fluid shear stress induces beta-catenin signaling in osteoblasts. *Calcif Tissue Int* 75(5):396–404.

34. Holguin N, Brodt MD, Silva MJ (2016) Activation of Wnt Signaling by Mechanical Loading Is Impaired in the Bone of Old Mice. *J Bone Miner Res* 31(12):2215–2226.

35. Plotkin L (2014) Connexin 43 hemichannels and intracellular signaling in bone cells . *Front Physiol* 5:131.

36. Sugiyama T, et al. (2012) Bones' adaptive response to mechanical loading is essentially linear between the low strains associated with disuse and the high strains associated with the lamellar/woven bone transition. *J Bone Miner Res* 27(8):1784–1793.

37. Brodt MD, Silva MJ (2010) Aged mice have enhanced endocortical response and normal periosteal response compared with young-adult mice following 1 week of axial tibial compression. *J Bone Miner Res* 25(9):2006–2015.

38. Holguin N, Brodt MD, Sanchez ME, Silva MJ (2014) Aging diminishes lamellar and woven bone formation induced by tibial compression in adult C57BL/6. *Bone* 65:83–91.

39. Sievänen H, Kannus P (2007) Physical Activity Reduces the Risk of Fragility Fracture. *PLoS Med* 4(6):e222.

40. Senderovich H, Tang H, Belmont S (2017) The Role of Exercises in Osteoporotic Fracture Prevention and Current Care Gaps. Where Are We Now? Recent Updates. *Rambam Maimonides Med J* 8(3):e0032.

Chapter 9

Conclusions

The belief that osteocytes were dormant placeholders in bone has evolved to an understanding of their essential dynamic role in bone maintenance. Largely in the past decade, essential roles for osteocytes in bone material quality and fracture resistance, in bone disease, and in mechanosensation have been elucidated. My doctoral research has explored and contributed to each of these themes.

The major findings of my dissertation research relate to bone quality and bone-cartilage crosstalk. I identified osteocyte-driven crosstalk between bone and cartilage as a causal factor in joint disease, where suppression of perilacunar/canalicular remodeling (PLR) contributes to osteonecrosis and osteoarthritis. I helped to elucidate cell-intrinsic roles for MMP13 and TGFβ signaling in PLR, and I demonstrated that PLR regulates bone quality during homeostasis. I also identified a novel regulatory role for adrenergic signaling in mechanosensitive TGFβ signaling. Together, we now know that osteocyte-specific changes in signaling regulate PLR, which maintains bone quality at multiple sites and has implications for joint disease (Figure 9.1).

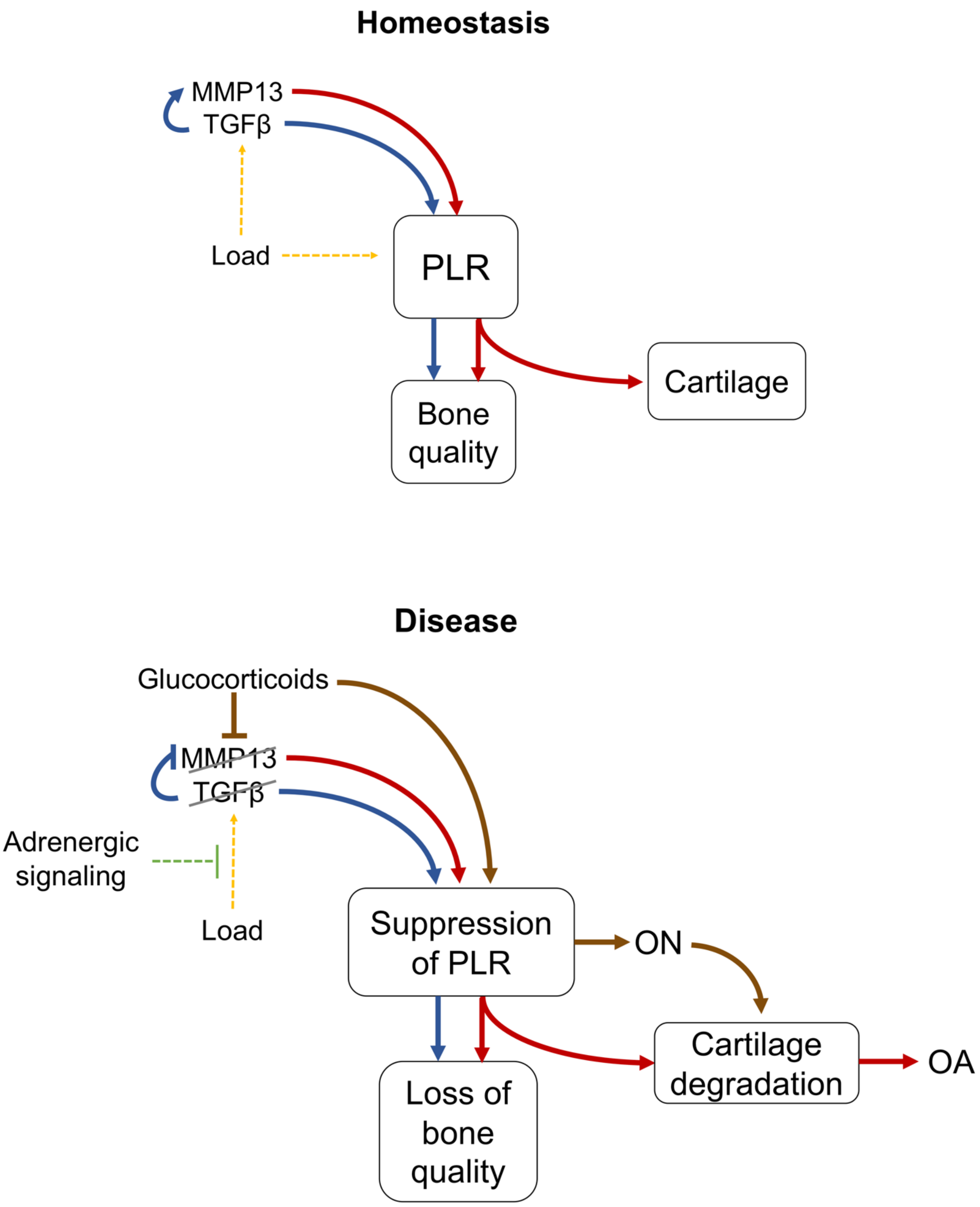

Figure 9.1: Schematic describing findings of dissertation research.

This work also pushes the field forward to new questions. For example, it is now becoming clear that osteocyte maintenance of canaliculi and lacunae are distinct processes, but the molecules and mechanisms underlying this differential regulation are unknown. Similarly, different genetic or drug interventions that disrupt PLR show different patterns of co-regulation or compensatory expression of PLR genes, and these patterns are not yet understood. The specific biological and mechanical mechanisms through which osteocyte-intrinsic defects in bone are able to affect cartilage also need to be investigated further. The site- and load-specific mechanoregulation of osteocyte activity in the mouse tibia also merits further study to determine how healthy osteocytes calibrate bone material properties for their functions and how these processes are disrupted in diseases of bone fragility.

Future work will hopefully identify additional hallmarks of PLR that can be studied in vitro or in high-throughput systems. The development of clinical markers of PLR will also be needed to further understand the contribution of osteocytes to disease development in humans and to evaluate the efficacy of novel drugs that target osteocytes.

Publishing Agreement

It is the policy of the University to encourage the distribution of all theses, dissertations, and manuscripts. Copies of all UCSF theses, dissertations, and manuscripts will be routed to the library via the Graduate Division. The library will make all theses, dissertations, and manuscripts accessible to the public and will preserve these to the best of their abilities, in perpetuity.

Please sign the following statement:

I hereby grant permission to the Graduate Division of the University of California, San Francisco to release copies of my thesis, dissertation, or manuscript to the Campus Library to provide access and preservation, in whole or in part, in perpetuity.

DocuSigned by:
Courtney Mazur
A8803A696FDA4D6...
Author Signature

12/17/2019
Date